CRYSTAL STRUCTURES AND FERROELECTRIC BEHAVIOUR OF EPITAXIAL BISMUTH FERRITE THIN FILMS

LIU HUAJUN

NATIONAL UNIVERSITY OF SINGAPORE

2012

CRYSTAL STRUCTURES AND FERROELECTRIC BEHAVIOUR OF EPITAXIAL BISMUTH FERRITE THIN FILMS

LIU HUAJUN

(*B.Sc. USTC, CHINA*)

A THESIS SUBMITTED

FOR THE DEGREE OF DOCTOR OF PHILOSOPHY

DEPARTMENT OF MATERIALS SCIENCE AND ENGINEERING

NATIONAL UNIVERSITY OF SINGAPORE

2012

DECLARATION

I hereby declare that the thesis is my original work and it has been written by me in its entirety. I have duly acknowledged all the sources of information which have been used in the thesis.

This thesis has also not been submitted for any degree in any university previously.

_____

LIU HUAJUN

15 August 2012

ACKNOWLEDGEMENTS

First of all, I would like to express the most sincere gratitude to my supervisor, Prof. John Wang, for his enormous support, guidance and encouragement during my PhD study at National University of Singapore. I benefited greatly from his inspiring suggestions and discussions on both research work and way of life. All these will be a great wealth for my whole research career.

I would like to convey my great appreciation to my co-supervisor, Dr. Yao Kui, for his patience and critical discussions on my work. From the weekly meeting in Institute of Materials Research and Engineering (IMRE), I learned a lot from his independent thinking of research ideas, enthusiasm and dedication to research projects.

I would like to give special thanks to Dr. Yang Ping, for his invaluable guidance and hands-on teaching of X-ray characterization of thin films at Singapore Synchrotron Light Source (SSLS). His profound knowledge in the theory and practice of X-ray techniques provides me great support during the whole PhD time.

The former and current group members in Advanced Ceramics Lab are acknowledged for their useful suggestions and discussions on experiments. They are Dr. Lou Xiaojie,

Dr. Wu Jiagang, Dr. Wang Yang, Dr. Zhang Yu, Dr. Happy Tan, Zheng Rongyan, Sim Chow Hong, Fransiska Cecilia Kartawidjaja, Ke Qingqing, Kang Guangqing, Li Hui, Liu Yanqiong, and Yang Zhenchun. Their friendship and cheerful moments makes the PhD time wonderful. I would like to thank Ji Wei, Tan Huiru, Lim Poh Chong for help with experiments in IMRE. I am also grateful to the help with X-ray experiments from Dr. Du Yonghua and Chew Eh Piew at SSLS.

Finally, I would like to thank my parents and wife for their continuous support and understanding during my PhD study. I owe everything I achieved to them. This thesis is dedicated to them.

TABLE OF CONTENTS

SUMMARY

The coupling between ferroelectric order and magnetic order, which gives rise to magnetoelectric multiferroic behaviour, attracts considerable research activities recently. The renaissance of multiferroic research arises mainly from the study on the only known single phase multiferroic material at room temperature - Bismuth Ferrite ($BiFeO_3$, or BFO). Even though intensive efforts have been dedicated to epitaxial BFO thin films, the relationship between the crystal structure and physical behaviour of BFO is still not clear, owing to the rich crystallographic phases and the complicated balance between different physical orders in BFO system.

This thesis focuses on the investigation into crystal structures and ferroelectric behaviour of different phases in BFO epitaxial thin films. Firstly, the crystal structure and strain effect on ferroelectric performance of BFO thin films deposited on $SrRuO_3$-buffered $SrTiO_3$ (STO) (001) substrates were investigated. For the 30-nm-thick BFO film, the crystal structure is a fully strained tetragonal phase with small $c/a \sim 1.05$. A unique twinning rotation structure with a monoclinic symmetry was identified for BFO films with thickness from 180 to 720 nm. Concerning the strain effect on ferroelectric polarization, our investigations demonstrate that remanent polarization doesn't show a clear correlation with strain. Instead, it is strongly

dependent on the body diagonal length of distorted pseudocubic unit cell, which is along the polarization direction.

Secondly, the super-tetragonal BFO phase was studied via two approaches. The first approach is to form BFO films on STO (001) substrates using high sputtering power above 150 W. Systematic structure analyses show that the parasitic β-Bi_2O_3 (BO) phase is the origin for the formation of super-tetragonal BFO phase when deposited at high sputtering power on STO substrates. By employing BO as a buffer layer, super-tetragonal phase BFO can be grown at low sputtering power on STO substrates. The second approach is to distort BFO lattice by substrates with large compressive strain above ~4.5%. For the ultrathin BFO film below 10 nm grown on $LaAlO_3$ (001) substrates, a monoclinic M_A structure with a giant *c/a* is developed. The large compressive strain of ~7% from $NdCaAlO_4$ substrate constrains BFO into a strictly super-tetragonal phase for the film thickness of ~30 nm.

The results obtained in this project help to improve the understanding of BFO crystal structures under different growth condition and strain state. The ferroelectric behaviour of monoclinic phase BFO supports the microscopic origin of ferroelectric polarization from the ionic displacement induced dipole moments. This project provides two general routes to stabilize the promising super-tetragonal phase in BFO epitaxial thin films, which facilitates the searching for improved performance in BFO-based systems.

LIST OF FIGURES

LIST OF TABLES

LIST OF PUBLICATIONS

1. ***H. Liu***, P. Yang, K. Yao, K. P. Ong, P. Wu and J. Wang, *Origin of a tetragonal $BiFeO_3$ phase with a giant c/a ratio on $SrTiO_3$ substrates*, ***Advanced Functional Materials***,22, 937-942, (2012).
2. ***H. Liu***, P. Yang, K. Yao and J. Wang, *Growth rate induced monoclinic to tetragonal phase transition in epitaxial $BiFeO_3$ (001) thin films*, ***Applied Physics Letters***, 98, 102902, (2011).
3. ***H. Liu***, K. Yao, P. Yang, Y. Du, Q. He, Y. Gu, X. Li, S. Wang, X. Zhou and J. Wang, *Thickness-dependent twinning evolution and ferroelectric behavior of epitaxial $BiFeO_3$ (001) thin films*, ***Physical Review B***, 82, 064108, (2010).
4. ***H. Liu***, P. Yang, K. Yao and J. Wang, *Twinning rotation and ferroelectric behavior of epitaxial $BiFeO_3$ (001) thin film*, ***Applied Physics Letters***, 96, 012901, (2010).
5. J. Wu, G. Kang, ***H. Liu*** and J. Wang, *Ferromagnetic, ferroelectric and fatigue behavior of (111)-oriented $BiFeO_3/(Bi_{1/2}Na_{1/2})TiO_3$ lead-free bilayered thin films*, ***Applied Physics Letters,*** 94, 172906, (2009).

Chapter 1. INTRODUCTION

1.1 Ferroelectricity and Ferroelectric Materials

Ferroelectricity, as a topic in classical condensed matter physics, is theoretically interesting due to the unique hysteresis behaviour under electric field [1]. It is the electrical counterpart of ferromagnetism. Ferroelectric materials are also practically attractive because of their wide applications, for example in high dielectric constant capacitors, piezoelectric transducers, nonvolatile random access memories, and sensor devices [2]. In addition, ferroelectric materials have been employed to replace inactive dielectric counterparts in traditional electronic devices to achieve smart devices [3]. A number of novel applications are also emerging, for example, combing ferroelectricity and magnetic properties into a single phase material promises the generation of multifunctional spintronic devices [4].

Definition of Ferroelectricity

For a material to be considered ferroelectric, it must possess two or more stable states of electric spontaneous polarization in zero applied electric field, which can be switched

reversibly by an external electric field [1]. The main characteristic behaviour of ferroelectrics is the hysteresis loop of polarization as a function of the applied electric field. From the hysteresis loops, critical parameters such as the spontaneous polarization P_s, remanent polarization P_r and coercive electric field E_C can be derived (Figure 1.1), which are important for the applications in electronic devices. Another important characteristic of ferroelectricity is its temperature dependence. For a given ferroelectric material, above the Curie temperature T_C, the ferroelectric polarization would be lost and the ferroelectric state would transfer to a non-polar paraelectric state. Hence, in order for ferroelectrics to work properly at room temperature, it is essential for the material to possess a T_C well above room temperature.

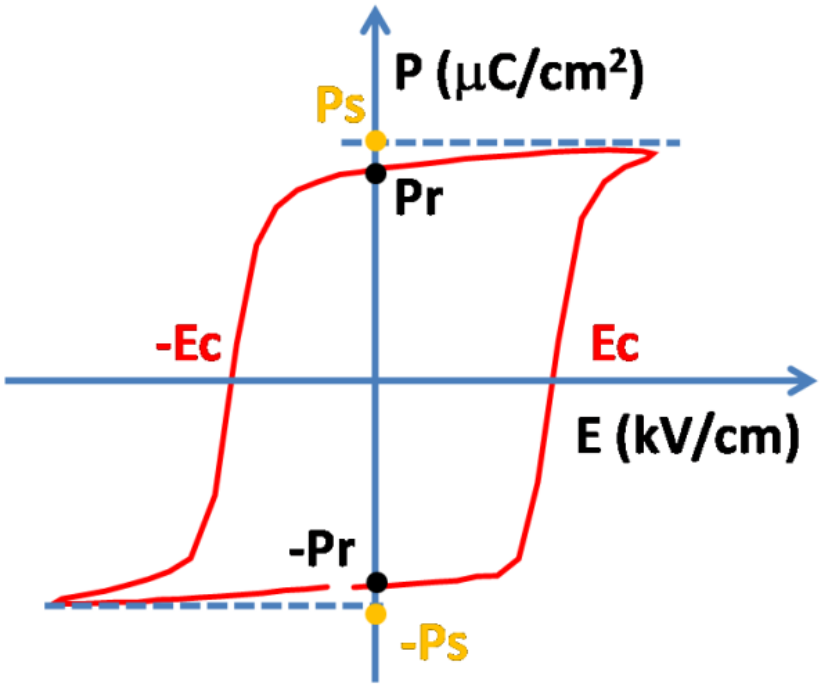

Figure 1.1 Ferroelectric hysteresis loop illustrating the spontaneous polarization P_s, remanent polarization P_r and coercive electric field E_C.

Ferroelectricity and crystal structure are intimately coupled. From crystallographic point of view, only those materials lacking the centro-symmetry can be polar and exhibit spontaneous electric polarization. Otherwise, the polar state would cancel each other. Within the thirty-two crystallographic point groups, only ten of them have a unique polar axis. Normally, the crystal structure changes from the centrosymmetric to non-centrosymmetric phase, corresponding to the transition from paraelectric phase to ferroelectric phase. Therefore, the ferroelectric phase transition is also known as symmetry breaking transition and the paraelectric phase as the high-symmetry reference structure. The ferroelectric crystal phase can be understood as a distortion along certain direction of the unit cell of these reference structures. For example, $BaTiO_3$ exhibits a cubic structure for the paraelectric phase above 120 ˚C and a tetragonal structure for the ferroelectric phase at room temperature [5]. In this case, the distortion along *c* axis breaks the centro-symmetry, resulting in the atomic shift following this direction. For this reason, a thorough investigation into the crystal structure is essential in understanding the origin of ferroelectricity, which provides directions for optimizing ferroelectric properties by properly tuning crystal structures.

Laudau-Devonshire Theory

Thermodynamically, the basic properties of ferroelectric materials result from the

double well potential in the diagram of free energy as a function of polarization (Figure 1.2). As the temperature increases, the ferroelectric phase would evolve into a high symmetry paraelectric phase with a single minimum for the free energy. There are two different mechanisms of temperature dependent phase transition. The first one is the order-disorder phase transition, in which the shape of the potential well is independent of temperature and the kinetic energy at high temperature creates a disorder state of ion positions above the transition temperature. The second one is the most common phenomena in ferroelectrics- the displacive phase transition. In this case, the shape of potential changes with temperature and has a single minimum above the phase transition temperature. The displacive phase transition is well described by Landau-Devonshire theory [6], which is briefly discussed in the following paragraph.

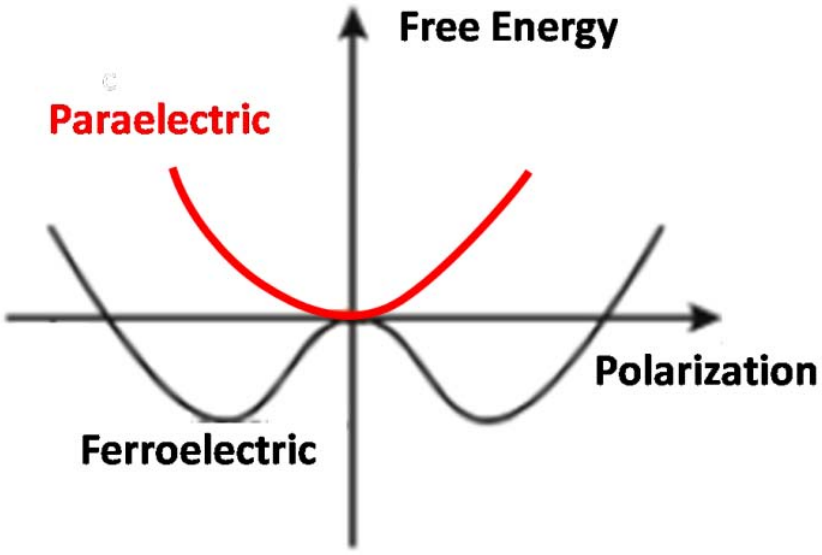

Figure 1.2 Free energy as a function of polarization for the ferroelectric phase and the paraelectric phase.

In the Landau-Devonshire theory, it is assumed that the free energy *F* of a thermodynamic stable system can be expanded in a power series of specific order parameters [7] . For a bulk ferroelectric system, these order parameters are the polarization *P*, electric field *E*, and temperature *T*. If one assumes the origin of the energy of the unpolarized and unstrained ferroelectric crystal to be zero, the free energy can be described as

$$F(P,E,T) = -EP + \frac{1}{2}aP^2 + \frac{1}{4}bP^4 + \frac{1}{6}cP^6 \quad . \tag{1.1}$$

The coefficient $a = a_0(T - T_0)$, which is a necessary result of the mean field theory supported by experimental observations. The free energy is minimized in the thermal equilibrium, thus one can have

$$\frac{\partial F}{\partial P} = 0 . \tag{1.2}$$

This shall give

$$E = aP + bP^3 + cP^5 . \tag{1.3}$$

The coefficient *b* here determines the order of paraelectric to ferroelectric phase transition. When *b* is positive, the phase transition is a continuous second order transition. At zero electric field, one can obtain

$$P_0 = \sqrt{\frac{a_0}{b}(T_0 - T)} . \tag{1.4}$$

The change of free energy and polarization are plotted in Figure 1.3 (a). In this case, there is no latent heat of transition. When *b* is negative, the phase transition will be a

first order discontinuous one. Polarization can be derived from

$$a_0(T - T_0)P + bP^3 + cP^5 = 0\,. \tag{1.5}$$

The first and second order phase transitions described by Landau theory are shown schematically in Figure 1.3.

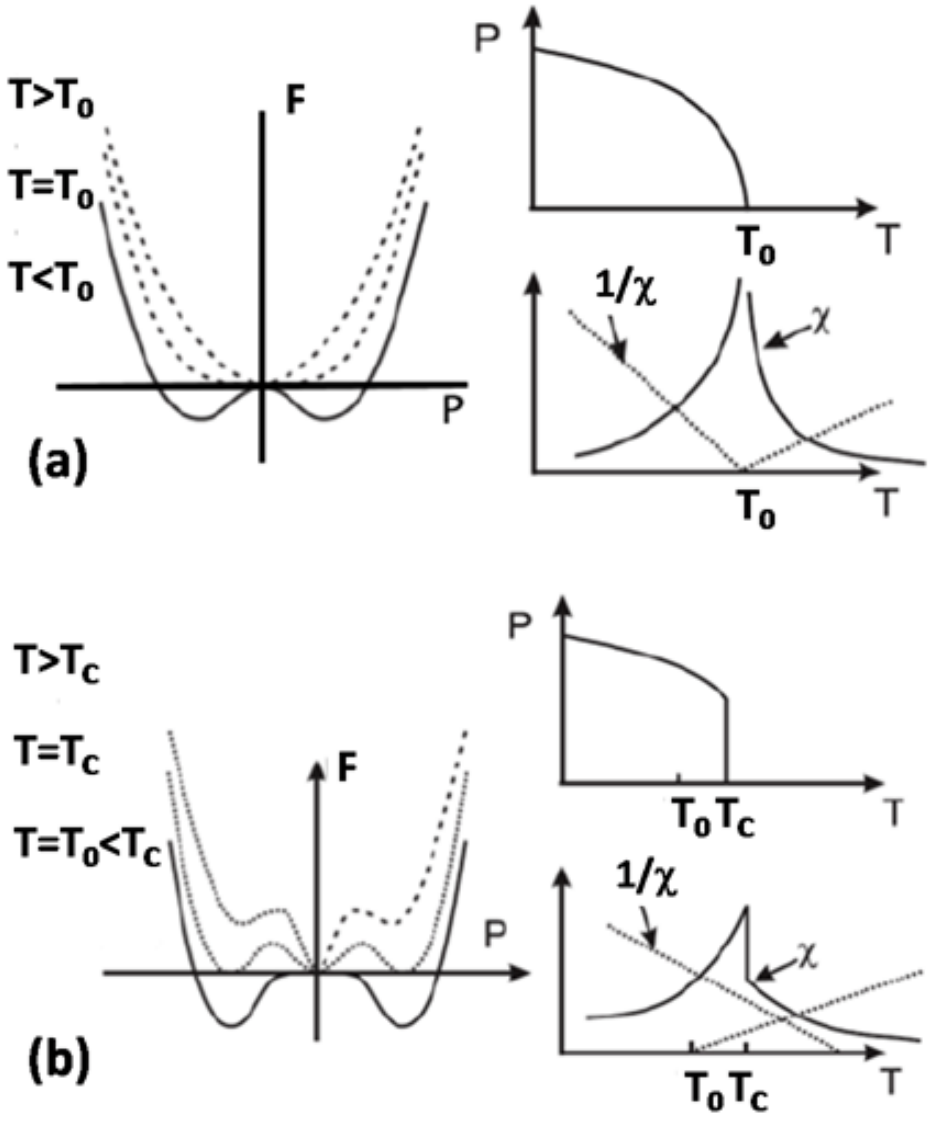

Figure 1.3 Plot of free energy as a function of polarization, spontaneous polarization as a function of temperature, susceptibility and its inverse as a function of temperature for (a) second order phase transition and (b) first order phase transition. Figure adopted from [7].

Ferroelectric Materials

There are several families of ferroelectric materials. In the 1920s, the first discovery of ferroelectricity was from the Rochelle salt, which has hydrogen bonds [8]. Due to the water soluble and fragile, the early family of hydrogen containing ferroelectric materials is not of much interest to researchers. Later, during World War II, the discovery of $BaTiO_3$ opened the door for the most technologically important family of ferroelectric materials- the perovskites. The simple structure and robust physical properties of perovskite ferroelectric materials stimulated both theoretical work and device development [2]. Until today, the most studied family of ferroelectric materials is still the pervoskite oxides. The dominant material for the application in sensors and actuators is lead titanate zirconate (PZT), which is a typical perovskite solid solution [9]. A recent direction for the searching of ferroelectric materials focuses on lead-free candidates, as lead containing materials are considered environmentally harmful. The alkaline niobate-based perovskite solid solution, as a lead free ferroelectric ceramic, provides comparative performance with the PZT family [10]. One more recent development of ferroelectric materials is to combine ferroelectric properties with ferromagnetic, ferroelastic properties to achieve the so-called “multiferroic” materials [11]. Among the multiferroic candidates, bismuth ferrite ($BiFeO_3$, or BFO) is most

interesting as it is the only single phase material that is both a strong ferroelectric and antiferromagnetic at room temperature [12]. This thesis focuses on the epitaxial thin films of this new generation of multifunctional material. In Section 1.2 below, a detailed review of multiferroic materials and BFO is given.

1.2 Multiferroics and Bismuth Ferrite

Multiferroics

Multiferroic materials, which show simultaneously ferroelectric, ferromagnetic and ferroelastic behaviour, attract considerable attentions recently [13]. Magnetoelectic (ME) materials are among an important class of multiferroics, showing ferroelectric and magnetic orders. On the one hand, the ME material promises wide applications in industry. Particularly, due to the interactions between magnetic and electric polarizations, it has promising applications in data storage allowing the electric field-controlled switching of magnetization and vice versa. On the other hand, these new multifunctional materials give rise to new physical phenomena, such as the phase transition under magnetic and electric fields and magnetoelectric interactions at the atomic scale. Indeed, there has been a revival of interest of in this field in recent years [13]. However, there are quite few single phase materials belonging to this category of

ME materials [14]. Theoretically, the mechanisms driving ferromagnetism and ferroelectricity at atomic scale are mutually exclusive. In conventional ferroelectric materials, such as $BaTiO_3$, the off-centering of cation requires empty *d* orbitals, while the formation of magnetic moment needs partially filled *d* orbital.

There are generally two approaches to design and look for materials with strong ME coupling. The first one is to combine piezoelectric and magnetostrictive materials together to realize the ME coupling mediated by strain [15]. The concept of two phase composite magnetoelectrics was first proposed by Van Suchtelen in 1972 [16]. Neither the piezoelectric nor magnetostrictive material shows ME effect, however, the composite consisting of the two phases shows good ME effect. The overall ME effect is caused by the product tensor property,

$$ME = \frac{electric}{mechnical} \times \frac{mechanical}{magnetic} \quad . \tag{1.6}$$

An electrical field applying to the composite will induce stain in the piezoelectric component, which is passed on to the magnetostritive material, where it causes magnetic moment. Similarly, applying a magnetic field will cause electrical polarization. Therefore, the ME effect is realized in these piezoelectric-magnetostrictive composite materials through the bridging of strain.

The second one is to search for the single phase magnetoelectric material. It is the

single phase magnetoelectric that creates new physical phenomena and contributes to the basic understandings. However, as mentioned above, the single phase magnetoelectric materials are very rare in nature due to the mutually exclusive mechanisms of ferroelectricity and ferromagnetism [14]. In the conventional model ferroelectric materials, such as $BaTiO_3$ or $PbTiO_3$, the hybridization between the titanium *3d* states and the oxygen *2p* states is essential for stabilizing the ferroelectric distorted state. So, the empty *3d* orbital is required for ferroelectricity, which is in contradiction with the requirement of partially filled *3d* orbital for ferromagnetism. To allow for the coexistence of ferroelectric and magnetic ordering in one phase, new ferroelectric mechanisms in which the polar state is stabilized by other driving forces have been developed over the past decades [17]. There are generally five different new origins of ferroelectricity found in crystals [18]. The ferroelectricity is driven by lone pair electrons of A-site cation [19], geometrically frustration from long range dipole-dipole interaction [20], charge ordering [21], magnetic long range order [22], and order-disorder hydrogen bonding transition in Metal-Organic Frameworks [23], respectively in each type of multiferroic materials. Bismuth ferrite belongs to the first type of single phase magnetoelectric materials, in which the two lone pair valence electrons in *6s* orbital of Bi drive to the off-center polar state of crystal and result in ferroelectricity. Meanwhile, the Fe ion gives rise to the antiferromagnetic ordering.

Bismuth Ferrite (BFO)

Among the different types of multiferroics discussed above, BFO is the only single phase that is both strong ferroelectric and magnetic at room temperature [12]. Indeed, due to the promising multi-functional applications, numerous studies have been published over the last decade, where investigations have been made into the magnetoelectric mechanisms and improvement in the coupling between magnetic and ferroelectric orders. The following descriptions are devoted to give a brief introduction on the crystal structure, ferroelectric, magnetic, piezoelectric properties, ME coupling and photovoltaic effect of BFO.

Bulk BFO belongs to *R3c* space group, with the lattice parameters of a = 5.6343 Å and α = 59.348° in rhombohedral unit cell [24]. Also, it can be expressed in hexagonal unit cell, a = 5.5787 Å and c = 13.8688 Å. This structure can be seen as a rhombohedrally distorted perovskite structure, with lattice parameters a = 3.965 Å, α = 89.45°, which is often used in literature as "pseudocubic unit cell" to conveniently index the crystal planes. A schematic diagram of BFO unit cell in different crystal system is shown in Figure 1.4. Due to the counter-rotation of oxygen octahedron along 3-fold axis along [001] direction in hexagonal system, the primitive unit cell contains two formula units with ten atoms. The iron atom is shifted away from the center of oxygen octahedron by 0.134 Å, which is much larger than other perovskite ferroelectrics without Bi [25].

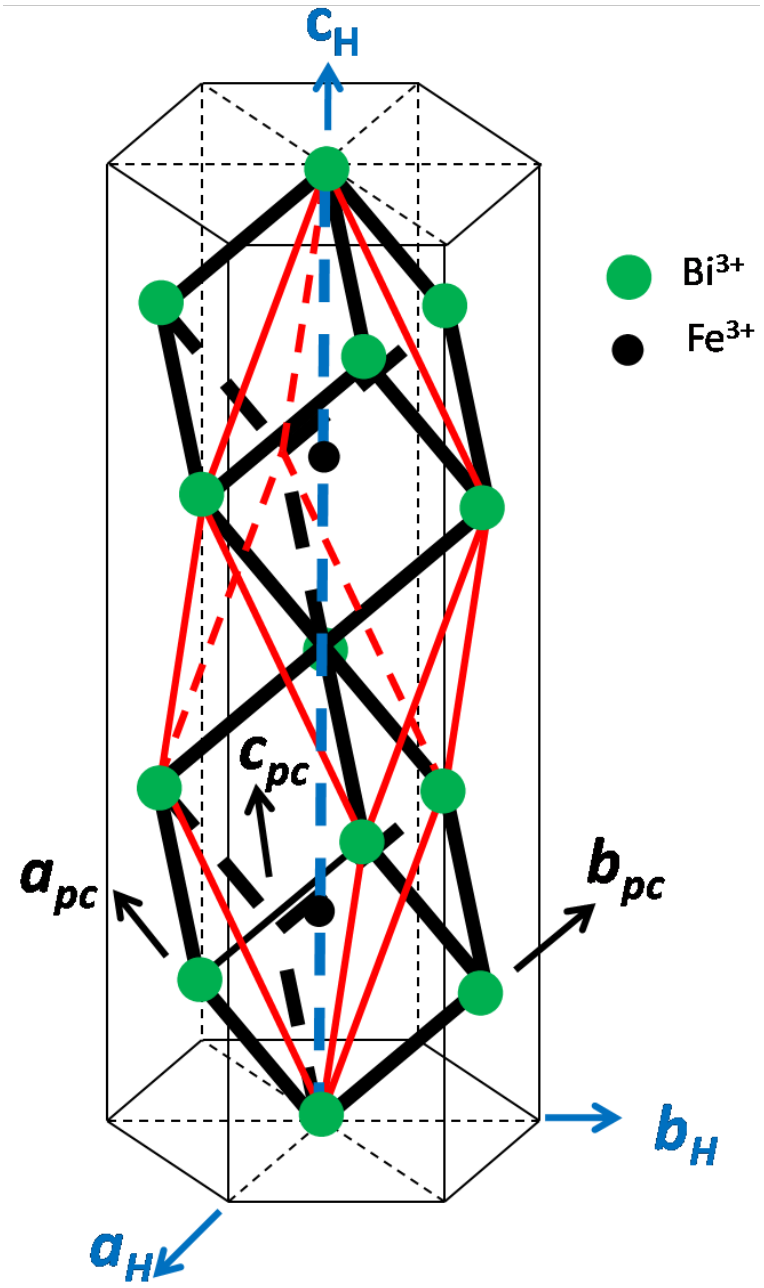

Figure 1.4 Schematic diagram of the crystal structure of BFO in hexagonal unit cell, rhombohedral unit cell (thin lines) and pseudocubic (*pc*) unit cell (thick lines).

The ferroelectric polarization of BFO is along the body diagonals of pseudocubic perovskite unit cell, which is the [001] direction in hexagonal unit cell. As the ferroelectric Curie temperature of BFO is very high, about 1100 K [26], it is estimated

to exhibit a large polarization. However, early work on single crystal BFO yielded only very small values of electric polarization (~ 6 μC/cm^2) [26]. The authors explained that their samples were not in saturation of polarization owing to large leakage. The first experimental confirmation of the large remanent polarization was done by Wang et al. in 2003 [27]. The follow-on works on single crystal [28] and ceramics [29] have also demonstrated the intrinsic ferroelectric behaviour of rhombohedral BFO, with approximately 100 μC/cm^2 along [111] in pseudocubic unit cell and 60 μC/cm^2 projected to [001] oriented epitaxial film or single crystal. This large polarization has also been predicated by the first principle calculation, which is in agreement with the experimental results [7].

BFO is a G-type antiferromagnet, in which each Fe^{3+} spin is surrounded by six nearest antiparallel spins [30]. The magnetic phase transition temperature, Neel temperature, is about 643K [27]. Due to local magnetoelectric coupling, the spins possess a weak canting moment instead of being perfectly antiparallel. This leads to a long-range superstructure of an incommensurate spin cycloid with a repeat distance of about 62 nm. In the first report by Wang et al. [27], it was shown with a very large magnetic moment of about 1.0 Bohr magneton (μ_B) per unit cell. However, later works have confirmed that the intrinsic magnetization of thin films is about 0.02 μ_B/cell [11, 31]. The first reported value was due to large concentration of oxygen vacancies in the

sample. The weak magnetic properties impede the device applications of BFO. To improve the magnetic properties, numerous works have been done by doping rare earth elements or by forming solid solutions with ferromagnetic phases [32, 33].

The attractive point of BFO as a piezoelectric material as compared to the widely used $Pb(Zr,Ti)O_3$ is its lead free in composition and therefore environmentally friendly. Its piezoelectric coefficient d_{33} value is about 70 pm/V [27], which is much smaller than those of other perovskite compounds (100-1000 pm/V) [12]. A morphotropic phase boundary (MPB) has recently been reported in $(Bi, Sm)FeO_3$ solid solution, showing a higher d_{33} value of about 110 pm/V at 14% of Sm [34]. It is likely that similar behaviour at MPB between BFO and other orthorhombic ferrites may also exist, which could potentially enhance the piezoelectric property of BFO.

As a result of the spin cycloid in BFO, the linear ME coupling between polarization and magnetization is averaged to zero [12]. The observed ME coupling is however of higher order. The ME coupling coefficient is about 3 V/cm Oe at zero magnetic field [27]. Zhao et al. have reported a correlation between the ferroelectric and antiferromagnetic domains [35]. The magnetic-easy plane can be changed by switching the polarization by 180°, which shows the possibility of electric control of magnetization in single phase mangetoelectric materials.

Recently, an interesting new phenomenon of BFO-diode effect was reported by T. Choi et al. [36]. The direction of diode effect of a single crystal BFO of single domain can be reversibly controlled by switching the ferroelectric polarization. A substantial photovoltaic current was also observed under the illumination of a linearly polarized light. This opens a new possibility of combing ferroelectric and semiconducting properties of this material, further increasing the multi-functional applications of BFO. For the photovoltaic effect of BFO epitaxial thin films, above bandgap voltage was reported with proposed new photovoltaic origin from domain walls [37]. However, the evidence of bulk photovoltaic effect was also reported in BFO thin films [38, 39]. Indeed, the research in this field of ferroelectric photovoltaic mechanism is still in the initial stage at this moment and improvement of performance is required for the practically useful application in solar energy conversion.

1.3 Literature Review

1.3.1 Strain Engineering of Ferroelectric Thin Films

Strain, a second-rank tensor describing the deformation of a material, is a very important parameter to tune the crystal structure and ferroelectric properties of

epitaxial thin films. This is known as “strain engineering” of ferroelectric thin films. The successful growth of highly quality ferroelectric thin films on suitable substrates has demonstrated that appropriately strained ferroelectric thin films can exhibit properties that are much better than those of their bulk counterparts [40]. For epitaxial layers, with in-plane lattice fully strained on single crystal substrates, the in-plane misfit strain is defined as

$$\varepsilon = \frac{a_{substrate} - a_{bulk}}{a_{bulk}}. \tag{1.7}$$

Depending on the relative size of the lattice between film and substrate, the misfit strain can be either compressive with a negative ε or tensile with a positive ε. Besides the lattice mismatch between film and substrates, the different thermal expansion coefficient can also give rise to strain, as most of the films undergo heat treatment during growth and annealing.

The quality of the single crystal substrates affects the film quality and orientation. Previous research on high temperature superconductors and semiconductors stimulated the development of perfect single crystal substrates with perovskite structure. Table 1 gives a list of substrates for the epitaxial growth of ferroelectric thin films, with the misfit strain with BFO given. With these high quality substrates available, a lot of work has been done on the strain engineering of both BFO and other ferroelectric materials, which will be reviewed in detail in the next section.

Table 1 List of available substrates for epitaxial growth of ferroelectric thin films

Substrates	Structure	Lattice parameters (Å)			Misfit strain
		a	b	c	BFO
$NdCaAlO_4$	Tetragonal	3.685	3.685	12.12	-7.0%
$YAlO_3$	Orthorhombic	3.69	3.69	3.69	-6.9%
$LaSrAlO_4$	Tetragonal	3.755	3.755	12.6	-5.2%
$LaAlO_3$	Rhombohedral	3.79	3.79	3.79	-4.4%
$SrLaGaO_4$	Tetragonal	3.843	3.843	12.68	-3.0%
$NdGaO_3$	Orthorhombic	5.426	5.496	7.707	-2.8%
LSAT	Cubic	3.868	3.868	3.868	-2.4%
$SrTiO_3$	Cubic	3.905	3.905	3.905	-1.5%
$DyScO_3$	Orthorhombic	5.440	5.717	7.903	-0.5%
$TbScO_3$	Orthorhombic	5.466	5.731	7.917	-0.1%
$GdScO_3$	Orthorhombic	5.480	5.746	7.932	+0.1%
$KTaO_3$	Cubic	3.989	3.989	3.989	+0.6%
$SmScO_3$	Orthorhombic	5.527	5.758	7.965	+0.7%
$NdScO_3$	Orthorhombic	5.575	5.776	8.003	+1.2%
MgO	Cubic	4.216	4.216	4.216	+6.3%

Previous studies on strain effect on ferroelectrics

The effect of strain on ferroelectric properties of materials has been widely reported in the literature. Here we focus on reviewing a couple of typical examples. Epitaxial tensile strain of 1% from $DyScO_3$ substrate has been shown to increase the Curie temperature by hundreds of degrees and produce room temperature ferroelectricity in otherwise paraelectric phase $SrTiO_3$ [41]. This is a good example of inducing new

property and phase by strain at room temperature, as the strain drives the paraelectric phase to ferroelectric phase. The high dielectric constant of $SrTiO_3$ thin film at room temperature and its electrical field dependence promise future device applications. In the prototypical ferroelectric material $BaTiO_3$, compressive strain greatly enhances the tetragonal *c/a* ratio and ferroelectric polarization [36]. There is a 250% increase in polarization and 500 ℃ increase in transition temperature of $BaTiO_3$ thin film under only 1.7 % compressive strain, demonstrating the strong sensitivity of ferroelectric properties on strain state. A further example of strain effect on ferroelectric behaviour is the development of superlattices, which are formed by alternating growth of epitaxial layers of two or three materials. Superlattices provide the potential to grow coherent films at larger thickness than epitaxial single layer film, because the superlattice structure impedes the formation of dislocations. Bousquet et al. [42] reported the improper ferroelectricity in $PbTiO_3$- $SrTiO_3$ superlattice with large temperature independent dielectric constant, which is different from $PbTiO_3$ and $SrTiO_3$.

Theory and simulation on strain effect on ferroelectrics

To understand the strain effect, various theoretical approaches have been developed, in which the first principles calculation and phase field simulation based on Landau

theory are most widely used [40]. The advantage for the first principles calculation is that it can predict the atomic arrangement in the unit cell and ferroelectric properties without input of experimental data. However, this method can only handle the calculation of less than 100 atoms, which is not able to reach the macroscopic ferroelectric domain level. With the input results from the first principles calculation, the phase field simulation can predict the domain configuration and ferroelectric properties and their dependence on temperature, strain, electrical boundary conditions [43-45].

The theoretical models not only help the experimentalists to interpret the experimental data, but also indicate new research directions by precise prediction of new physical properties within available experiment conditions. For examples, as mentioned above, the ferroelectric behaviour of $SrTiO_3$ thin film at room temperature is first predicted by Perstev et al. [46] and then demonstrated experimentally by Haeni et al. [41]. The strain-phase diagram, which gives the information on the effect of biaxial strain and temperature on ferroelectric transitions and domain structures, has been theoretically predicted for $BaTiO_3$, $PbTiO_3$, $Pb(Zr_{1-x}Ti_x)O_3$ thin films [45, 47]. The development of new algorithms and improvement of calculation ability of computers will continue to advance the basic understanding and help to pave the way for experimental ferroelectric studies.

Strain engineering of $BiFeO_3$ epitaxial thin films

The first experimental demonstration of large ferroelectric polarization of 60 $\mu C/cm^2$ for BFO is from epitaxial thin films [27], which is ten times larger than the bulk BFO single crystals previously reported [26]. This fact naturally drives the authors to believe that it is the enhancement from the strain effect, as the BFO film is grown on STO substrates with a misfit compressive strain of 1.5%. However, the similar polarization value reported later in high quality single crystals and ceramics demonstrates the large polarization is the intrinsic behaviour of BFO [28, 29]. In addition, the first principles calculations also predicted the strain independence of rhombohedral phase BFO epitaxial thin films within the stain range of $\pm 3\%$ [48].

Although the strain does not greatly improve the ferroelectric performance of rhombohedral phase, BFO does show a rich phase diagram for strain varying from -7% to +7%. In epitaxial thin films, BFO crystal structure could be stabilized in several different crystal systems, including monoclinic (M_A, M_B & M_C), tetragonal, rhombohedral, orthorhombic and even triclinic. This drives BFO as an ideal model material for the strain engineering study. In Figure 1.5, the summary of strain phase diagram is given for (001) oriented BFO epitaxial thin films. With increasing in-plane compressive strain, the BFO phase changes from monoclinic M_A to monoclinic M_C and Tetragonal (T) phase. The enhanced tensile strain drives BFO from monoclinic M_A

to M_B, then to Orthorhombic (O) phase. In the next section, detailed review on the crystal structures for each of these BFO phases will be presented.

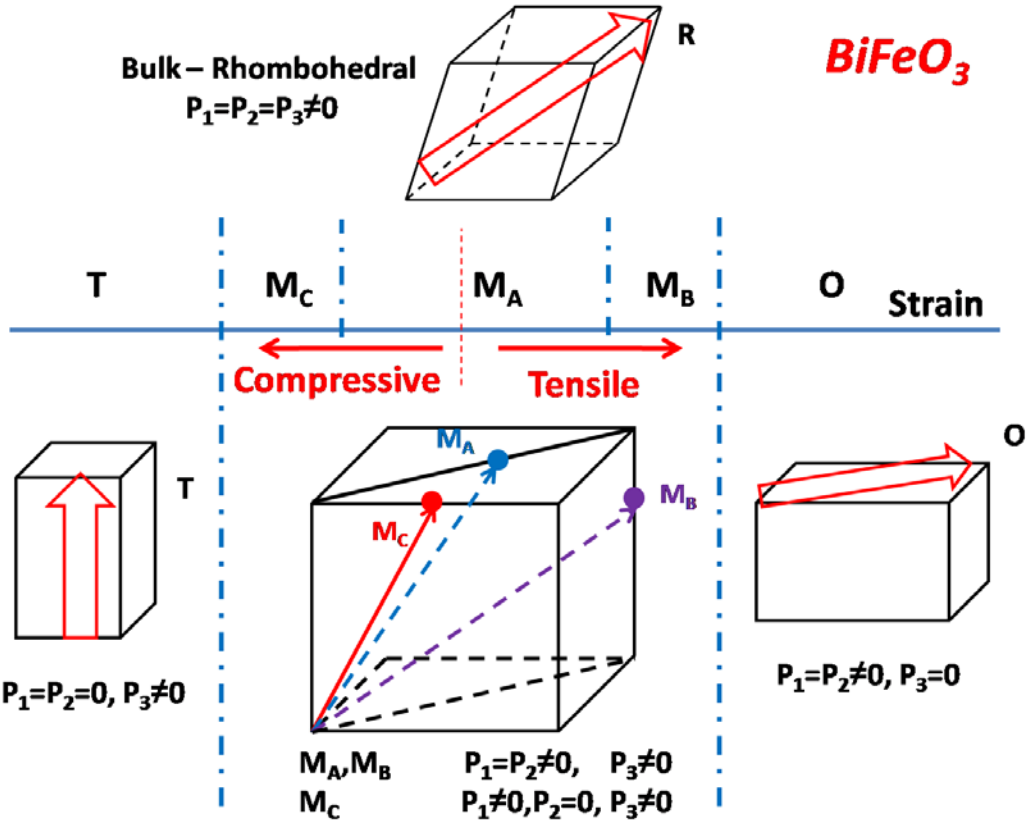

Figure 1.5 Strain phase diagram of epitaxial BFO films in (001) orientation.

1.3.2 Crystal Structure of Epitaxial Bismuth Ferrite Thin Films

For ferroelectric materials in monoclinic phase, three types of monoclinic structure have been classified according to their space groups and polarization directions [49]. M_A and M_B phases belong to the space group of *Cm*, while M_C phase has a space

group of *Pm*. The differences among these three monoclinic structures are illustrated in Figure 1.6. For M_A and M_B phases, the monoclinic distortion is along the [110] direction of the pseudocubic lattice, which are shown by the arrow in Figure 1.6 (a). This leads to the in-plane lattice parameters of monoclinic phase to be around $\sqrt{2}$ times of the pseudocubic cell. For M_C phase in Figure 1.6 (b), the monoclinic distortion is along the [100] direction of the pseudocubic lattice, resulting in a similar lattice dimension of M_C lattice with the pseudocubic lattice. The difference between M_A and M_B phase is shown in Figure 1.6 (c). The M_A phase is formed when the in-plane strain is compressive, while the M_B phase is produced in tensile strain condition. This gives rise to $a/\sqrt{2}c < 1$ for M_A phase and $a/\sqrt{2}c > 1$ for M_B phase. This notation of these three monoclinic phases will be used through this thesis.

Monoclinic M_A and tetragonal phase under small compressive strain

The most extensively studied BFO epitaxial thin films are grown on cubic STO (001) single crystal substrates. The compressive epitaxial strain of ~ 1.5% from STO substrates contracts the in-plane lattice and elongates the out-of-plane lattice constants. For the in-plane fully strained film with film thickness of less than 50 nm, the coherent constraint from cubic STO lattice forces BFO to be in tetragonal symmetry [10]. This tetragonal phase has a small *c/a* ratio around ~ 1.04, as compared to the giant *c/a* ratio

around ~ 1.25 of the super-tetragonal BFO phase [50]. As the film thickness increases, the in-plane compressive strain relaxes and the crystal structure has a tendency to shift back to the low energy bulk rhombohedral phase. In the thickness range of hundreds of nanometers, the partially relaxed film shows a monoclinic M_A structure, which was demonstrated by the unique splittings of diffraction peaks in reciprocal space mappings (RSMs) [10, 51]. Finally, for the very thick film of around 2 μm, the substrate strain is fully relaxed and the crystal structure changes back to the bulk rhombohedral structure[50].

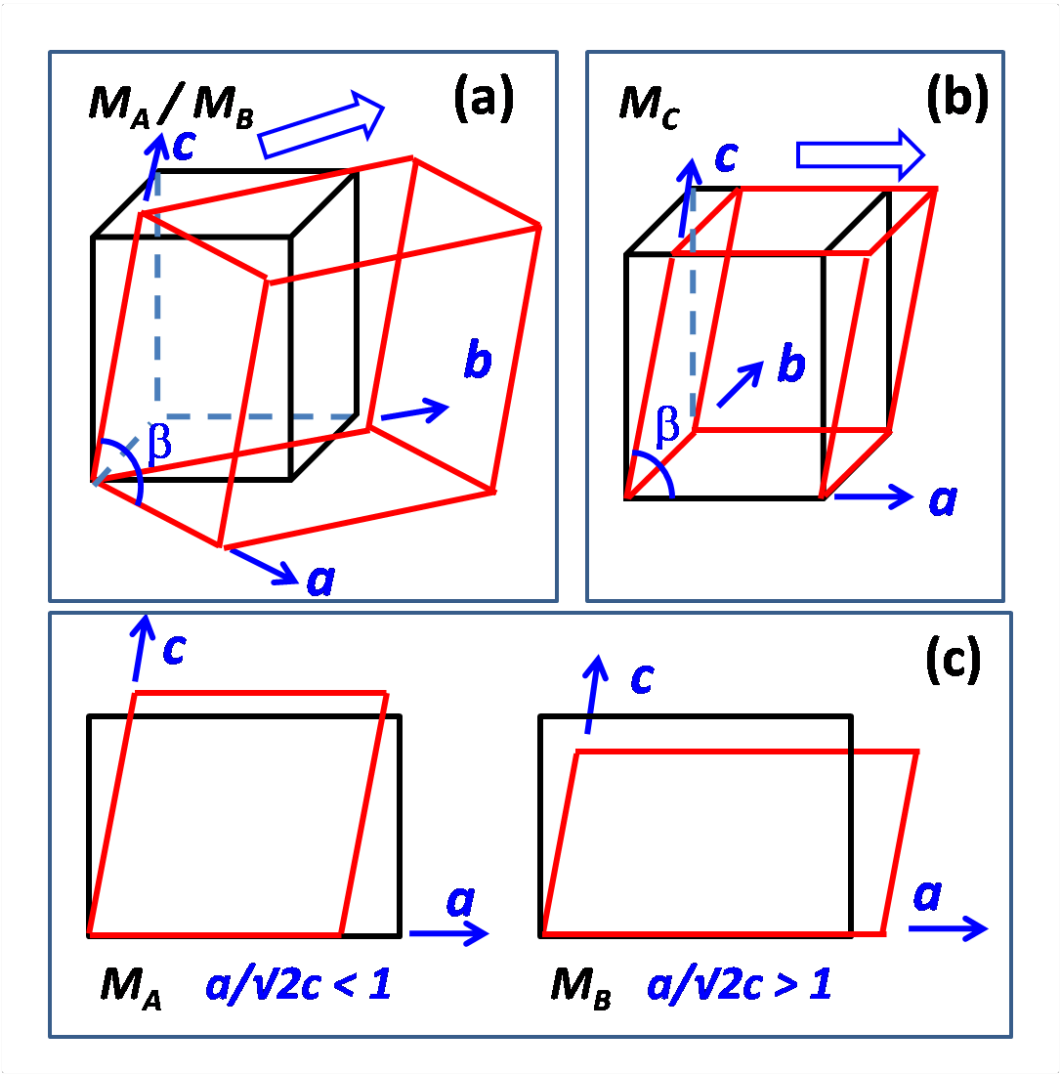

Figure 1.6 The monoclinic distortion from high symmetry cubic unit cell for M_A and M_B phase (a) and M_C phase (b). The cross sectional view of lattice in *ac* plane, showing the difference between M_A and M_B phase (c).

Monoclinic M_C and super-tetragonal phase under large compressive strain

Larger compressive strains of ~ 4.5 % elongate the out-of-plane dimension of the BFO lattice greatly, from 4 Å to 4.6 Å, for BFO epitaxial thin films grown on $LaAlO_3$ (LAO)

(001) and $YAlO_3$ (YAO) (110) substrates [52]. For BFO films deposited on LAO substrate, both Raman and X-ray studies show a monoclinic distortion for BFO lattice, which gives a M_C structure [50, 53]. This M_C phase is called "tetragonal-like"[52], because it has a similar unit cell and a big out-of-plane lattice constant of around 4.6 Å. With similar reasons, M_A phase is called "rhombohedarl-like" because of the close unit cell dimensions with bulk rhombohedral phase. According to the first principle calculations, a super-tetragonal BFO phase with giant *c/a* ~ 1.25 could be formed at in-plane compressive strain above 4.5 % [54]. It is expected that the BFO film with strict tetragonal symmetry with *P4mm* space group can be obtained on substrates with in-plane lattice parameter smaller than LAO. Experimentally, it was found that Ba-doped BFO film is in super-tetragonal phase on LAO substrate, as a result of the additional stress from chemically doping of Ba atom with larger atomic radius [50].

Monoclinic M_B and orthorhombic phase under tensile strain

Having studied the compressively strained BFO films, scientists are looking at the possibility of developing new phases and novel properties at the tensile strain side of BFO epitaxial thin films. Tensile strain leads to the shrinkage of the out-of-plane dimension and elongation of the in-plane length of BFO lattice. Monoclinic M_B BFO phase could be formed under a small tensile strain from substrates like $SmScO_3$ and

$NdScO_3$ [55]. While an extremely large tensile strain of around 8% could lead to an orthorhombic phase in *Ima2* space group with only in-plane polarization, as predicted by first principles calculations [56]. To create such large tensile strain, MgO is the only available substrate with the largest in-plane lattice constant, as can be seen from Table 1. However, the BFO film deposited on MgO substrates show a low crystallinity and poor epitaxial quality, due to the mismatch of perovksite structure of BFO with rock-salt structure of MgO [57]. Until now, this predicted orthorhombic phase has not been demonstrated experimentally.

Monoclinic M_B and orthorhombic phase under compressive strain in (110) orientation

Although most of the epitaxial BFO thin films reported in the literature are grown in (001) directions, substrates with other orientation strain the film in different ways, which may produce new crystal phases, domain structures and improved properties [58]. For BFO films with the film thickness of ~200 nm grown on STO substrates with (110) orientation, experimentally the structure was determined to be a ground state M_B phase [59]. However, a recent first principles calculation predicted two paraelectric orthorhombic phases for compressive strained BFO films in (-110) orientation [60]. The first phase transition from monoclinic *Cc* phase to orthorhombic *Pnma* phase

occurs as the compressive strain in (-110) orientation increases to 1.6%. Interestingly, this *Pnma* phase is the same as the high temperature paraelectric phase of BFO as proven by temperature dependent structure studies by neutron diffractions [61]. This is a strain driven paraelectric phase of BFO from ferroelectric phase, as a reverse example of what happened in STO thin films [41], showing the strong effect of strain on ferroelectric properties. The second phase transition under compressive strain of around 7% in (-110) orientation produces a new orthorhombic phase $P2_12_12_1$, which is also a paraelectric phase without ferroelectric polarization in any direction. More experimental results for BFO films in (110) orientation are expected to confirm these prediction of new phases, as well as novel properties. The investigation into the orthorhombic phase is indeed only in its infancy, with fascinating stories being expected in the near future.

Rhombohedral phase under compressive strain in films with (111) orientation

Bulk BFO exhibits a *R3c* space group with the rhombohedral symmetry [24]. The rhombohedral distortion of perovskite structure can be seen as the elongation along the (111) direction of cubic unit cell. Therefore, the strain along (111) direction only modifies the lattice constant while the crystal symmetry will remain as rhombohedral as the 3-fold symmetry axis is not destroyed. Experimental structural study on BFO

films deposited on STO (111) substrates shows indeed a rhombohedral phase with lattice constants very close to bulk BFO [20]. Unlike BFO films in other orientations with complex domain structure, the rhombohedral phase in thin film form has only a single domain without any ferroelectric or ferroelastic domain walls, which is an ideal platform to study the intrinsic properties of BFO [58].

1.3.3 Ferroelectric Property of Epitaxial Bismuth Ferrite Thin Films

Ferroelectric behaviour of bulk $BiFeO_3$ single crystal

Bulk single crystals are commonly employed to study materials' properties, as they are simple compared to ceramics and thin films. Before looking at the ferroelectric behaviour of BFO thin films, it would be useful to review the studies on single crystals.

The first work on the ferroelectric behaviour of BFO single crystal was done in 1970, where a spontaneous polarization of 3.5 $\mu C/cm^2$ along <001> direction of pseudocubic unit cell was measured [26]. This value is surprisingly small as the ferroelectric Curie temperature is high and the atomic displacement is large for BFO. The authors claimed that the hysteresis loop was not well saturated due to the high leakage of their sample.

The growth of high quality single crystal of BFO was not of much interest to scientists until the report of a large spontaneous polarization of 50 $\mu C/cm^2$ along <001> direction in epitaxial thin films [27]. Due to the highly volatile Bi, the composition of single crystal BFO is difficult to control. The parasitic phases produced during single crystal growth lead to high conductivity which prevents the ferroelectric measurement. In 2007, Lebeugle et al. reported a polarization value close to 60 $\mu C/cm^2$ along <001> direction in BFO single crystal with high electrical resistivity [28]. This work serves as a sound evidence for the intrinsic ferroelectric property of BFO. Later in 2011, a new laser-diode heating floating-zone method was developed to grow highly insulating BFO single crystals [10]. The corresponding ferroelectric measurement also confirmed the large spontaneous polarization.

Ferroelectric behaviour of monoclinic phase $BiFeO_3$ thin films

The current on-going intensive interest with BFO is mainly stimulated by the Science paper published in 2003 by Ramesh's group [27], which demonstrated an unexpected large polarization and multiferroic behaviour of BFO epitaxial thin films at room temperature. In their work, the BFO epitaxial thin films were grown on $SrRuO_3$ (SRO)-buffered $SrTiO_3$ (STO) (001) single crystal substrates. The crystal structure of BFO is distorted from bulk rhombohedral to monoclinic phase due to the cubic lattice

of substrate. Initially, the large polarization measured in BFO epitaxial thin film was considered to be the strain effect, as previous bulk single crystal only produced 15 times smaller polarization value. However, the thickness independence of polarization [62] and similar large polarization measured in high quality BFO single crystals [28] confirm that the strain does not play a critical role here. Instead, the large polarization value is an intrinsic behaviour of BFO.

Ferroelectric behaviour of super-tetragonal phase $BiFeO_3$ thin films

An interesting phase of BFO thin film is the super-tetragonal phase. This phase is called super-tetragonal because it has a giant *c/a* of ~1.25, much larger than ~1.05 for the normal tetragonal phases. This giant tetragonal ratio would lead to a giant polarization value of ~150 $\mu C/cm^2$ along <001> direction from theoretical calculations [54], almost three times larger than that of the monoclinic phase.

There are two approaches in the literature to obtain this super-tetragonal phase. The first approach is to grow films at high growth rate. Yun et al. [38] reported a giant polarization of ~150 $\mu C/cm^2$ in polycrystalline BFO films deposited on Si substrates at temperature of 90 K. To identify the origin of this giant polarization, they deposited epitaxial BFO thin film on STO substrates and found that high growth rate would give

rise to a tetragonal phase with *c/a* of ~1.26 [63]. From the first principle calculations, the authors suggested that this giant tetragonal *c/a* ratio should produce large ionic off-centering, resulting in the giant polarization. The second approach is strain engineering. In fact, the super-tetragonal phase of BFO is a fascinating example of the power of strain engineering. Above the compressive strain of ~ 4.5%, the lowest energy phase for BFO epitaxial thin films would change from monoclinic to super-tetragonal phase [52, 54]. The out-of-plane lattice parameter increases from 4.0 Å to 4.6 Å in association with this phase transition, leading to giant piezoelectric strain [52]. The first attempt to characterize the ferroelectric behaviour of this super-tetragonal phase measured a polarization value of only ~75 $\mu C/cm^2$ [64], where the authors attributed the low polarization value to high leakage of thin film sample. In a more recent work [65], a polarization value around ~130 $\mu C/cm^2$ was reported in a film consisting mixture phase of tetragonal-like and rhombohedral-like BFO phases. From a linear extrapolation, the polarization value for super-tetragonal phase BFO is ~150 $\mu C/cm^2$, which agrees with the theoretically predicted value [54]. The research on super-tetragonal BFO films is still an on-going topic , as the giant polarization would provide opportunities to improve the device performance, such as in ferroelectric memories and ferroelectric tunnel junctions.

1.3.4 Concluding Remarks

Since the breakthrough with multiferroic epitaxial thin films reported in 2003, BFO thin films have attracted considerable attention due to the unique ferroelectric, magnetic, and magnetoelectric coupling behaviour. Although a large amount of work has been done with the epitaxial BFO thin films, there are still several outstanding issues that have not been properly clarified and well understood.

i) There are still considerable controversies about the crystal structures of BFO thin films deposited on STO (001) substrates. For example, a fully relaxed and bulk-like rhombohedral structure for BFO films deposited by liquid-phase epitaxy was reported by Qi et al [66], while Xu et al. has observed that a monoclinic structure exists in the film grown by pulsed laser deposition [51].

ii) The strain effect on ferroelectric behaviour of BFO film on STO (001) substrates is not fully understood. Kim et al. have demonstrated that the polarization was almost unchanged when strain relaxes with increasing film thickness of (001) BFO films grown on $SrTiO_3$ (STO) substrate [62]. However, Jang et al. have reported that there was a strong strain dependence of polarization in BFO (001) thin films due to the polarization rotation [40].

iii) There is rather limited understanding of the super-tetragonal phase formed on STO (001) substrates. For example, the first principles calculation claimed that it was highly unlikely to form the super-tetragonal phase with a giant *c/a* on STO substrate [54]. However, when grown by Pulsed Laser Deposition on STO substrates, the formation of the super-tetragonal BFO structure has been experimentally reported when the growth rate was increased by changing laser frequency from 5 to 15 Hz [63].

iv) The origin of forming the super-tetragonal BFO phase on STO (001) substrates has not been properly studied. From the results of theoretical calculations, this super-tetragonal phase was identified as a stable phase only under high compressive strain of above ~ 4.5% [54]. However, STO substrate can generate a compressive strain of only ~ 1.5%. Beside strain, there are other possible formation parameters for this super-tetragonal BFO phase deposited on STO substrates.

v) The strain driven formation of strictly super-tetragonal phase has not been experimentally demonstrated. Most of the previous reports on highly compressive strained BFO films are deposited on LAO (001) substrates with a lattice mismatch of ~ 4.5 %. However, the BFO crystal structure on LAO exhibits a tetragonal-like

but strictly monoclinic M_C structure [52, 64]. The question is whether it is possible to form the strict super-tetragonal BFO phase on substrates with a larger compressive strain than LAO.

1.4 Purpose of Research

This thesis aimed at making thorough understanding on the crystal structures of epitaxial BFO thin films, and clarifying the relationship between strain, crystal structures and their ferroelectric behaviour. The specific objectives are:

i) To understand the crystal structures and thickness dependent ferroelectric behaviour of BFO thin films grown on STO (001) substrates,

ii) To clarify the formation mechanism of super-tetragonal phase BFO on STO substrates,

iii) To explore the crystal structures of highly strained BFO films deposited on substrates with large compressive strain above ~4.5%.

In order to achieve these objectives, high quality BFO epitaxial thin films have to be firstly grown by optimizing the sputtering parameters. The crystal structures were then studied by high resolution X-ray diffraction at synchrotron light source and Transmission Electron Microscopy, followed by the characterization for their

ferroelectric properties by the standard electrical measurement of ferroelectric hysteresis behaviour.

The chapters in this thesis are organized as follows. While a brief review has been made in Chapter 1, the film deposition method and basic operation principles of characterization techniques will be introduced in Chapter 2, where the effect of each sputtering parameter on epitaxial film quality will be discussed. In Chapter 3, the crystal structures of BFO films on STO substrates are studied by high resolution synchrotron X-ray diffraction. In addition, the strain effect on ferroelectric polarization is investigated by the thickness-dependent study. In Chapter 4, the growth-rate induced monoclinic to super-tetragonal phase transition will be presented for BFO films on STO substrate. Moreover, the role of parasitic β-BO phase in the formation of super-tetragonal BFO phase will be studied through a detailed structure analysis. Chapter 5 presents the structure evolution of BFO films on high compressive substrates, aiming at examining the strain phase diagram predicted by the first principles calculations. Chapter 6 summarizes the whole thesis and provides ideas for the future work.

The results obtained in this study present a significant advance on the understanding of crystal structures and ferroelectric behaviour of BFO epitaxial thin films. The structural

study from synchrotron X-ray diffraction contributes to clarify the crystal structure of different BFO phases. The investigation into ferroelectric behaviour provides useful information for novel device applications of BFO thin films, where they are tailored through changes in crystal structures. In addition, as BFO is a multifunctional material, the study of structural effect on magnetism and magneto-coupling behaviour of BFO can benefit from this work as well. Although the study in this thesis is only on BFO, it also sheds light on understanding and tuning the ferroelectric behaviour of other ferroelectric materials systems.

Chapter 2. EXPERIEMENTAL DETAILS

In this thesis, the epitaxial BFO thin films were deposited by using Radio Frequency (RF) Magnetron Sputtering system. The crystal structure was characterized by High Resolution X-ray Diffraction (HRXRD) and Transmission Electron Microscopy (TEM). Atomic Force Microscopy (AFM) was employed to study the surface morphology of as-deposited BFO thin films. The dielectric, ferroelectric and leakage behaviour of BFO thin films were measured by an Impedance Analyzer, a Radiant Technology precise system with a probe station and a Keithley current-voltage meter, respectively.

2.1 Deposition of Epitaxial $BiFeO_3$ Thin Films by Sputtering

$BiFeO_3$ target preparation by solid state reaction

The BFO ceramic targets were prepared by solid state reaction of Bi_2O_3 and Fe_2O_3 powders. Due to high volatility of Bi, 10% excess of Bi_2O_3 was added to compensate for the Bi loss during high temperature heat treatment. The general workflow of the experimental procedures is summarized in Figure 2.1.

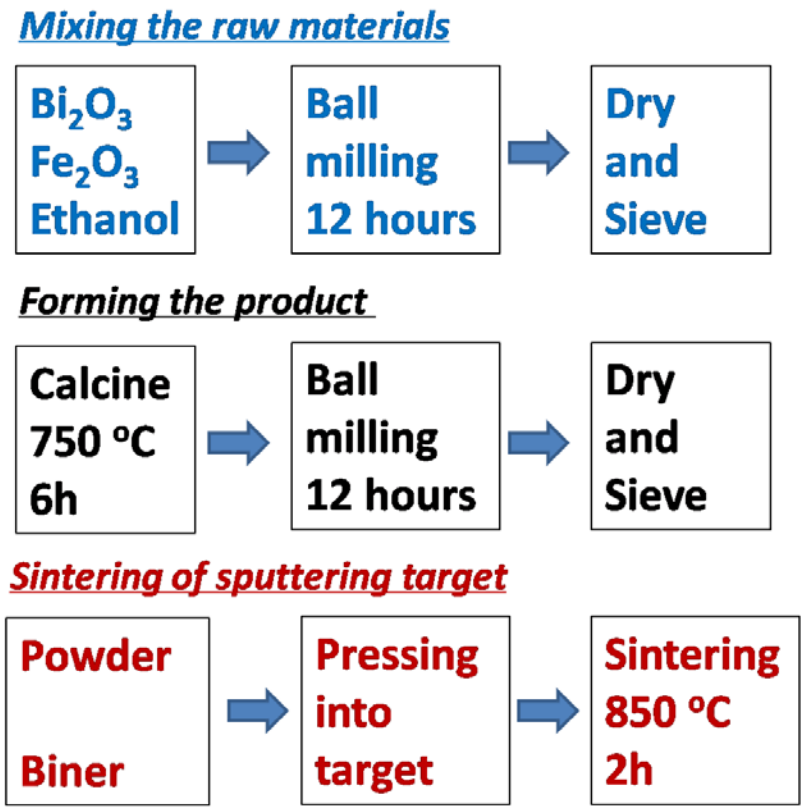

Figure 2.1 Experimental procedure of BFO target preparation

Introduction to RF sputtering

In this project, a RF magnetron sputter machine (Oerlikon Leybold Vacuum, Germany) was used to deposit the thin film samples. Figure 2.2 shows a schematic diagram of a RF magnetron sputtering system, which is adopted from [28]. It contains a vacuum chamber with sputtering guns, substrate holder with heater, gas supply and power supply system and the vacuum pumps.

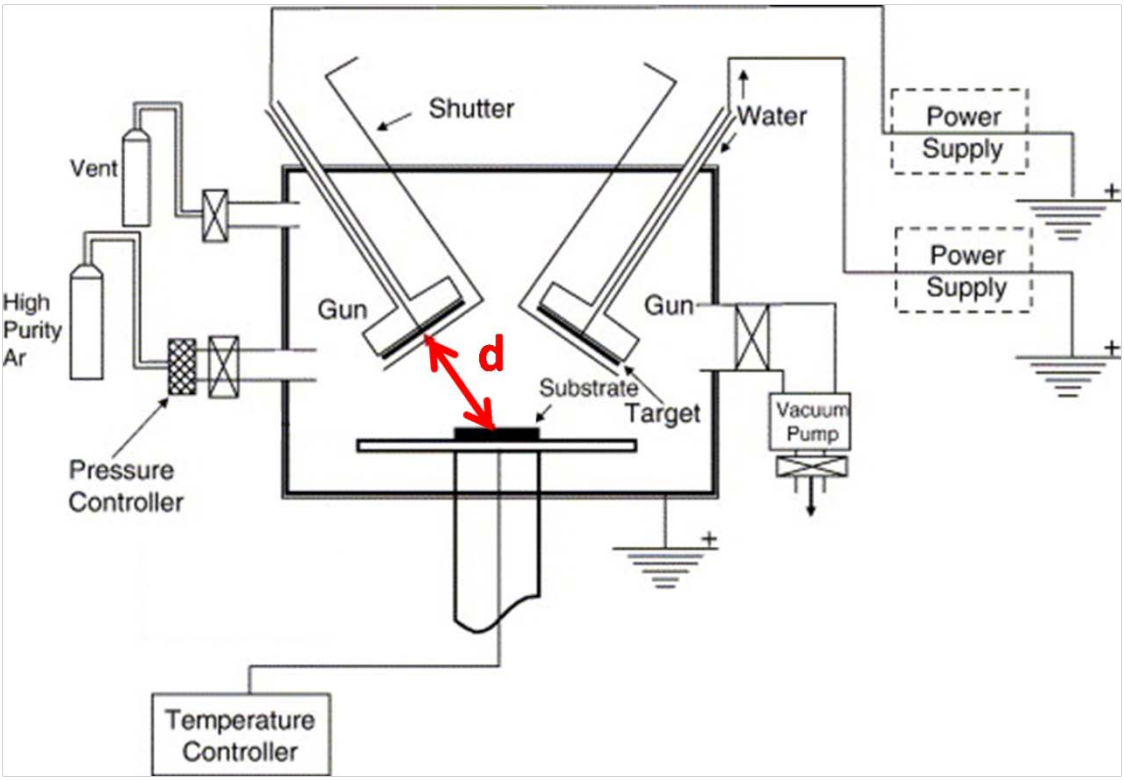

Figure 2.2 Schematic illustration of RF sputtering system. Figure adopted from [28].

Sputtering is the process of removing atoms from the surface of a target by kinetic-energy transfer from an incoming incident flux of highly energetic particles [67]. Before sputtering, the chamber has to be in high vacuum state by continuously pumping to remove air and water molecules. Typically, the vacuum chamber is pumped by a combination of turbo-molecular and mechanical pumps. During sputtering, the target is charged negatively, acting as a cathode. The ion gases, Ar^+, are accelerated towards the target with high kinetic energy, bombarding the target surface. The ejected neutral atoms fall on the substrate surface, migrate and condense to form a thin film layer. In order to improve the sputtering yield, magnetic field is employed to

confine the charged particles in the vicinity of the target. This is called magnetron sputtering, which increases the deposition rate by 10 to 100 times, as compared to basic diode sputtering method [68].

For sputtering of an insulating target, the conventional DC sputtering will not work. Because the positive charge will build up on the target surface, which rejects the positive Ar^+ flux and stops the sputtering process. In order to solve this issue, RF sputtering is developed, in which the electrical potential applied on the target is alternating at high frequency in radio frequency regime. The heavy Ar^+ cannot follow the RF field and respond only to the DC self-bias. Thus, the plasma discharge is maintained by this RF field.

Sputtering is commonly used in semiconductor industry, due to its ability to maintain the target composition and deposit large area of uniform thin films. As compared to other film deposition technology, such as Pulsed Laser Deposition (PLD) and Molecular Beam Epitaxy (MBE), the film growth by sputtering is very fast and the process is far away from thermal equilibrium. This high deposition rate tends to results in rough surface. However, smooth surface can be obtained by fine tuning of sputtering parameters.

Sputtering of epitaxial $BiFeO_3$ thin films

The general steps of growth of epitaxial BFO thin films by sputtering are as follows.

i) Substrate cleaning

Commercially available single crystal substrates often contain organic and inorganic residuals on the surface as a result of the polishing process. Before deposition of thin films, the substrates should be carefully cleaned. In this project, all the substrates are ultrasonically cleaned by successively immersing them for one minute in the solvent of acetone, ethanol, and De-ionized (DI) water. Finally, the substrates are dried with N_2 gun.

ii) Pre-sputtering

After the target and substrates being installed in the chamber, the system will be pumped down to vacuum with pressure less than 10^{-6} Torr. Then, the substrates will be heated slowly up to the growth temperature.

iii) Sputtering

Argon and oxygen gas are introduced to the chamber, in order to maintain a dynamic chamber pressure within the range for sputtering plasma to occur. Tune the sputtering power to the setting value, open the shutter, then the plasma can be

captured. Allow the film growth for the time duration required.

iv) Post-sputtering

After the deposition finishes, the shutter is closed, the substrates are then cooled down directly to room temperature. Finally, the chamber is vented with N_2 gas to atmosphere pressure for taking out the samples.

There are several parameters shall be tuned to produce the high quality epitaxial thin films, including temperature, O_2 pressure, Ar/O_2 ratio, sputtering power, and sputtering time. For the oxide thin films, high temperature growth is required in order to obtain crystallized films. The high temperature also improves the mobility of the deposited particles to the low energy positions. By applying silver paste to the back side of the substrates, a better contact with heating plate and more uniform temperature field can be achieved, which greatly improves the film quality. O_2 partial pressure controls the oxygen vacancies in the as-deposited films. Also, the crystalline phases of oxides are very sensitive to the O_2 partial pressure. The total sputtering pressure and the sputtering power determine the growth rate. The film thickness is controlled by varying the sputtering time. The standard sputtering parameters employed in this thesis are listed in the Table 2.

Table 2 Sputtering parameters of BFO and SRO films

Film	Temperature (°C)	Sputtering power (W)	Ar flow rate (Sccm)	O_2 flow rate (Sccm)	Deposition rate (nm/min)
$SrRuO_3$	680	70	240	80	~0.5
$BiFeO_3$	680	120	140	20	~3

2.2 High Resolution X-ray Diffraction of Epitaxial Thin Films

X-ray Diffraction

X-ray Diffraction (XRD) is a very useful tool to investigate the crystal structure of materials, as it has a wavelength in the same order of inter-atomic distance of crystals. Figure 2.3 illustrates the basic principle of Bragg's law in XRD. When two parallel incident X-ray beams interact with the atoms in the crystal, the X-ray beams are diffracted into a certain direction, forming an angle of 2θ with incident direction. The difference between the travel distances of two parallel X-ray beams is $2d\sin\theta$, in which d is the distance between two crystalline planes. For diffraction peaks to occur, this travel difference has to be an integer times of wavelength for constructive interference

of diffracted beams. This gives the Bragg's condition of diffraction

$$2d \sin\theta = \lambda . \qquad (2.1)$$

From the direction of diffraction beam, the lattice dimensions of the crystal can be derived from the Bragg's Law.

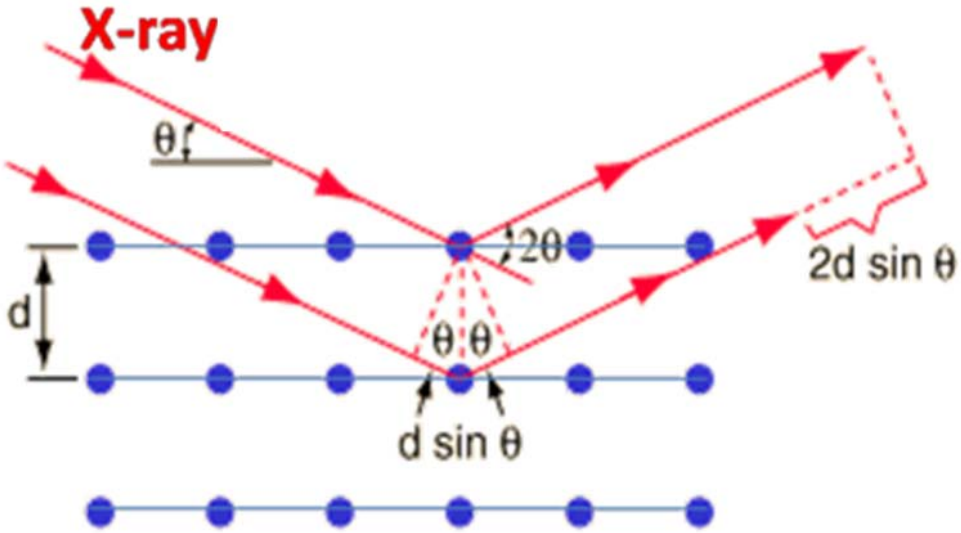

Figure 2.3 Schematic illustration of Bragg's law in X-ray diffraction

Four-Circle Diffractometer and Reciprocal Space Mapping

Normal powder X-ray diffraction can help to identify phases of a sample by comparing the diffraction peaks with the standard XRD card. However, for the proper characterization of epitaxial thin films, powder XRD is unable to provide enough information. To obtain both in-plane and out-of-plane lattice dimensions, the four circle X-ray diffractometer is required, as shown in Figure 2.4. There are four degrees

of freedom for this kind of diffractometer- ω, 2θ, χ, Φ, which are labeled in the figure. The sample can be rotated within horizontal plane, which gives the Φ circle. In addition, the sample stage can be tilted by the angle of ω along the X-ray beam direction and by the angle of χ perpendicular to the beam direction. The last circle is 2θ, the angle between the incident beam and diffracted beam, which is varied by the motion of detector.

With the flexibility of four circle diffractometer, several types of scans that are not available in powder diffraction can be achieved [69]. Figure 2.5 illustrates four basic scans in the reciprocal space by four circle diffractometer. The dots represent the diffraction peaks within the q_x-q_z plane in the reciprocal space. $\boldsymbol{k_1}$ and $\boldsymbol{k_2}$ are the incident and diffracted beam wave vector, respectively. The large semicircle shows the region of the available diffraction that can be measured at a certain value of X-ray wavelength, because outside the semicircle $\lambda/2d = \sin\theta > 1$, which is not possible. Within the two small semicircles, the diffractions are also not available due to the incident beam below surface for the left one and exit beam below surface for the right one. Hence, the diffraction peaks that can be measured in the reciprocal space are those in between the two small semicircles and the large semicircle.

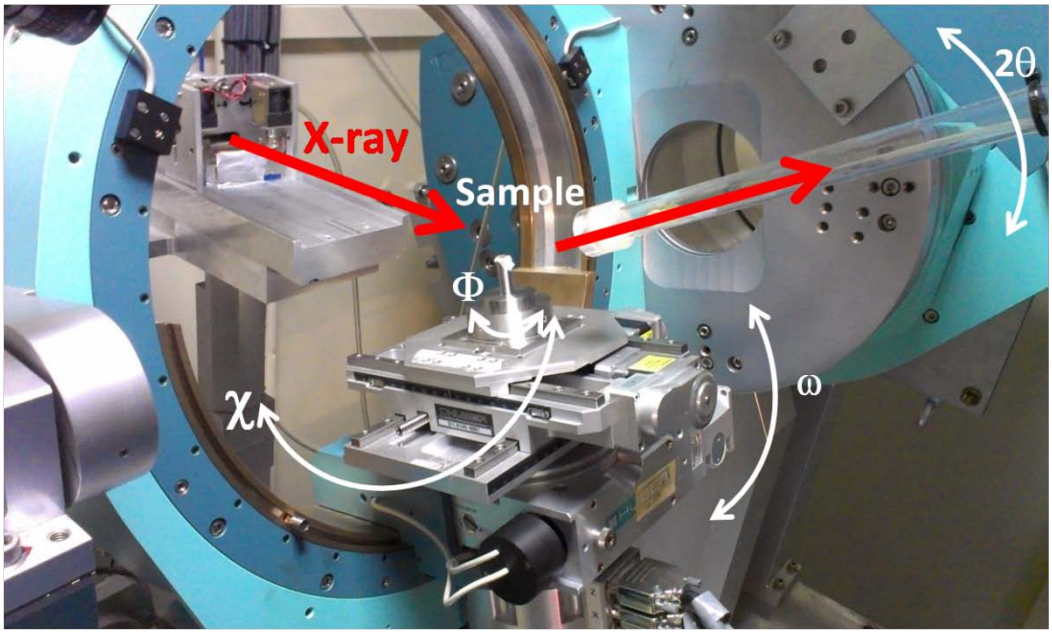

Figure 2.4 Four circle X-ray diffractometer in Singapore Synchrotron Light Source

For the first scan type in Figure 2.5, it is the specular scan along the q_z direction in the reciprocal space. During the scan, ω is fixed always to be half of 2θ in order to maintain the scan direction exactly along the q_z direction in the reciprocal space, as shown by the arrow in Figure 2.5. This is effectively the same scan as the $\theta/2\theta$ scan in the powder XRD. The second scan type is offset scan, in which ω is always kept as $(2\theta+\delta)/2$, where δ is a small deviation angle. This enables the scan direction tilt by $\delta/2$ from the q_z direction. The third scan type is detector scan, where only 2θ varies during the scan while ω is fixed. This gives the scan direction along a circle in the q_x-q_z plane, as shown by the curved arrow in Figure 2.5. The last scan type is rocking curve or ω scan. In this case, ω varies during the scan while 2θ is fixed, giving rise to a circle scan direction perpendicular to the radial direction in the reciprocal space. Combing any

two of these scans together, a *2D* area in the reciprocal space can be measured experimentally, which is known as the reciprocal space mapping.

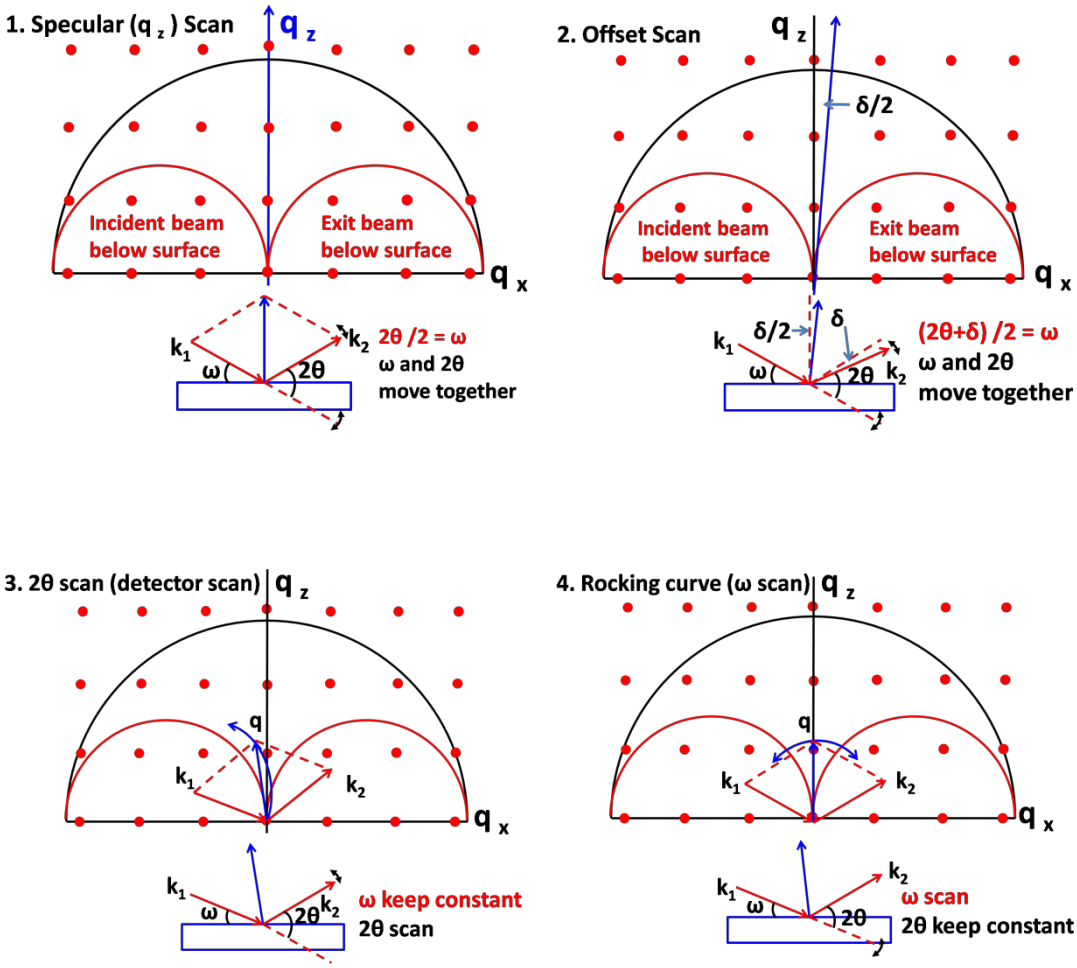

Figure 2.5 Schematic illustration of four basic scans in the reciprocal space by four circle X-ray diffractometer

Crystal System and Lattice Parameters Determination

From the diffraction peaks in reciprocal space mapping, the crystal symmetry can be determined, which gives the information of the crystal system. In the following description, monoclinic structure will be used as the example to illustrate the process of the analysis of crystal symmetry. The monoclinic unit cell has the lattice parameters $a \neq b \neq c, \alpha = \gamma = 90°, \beta \neq 90°$. Figure 2.6 (a) shows the schematic real space and the corresponding reciprocal space monoclinic unit cell in the vertical *(h0l)* plane. Due to the monoclinic distortion angle β in the *ac* plane, the real space unit cell can be either distorted to the left or right side. In addition, the *bc* plane gives a rectangular shape, resulting the three kind of unit cell shown in the first row in Figure 2.6 (a). From the relationship between the real space and reciprocal space,

$$a.a^* = b.b^* = c.c^* = 1. \tag{2.2}$$

$$a.b^* = a.c^* = b.a^* = b.c^* = c.a^* = c.b^* = 0. \tag{2.3}$$

the reciprocal space unit cell can be derived. It is clear that if the *(h0l)* reciprocal space mapping is measured for monoclinic structure, there will be three diffraction peaks. Two peaks from tilted *a* domains as a result of the monoclinic distortion and the other one from the *b* domain. From similar analysis shown in Figure 2.6 (b), two diffraction peaks will occur in the *(hhl)* reciprocal space mapping for monoclinic structure. Therefore, the monoclinic crystal structure has a signature diffraction pattern of three peaks in *(h0l)* and two peaks in *(hhl)* reciprocal space mapping.

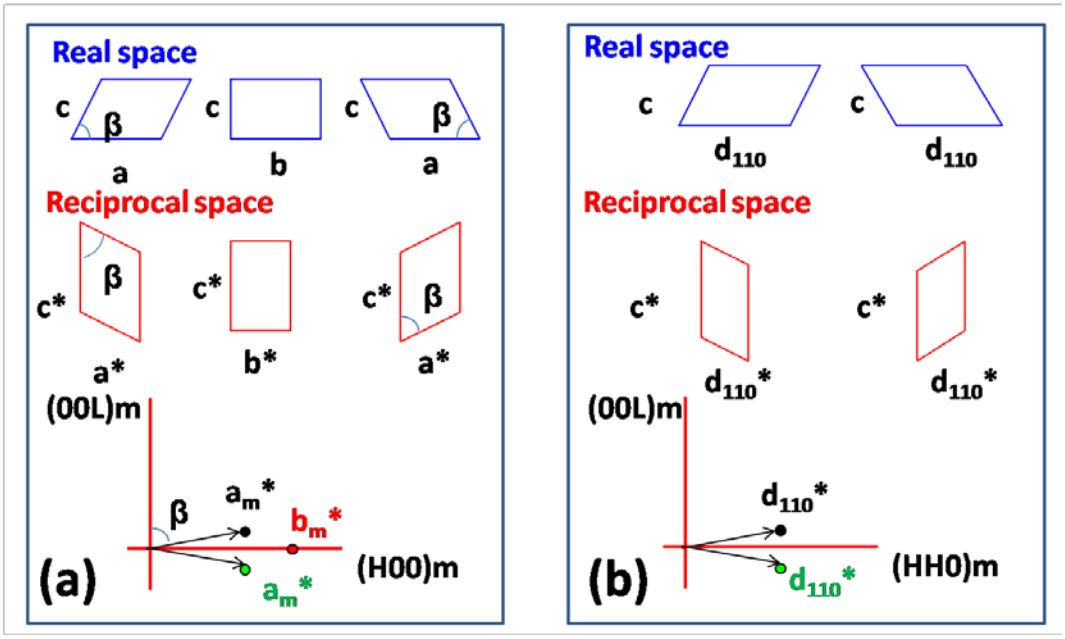

Figure 2.6 Schematic diagram of monoclinic phase in reciprocal space mapping for *HL* plane (a) and *HHL* plane (b)

In the reciprocal space mappings using pseudocubic lattice settings, M_A, M_B and M_C can be differentiated by the number of *(h0l)* and *(hhl)* diffraction peaks observed, as shown in Figure 2.7.

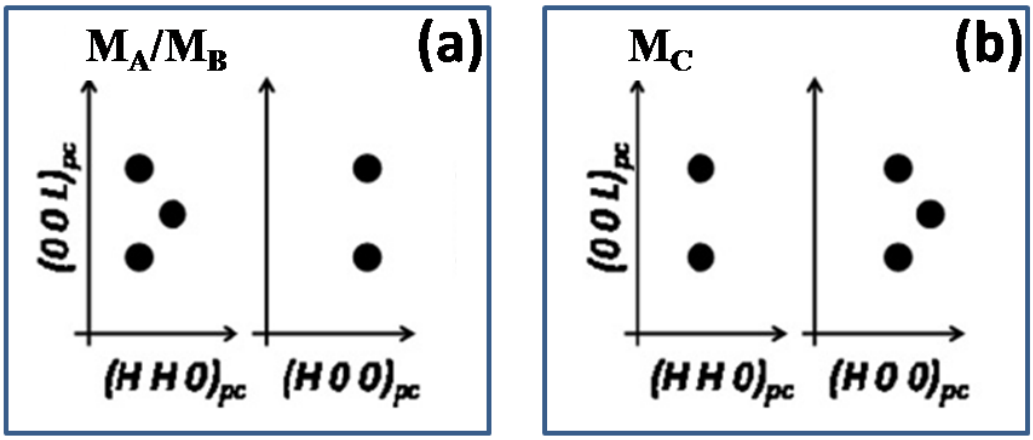

Figure 2.7 Schematic illustration of diffraction patterns in reciprocal space mapping for (a) monoclinic M_A and M_B (b) monoclinic M_C phases

In this project, both lab based X-ray source (Bruker) and Synchrotron light source (Singapore Synchrotron Light Source-SSLS and Shanghai Synchrotron Radiation Facility-SSRF) were employed to study the crystal structures of epitaxial thin films. High resolution XRD improves the resolution by cutting the X-ray beam to obtain a single wavelength X-ray. However, this results in the loss of intensity and flux. Therefore, the lab based X-ray source is not strong enough to achieve precise and clear characterization of the crystal structure, especially for very thin films. Synchrotron light source has a much higher brilliance and brightness, providing a powerful tool for the investigation into crystal structure for epitaxial thin films.

2.3 Transmission Electron Microscopy

A Philips CM300 FEG Transmission Electron Microscopy (TEM) at an acceleration voltage of 300 kV was employed in this project for high resolution images and diffraction patterns analysis of cross-sectional thin film samples. A scanning transmission electron microscopy (STEM) detector on a JEOL JEM-2010F at 200 kV was used to analyze the element distribution in the film by the energy dispersive X-ray spectroscopy (EDX) mapping. More detailed TEM operation and analysis can be found in the references[70, 71].

2.4 Atomic Force Microscopy

Atomic Force Microscopy (AFM) probes the sample surface with a sharp tip attached to a cantilever. By scanning a sharp tip over the sample surface, the high resolution images at atomic scale can be produced from the deflection of the cantilever. AFM can be operated in three modes, namely contact mode, tapping mode and non-contact mode. In the contact mode, the tip contacts with the sample surface, which gives a high scan speed with atomic resolution. The disadvantage of this mode is that the lateral force can distort features in the image and the damage of soft sample due to the scraping between the tip and sample. In the tapping mode, the cantilever is oscillating while the tip lightly taps on the sample surface during scanning and contacting the surface at the bottom of the swing. The tapping mode increases the lateral resolution at the cost of lower scan speed. Non-contact mode operates by holding the tip at a small distance above the sample. During the scan, the tip doesn't contact sample surface, which results in lower lateral resolution and slower scan speed. In this thesis, a Dimension Icon Atomic Force Microscopy with ScanAsyst (Bruker AXS) is employed to study the surface morphology of as-deposited BFO thin films.

2.5 Electrical Characterization

To characterize the electrical properties of thin films in out-of-plane vertical direction, top electrode is required to form a capacitor with bottom conductive buffer layer under the ferroelectric layer. In this project, gold electrode with a diameter of 0.2 mm was sputtered on top of as-deposited BFO thin films through a mask. The area of deposited electrode was calibrated by optical microscopy to avoid the possible shadow effect, which could increase the area of electrode by several times. During the measurement, a bipolar voltage was applied to the sample through top electrodes, as shown in Figure 2.8. The effective equivalent electrical circuit is also shown, in which two capacitors are connected in series.

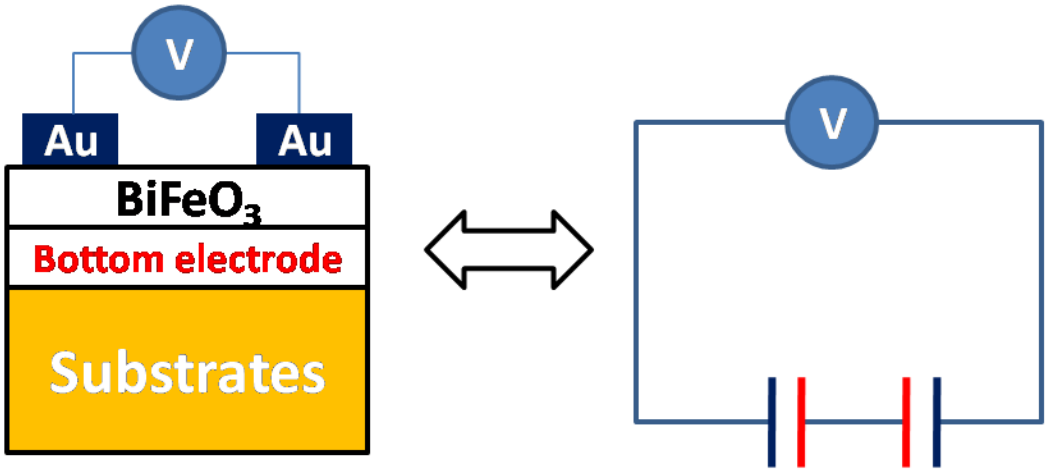

Figure 2.8 Schematic illustration of the measurement setup for out-of-plane polarization and its equivalent electrical circuit.

Dielectric property of BFO thin films was characterized by an Impedance Analyzer (Solartron 1261, Farnborough, UK). The real and imaginary permittivities were measured over a wide frequency range from 10^{-1} Hz to 10^{6} Hz.

Ferroelectric polarization versus electric field (P-E) hysteresis loop was measured by a Radiant precise workstation (Radiant Technologies, Medina, US). The measurement of the hysteresis loops are based on the Sawyer Tower circuit [72], shown in Figure 2.9. Here the electrical voltage across the sample is applied through the signal generator, and the current is integrated into charge by of a large reference capacitor in series with the sample. To generate the P-E loops, the voltage applied to the material on the x-axis of the oscilloscope and the surface charges on the y-axis are plotted.

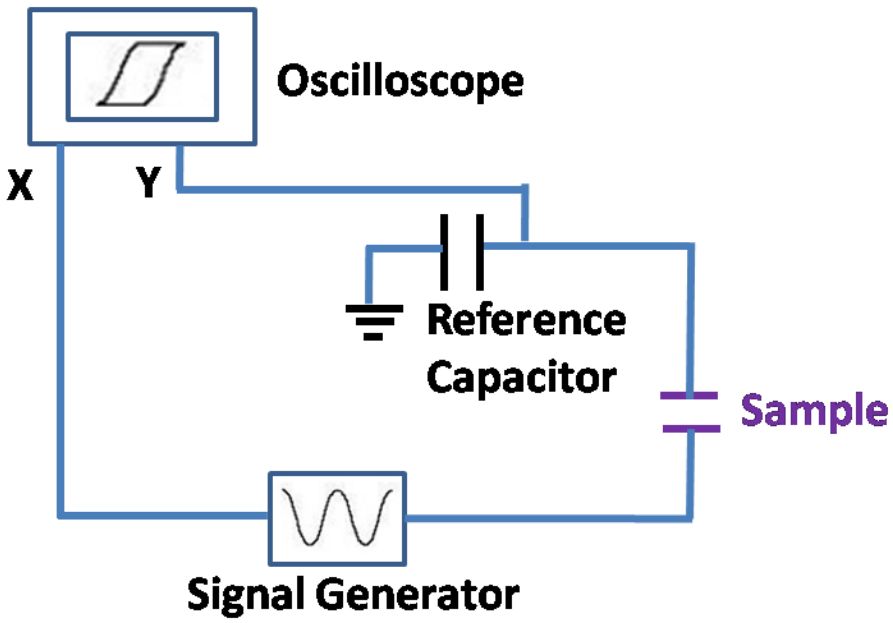

Figure 2.9 Sawyer Tower circuit for the measurement of ferroelectric hysteresis loop

During the measurement of P-E loops, there are several artifacts that have to be avoided to obtain reliable data [73]. As shown in Figure 2.10 (a), the dead short circuit gives rise to a round circle loop. A linear lossy capacitance, which is a combination of ideal capacitance and resistor, produces the loop in Figure 2.10 (b). Another artifact may arise from the saturation of amplifier. As shown in Figure 2.10 (c), the saturated hysteresis loops generate a larger remanent polarization as the applied voltage increases. This is not possible as if the dipole of the ferroelectric sample is saturated at lower voltage, there is no addition dipole moment in the system to increase the polarization at higher voltage. What happened here is the saturation of the amplifier in the measuring system. The last artifact is from the nonlinear lossy capacitor as shown in Figure 2.10 (d). This can be tested by the frequency dependent measurement of P-E loops, as the dielectric loss is highly frequency dependent while the intrinsic ferroelectric property is frequency independent.

Leakage behaviour is characterized by a Keithley meter (Keithley 6430, Cleveland, US). The current-voltage curve is measured by applying a DC voltage through the electrodes and collecting the current through the circuit by an Ampere meter. Temperature dependent I-V curves can be measured to obtain the information of conduction mechanisms by fitting into different conduction models [6].

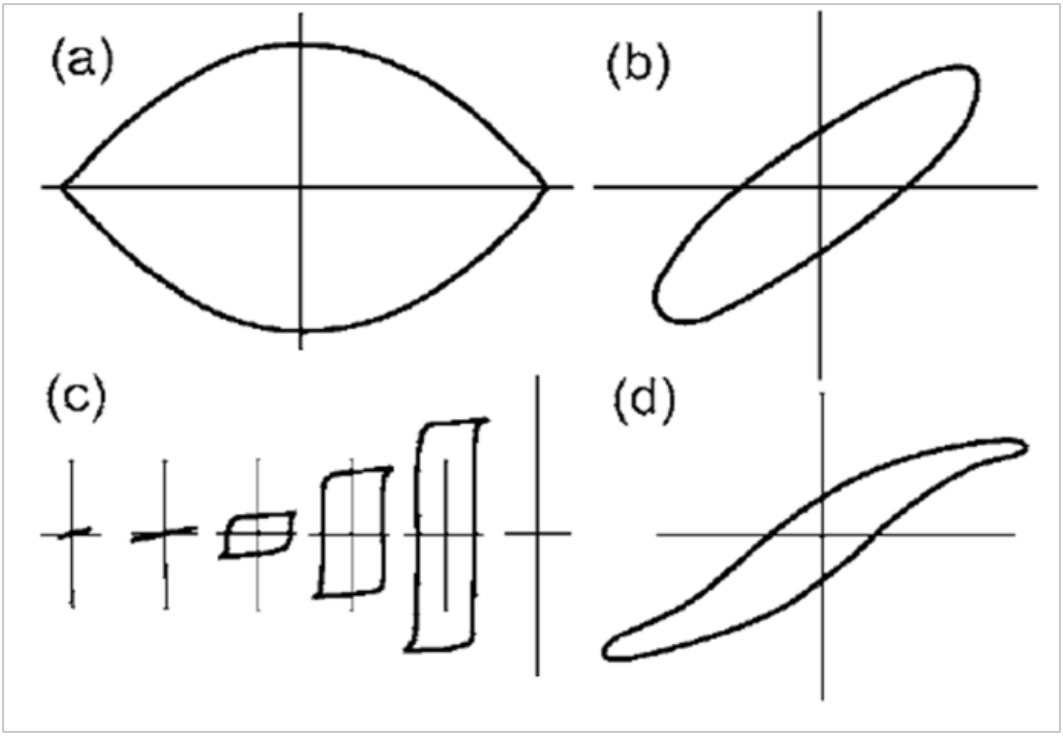

Figure 2.10 Schematic illustration of possible artificial data in ferroelectric hysteresis loop measurement. (a) dead shorts, (b) linear lossy dielectric, (c) saturated amplifier, and (d) nonlinear lossy dielectric. Figure adopted from [73].

Chapter 3. EVOLUTION OF MONOCLINIC STRUCTURE AND FERROELECTRIC BEHAVIOUR OF EPITAXIAL $BiFeO_3$ THIN FILMS

3.1 Introduction

The most studied epitaxial BFO thin films so far are those grown on STO (001) single crystal substrates, because of the close match of in-plane lattice dimension between BFO and STO. Also, the large ferroelectric polarization is first reported for BFO films grown on SRO-buffered STO substrates [27]. However, there are still several controversies about the crystal structures of BFO thin films on STO substrates. For example, a fully relaxed and bulk-like rhombohedral structure was reported by Qi et al, for the $BiFeO_3$ thin film of 200 nm in thickness grown by liquid-phase epitaxy [66]. Xu et al., on the other hand, has observed that a monoclinic structure exists in the film grown by pulsed laser deposition [51]. Saito et al. observed a tetragonal structure for the film thickness below 50nm but a monoclinic structure for the film thickness above 50 nm [10].

In addition, another interesting problem for BFO film is the epitaxial strain effect on ferroelectric behaviour. As is well known, strain relaxes as the film thickness increases. Therefore, the thickness dependent ferroelectric properties would be an ideal platform for the study of the strain effect. There have been some reports about the strain effect on the polarization of BFO epitaxial thin films deposited on STO (001) substrates. Kim et al. reported that the polarization almost keep unchanged when strain relaxes with increasing film thickness of (001) BFO films grown on $SrTiO_3$ (STO) substrate [62]. However, more recently, Jang et al. reported that there was a strong strain dependence of polarization in BFO (001) thin films due to the polarization rotation. Therefore, the strain effect on polarization in BFO epitaxial thin films is not fully understood.

The objective of study in this chapter is to identify the crystal symmetry and lattice parameters of BFO thin films deposited on STO (001) substrates by high resolution synchrotron X-ray diffraction. In addition, a thorough understanding is made on how the crystal structure relaxes as the film thickness increases and how this structural change affects the ferroelectric and leakage behaviour.

3.2 Twinning Rotation of $BiFeO_3$ (001) Thin Films

The BFO thin film of 720 nm in thickness was grown by radio frequency sputtering at the deposition temperature of 680 $^{\circ}$C, from a ceramic target with 10% bismuth excess to compensate for Bi loss at high temperature. Prior to the deposition of the BFO thin film, a buffer layer of SRO of ~60 nm in thickness was first deposited on STO (001) substrate as the bottom electrode. The as-grown BFO thin film was investigated by high-resolution synchrotron X-ray diffraction at Singapore Synchrotron Light Source (SSLS). The ferroelectric and leakage behaviour of the thin film were investigated by using the radiant precise workstation (Radiant Technologies) and Keithley 6430 I-V system, respectively. Circular Au electrodes of diameter 0.2 mm were sputtered on the film surface prior to evaluation of these electrical behaviour.

Figure 3.1(a) shows the reciprocal space mapping (RSM) around (002) STO diffraction of the epitaxial BFO/SRO/STO thin film at $\Phi = 0^{\circ}$. The vertical axis is the scan along the 2θ direction with zero point at the peak of substrate (2θ-θ coupled scans). Meanwhile, the horizontal axis along ω measures the relative angles between atomic planes of the film and substrate. A strong reflection was observed at the top of the figure, which was identified as (002) diffraction of the STO substrate. SRO gave rise to the second spot which had the same ω value as the STO substrate, showing that the

SRO buffer layer was grown coherently. The two spots with the same 2θ value but different ω values came from the BFO film. The centers of the two peaks from BFO were not at the origin, indicating that the (002) atomic plane of BFO film was not completely parallel to the substrate. As is shown in Figure 3.1 (c), the diffraction of the BFO film was from two sets of atomic planes, with normal directions at the angle of 0.900^{o} to each other as calculated from Gaussian fitting results.

In contrast to $\Phi = 0^{\circ}$, at the direction of $\Phi = 45^{\circ}$ (Figure 3.1(b)), BFO (002) showed three peaks with the middle one having the strongest intensity. The peaks from the STO substrate and SRO buffer layer were the same as $\Phi = 0^{\circ}$. This indicates that there were three sets of atomic (002) planes from BFO at the direction of $\Phi = 45^{\circ}$. The middle plane was parallel to the substrate as it followed the STO and SRO in ω direction. The left and right planes tilted along $\Phi = 45^{\circ}$ direction, with their normal directions at an angle of 1.320°. These three planes are schematically shown in Figure 3.1 (d).

Four structural variants exist in the rhombohedral phase, r_1, r_2, r_3 and r_4 with their polarization directions along <111> direction of the parent cubic structure. [12] Based on the results from the (002) RSM and analyses above, the structure of rhombohedral twins is proposed as in Figure 3.1 (e). At $\Phi = 0^{\circ}$, r_1 and r_4 overlapped and r_2 and r_3

also superposed, resulting in two sets of atomic planes. This explains why two peaks were observed at $\Phi = 0^{\circ}$ direction, with r_1 and r_4 constituted the left plane and r_2 and r_3 formed the right plane. While at $\Phi = 45^{\circ}$, r_2 and r_4 tilted in the plane that was perpendicular to the scanning direction and the tilted angle was very small. Therefore, at $\Phi = 45^{\circ}$, r_2 and r_4 overlapped and appeared to be parallel with the substrate (002) plane. The other two peaks arose from tilted r_1 and r_3. Thus, r_1 and r_2 (or r_3 and r_4) twins rotated 0.900° while r_1 and r_3 twins rotated 1.320° to form a closely packed structure. Under the compressive epitaxial stress from the STO substrate, the rotation of these twinning blocks is favorable as it would partially release stresses in BFO thin film.

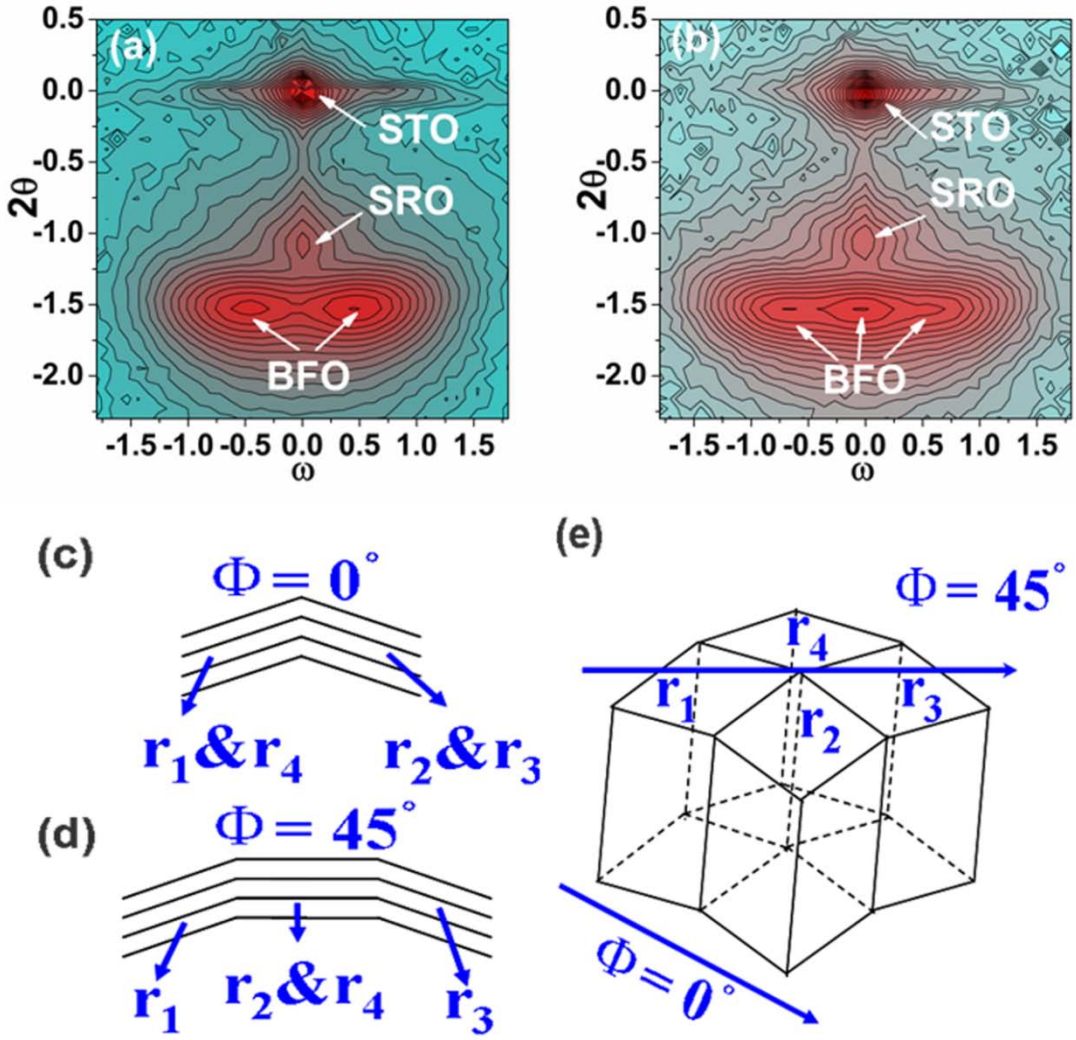

Figure 3.1 Reciprocal space mapping around (002) STO at (a) $\Phi = 0^{\circ}$, (b) $\Phi = 45^{\circ}$ for the epitaxial BFO film of 720 nm in thickness. The twinning blocks r_1 to r_4, shown in real space, corresponding to $\Phi = 0^{\circ}$ and $\Phi = 45^{\circ}$ are schematically shown in (c) and (d), respectively. (e) shows the three dimension twinning blocks.

The mappings around (002) only provide the information on the spacing of lattice planes in the out-of-plane direction. To precisely determine the crystal structure and the lattice parameters of the epitaxial BFO thin film, RSM diffraction patterns around (103) STO at $\Phi = 0^{\circ}$ and (113) STO at $\Phi = 45^{\circ}$ were measured, as shown in Figure 3.2

(a) and 2(b), respectively. Two diffraction spots from BFO film were clearly seen in (103) while three diffractions spots in the (113) pattern. This confirms that the BFO film exhibits a monoclinic structure. However, the lattice is rotated by 45° about the surface normal direction (*c* direction) with respect to the STO substrate, with the *a* and *b* axes being about the $\sqrt{2}$-times of the substrate. Thus, the BFO patterns in Figure 3.2 (a) and (b) are indexed as $(113)_m$ and $(203)_m$ of monoclinic system.

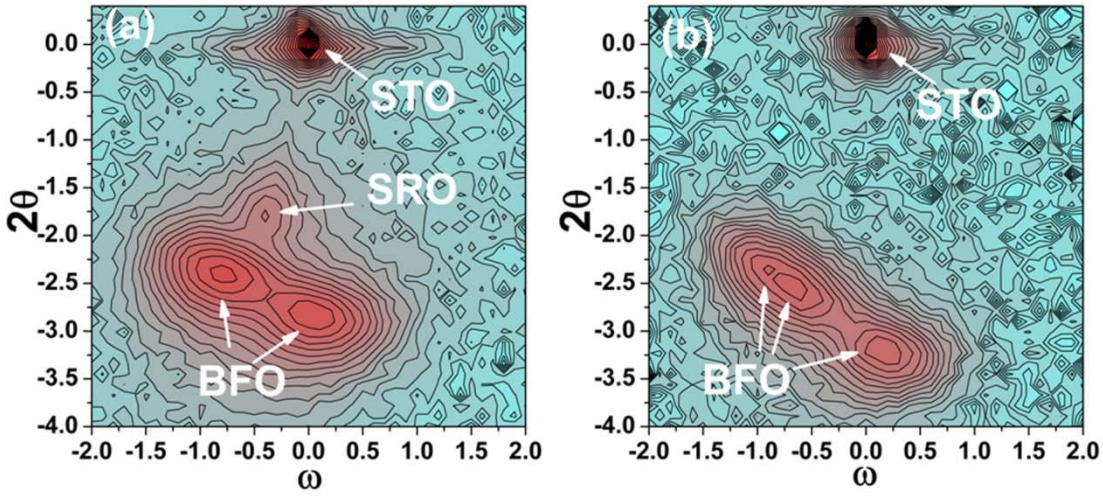

Figure 3.2 Reciprocal space mappings around (a) (103), and (b) (113) $SrTiO_3$ for the epitaxial BFO film of 720 nm in thickness.

The lattice parameters of the BFO monoclinic unit cell were determined to be *a* = 5.610(1) Å, *b* = 5.529(1) Å, *c* = 4.031(1) Å and β = 89.34(1)°. They are comparable to the lattice constants reported in previous studies except that the out-of-plane lattice

parameter *c* is much larger, as is shown in Table 3. The BFO film lattice is thus not fully relaxed to the bulk unit cell at the film thickness of 720 nm, although the compressive stress arising from the substrate mismatch may be released partially as a result of the rotation in twinning structure of BFO film. The cross-section view of the twinning structure is schematically shown in Figure 3.3. As can be seen, the vertical domain walls are formed as a result of twinning rotation.

Table 3 Structure and lattice parameters of the epitaxial BFO thin film of 720 nm in thickness as compared to those of the films of different film thicknesses

Film Thickness (nm)	Lattice parameters	Length of body diagonal $[111]_p$
~720, this work	**Monoclinic** ***a* = 5.610 Å, *b* = 5.529 Å,** ***c* = 4.031 Å, *β*= 89.34°**	**6.875 Å**
~200, [66]	Rhombohedral a = 3.9618 Å, α = 89.45°	6.862 Å
~200, [51]	Monoclinic $a/\sqrt{2}$ = 3.907 Å, $b/\sqrt{2}$ = 3.973 Å, c = 3.997 Å, β= 89.2°	6.857 Å
~500, [10]	Monoclinic a = 5.602 Å, b = 5.562 Å, c = 3.971 Å, β= 88.89°	6.845 Å

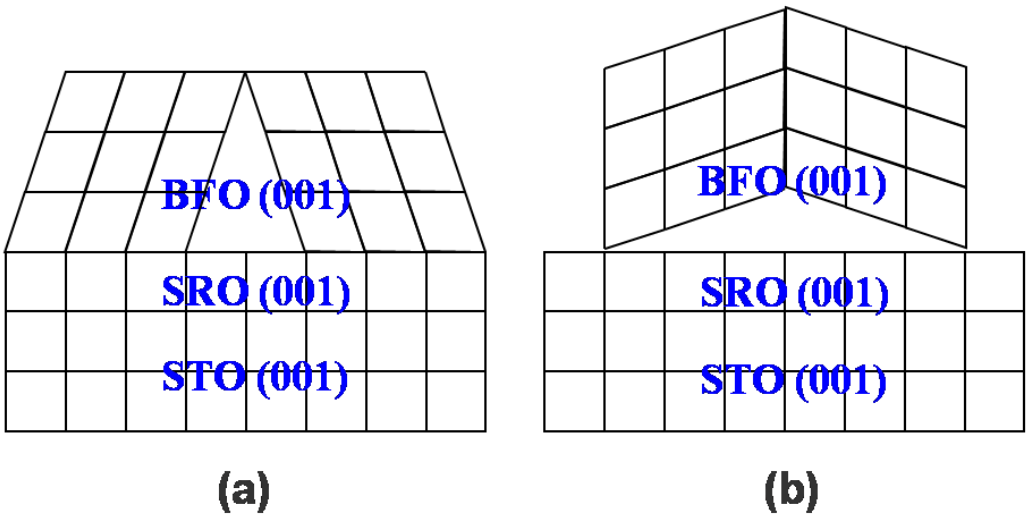

Figure 3.3 Schematic diagram of the twinning structure for the epitaxial BFO thin film deposited on STO (001) substrate with SRO buffer layer, without (a) and with (b) rotation of rhombohedral blocks. The arrows show the direction of polarization in $[111]_p$ in the pseudocubic unit cell.

This twinning structure confirmed for the BFO thin film gives rise to an enhancement in ferroelectric behaviour. As shown in Figure 3.4 (a), the epitaxial BFO thin film exhibited well established square-like hysteresis loops, which were almost independent of test frequency. The remanent polarization value was measured to be $2P_r$ = 164 ± 2 μC/cm^2 with a coercive electric field $2E_c$ = 510 ± 5 kV/cm. The observed P_r value is larger than those previously reported, in the range of 50-60 μC/cm^2. Two considerations are made to account for the enhancement in polarization. Firstly, from the lattice parameters determined by RSM, the length of $[111]_p$ in the pseudocubic unit cell can be calculated. The results, as summarized in Table 3, show that the length of polarization direction is enlarged, meaning that the polarization along $[111]_p$ direction

is enhanced. Secondly, as the rhombohedral variants are rotated (Figure 3.3(b)), the polarization projection onto [001] direction is enlarged as compared to that of the structure which is not rotated (Figure 3.3 (a)). The *P-E* loops were measured along the [001] direction, so the rotated twinning structure leads to an enhanced remanent polarization, by an elongated polarization in $[111]_p$ direction and increased projection onto the [001] direction.

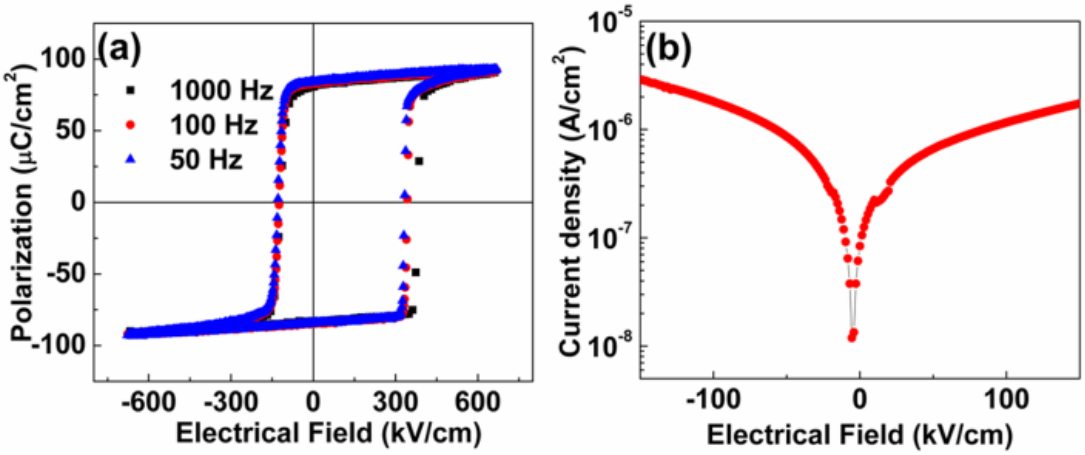

Figure 3.4 (a) Frequency dependent hysteresis loops for the epitaxial BFO thin film of 720 nm in thickness. (b) *J-E* relationships of the Au/BFO/SRO capacitor for both negative and positive biases.

Figure 3.4 (b) shows the leakage current density of the epitaxial BFO thin film as a function of applied electrical field for both negative and positive biases. A very low leakage current density of ~1.2 ±0.3 × 10^{-6} A/cm^2 at 100 kV/cm was obtained, which was three orders of magnitude lower than some of those previously reported. The

origin of the greatly reduced leakage current density for the epitaxial BFO thin film with rotated twining structure is associated with the interface between the BFO and SRO layers, where the mismatch strain is largely accommodated. Indeed, as suggested recently, the leakage mechanism of BFO is interface-limited, rather than bulk-limited [74].

3.3 Evolution of Thickness-dependent Structure and Ferroelectric Behaviour of $BiFeO_3$ (001) Thin Films

In order to investigate the effect of residual strain on twinning evolution and ferroelectric behaviour, epitaxial BFO (001) films with thickness from 30 nm to 720 nm were grown by radio frequency sputtering. The crystal structure was identified by high resolution synchrotron X-ray diffractometry at the X-ray Development and Demonstration (XDD) beam line of Singapore Synchrotron Light Source (SSLS) and BL14B1 beam line of Shanghai Synchrotron Radiation Facility (SSRF), using 1.000 Å X-rays with a Huber 5021 6-axes diffractometer. The ferroelectric and leakage behaviour of the thin film were investigated by using the radiant precise workstation (Radiant Technologies) and Keithley 6430 I-V system, respectively.

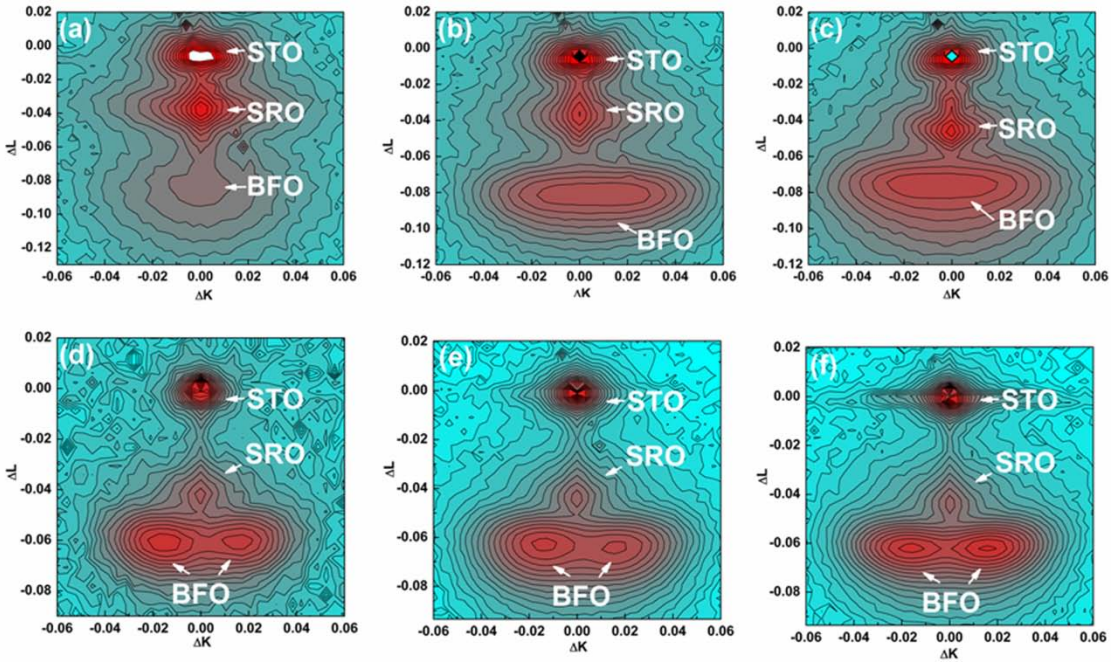

Figure 3.5 *KL* reciprocal space mappings around STO *(002)* for the epitaxial BFO films with film thickness of 30 nm (a), 180 nm (b), 360 nm (c), 450 nm (d), 540 nm (e) and 720 nm (f), respectively.

Figure 3.5 shows the *KL* reciprocal space mappings (RSM) from (002) STO diffraction of the epitaxial BFO thin films. The vertical axis is along the *L* direction while the horizontal axis is along *K* direction in the reciprocal space. The spots from STO and SRO remain to be a single peak for all mappings with different film thicknesses, showing a high quality of epitaxial growth of the SRO buffer layer. However, for the diffraction peaks from BFO, it develops from a single sharp peak at 30 nm to an elongated peak at 180 nm and 360 nm and finally to two well separated peaks for 450 nm, 540 nm and 720 nm films. As discussed in the previous section, these two peaks with the same *L* value indicate a rotated twinning structure in BFO lattice. Therefore,

with increasing film thickness, the BFO film changes from a strained lattice to a partially relaxed one with monoclinic rotated twinning structure.

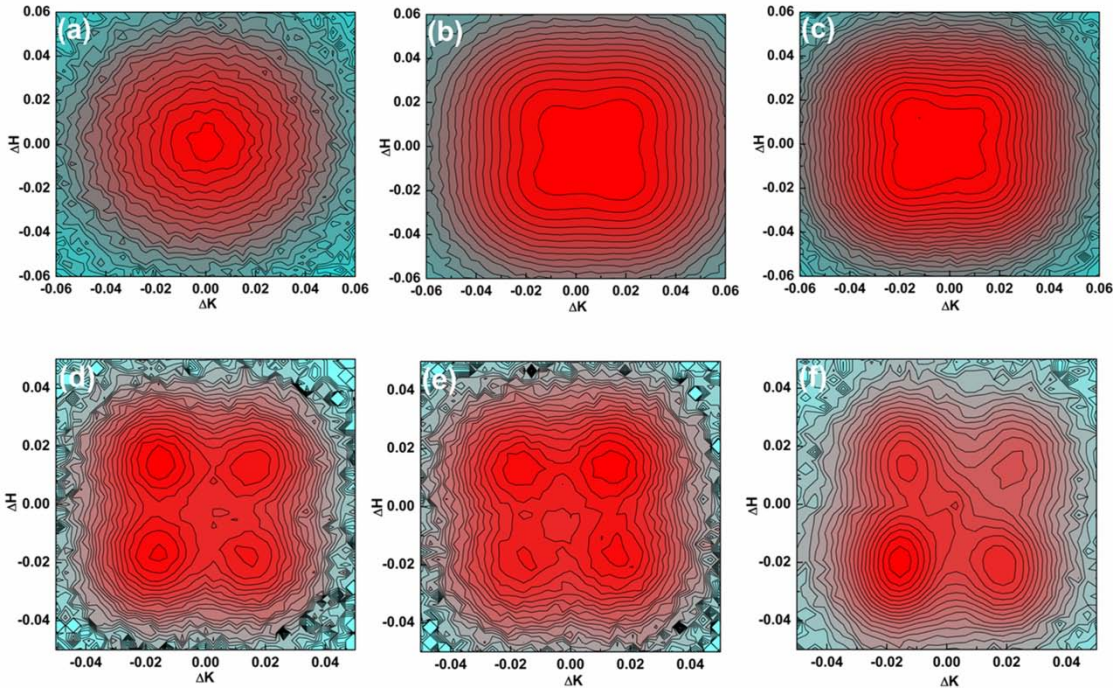

Figure 3.6 *KH* reciprocal space mappings around STO *(002)* for epitaxial BFO films with film thickness of 30 nm (a), 180 nm (b), 360 nm (c), 450 nm (d), 540 nm (e) and 720 nm (f), respectively. *L* values were set at the corresponding BFO peaks in Figure 3.5.

In order to fully understand the crystal structure of the BFO films of varying thicknesses, *KH* reciprocal space mappings (RSM) around (002) STO diffraction were measured for BFO thin films with thickness changing from 30 nm to 720 nm, as shown in Figure 3.6. These mappings were obtained with *L* value at the BFO peaks in Figure 3.5. Clearly, for the film of 30 nm in thickness, a single peak without any distortion was observed. As the film thickness increases, the BFO spot shows a trend to form

four peaks for diffraction in the *KH* plane. This confirms the structure model proposed in Figure 3.1 (e), in which two pairs of twin variants along [100] and [010] coexist.

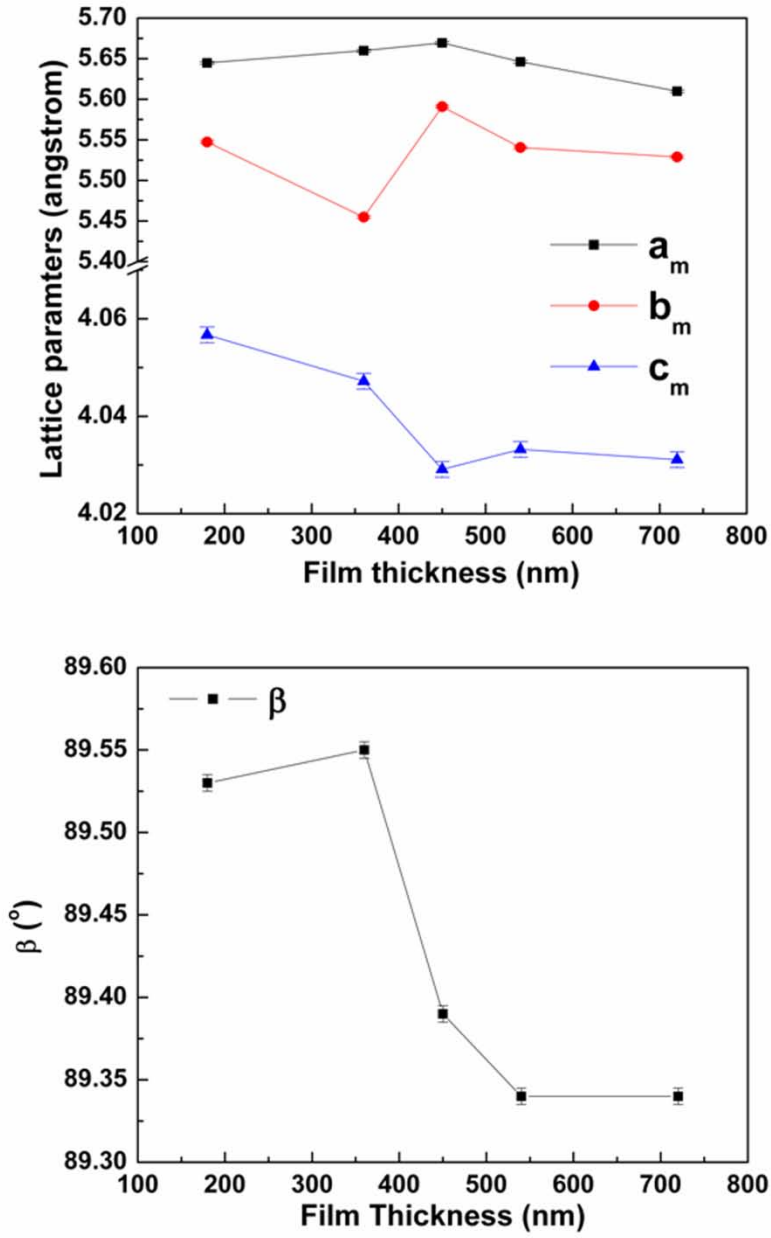

Figure 3.7 Lattice parameters derived from reciprocal space mappings for the epitaxial BFO film with the film thickness changing from 180 nm to 720 nm.

From the reciprocal space mappings shown above and the mappings around (103) and (113) (not shown here), the crystal structures and lattice parameters were determined, as summarized in Figure 3.7. The BFO film possesses a fully strained tetragonal structure for the film with thickness of 30 nm. However, the films with thickness increasing from 180 nm to 720 nm show a monoclinic twinning structure, which is initiated at 180 nm and fully developed at 450 nm. The monoclinic distortion angle β shows increasing deviation from 90° as film thickness increases. The lattice parameters exhibits a different evolution as compared to the film with in-plane twins but without out-of-plane twinning rotation [75]. This unique out-of-plane twinning rotation relaxes strain in the films and maintains a degree of distortion in lattice parameters even at a film thickness of 720 nm.

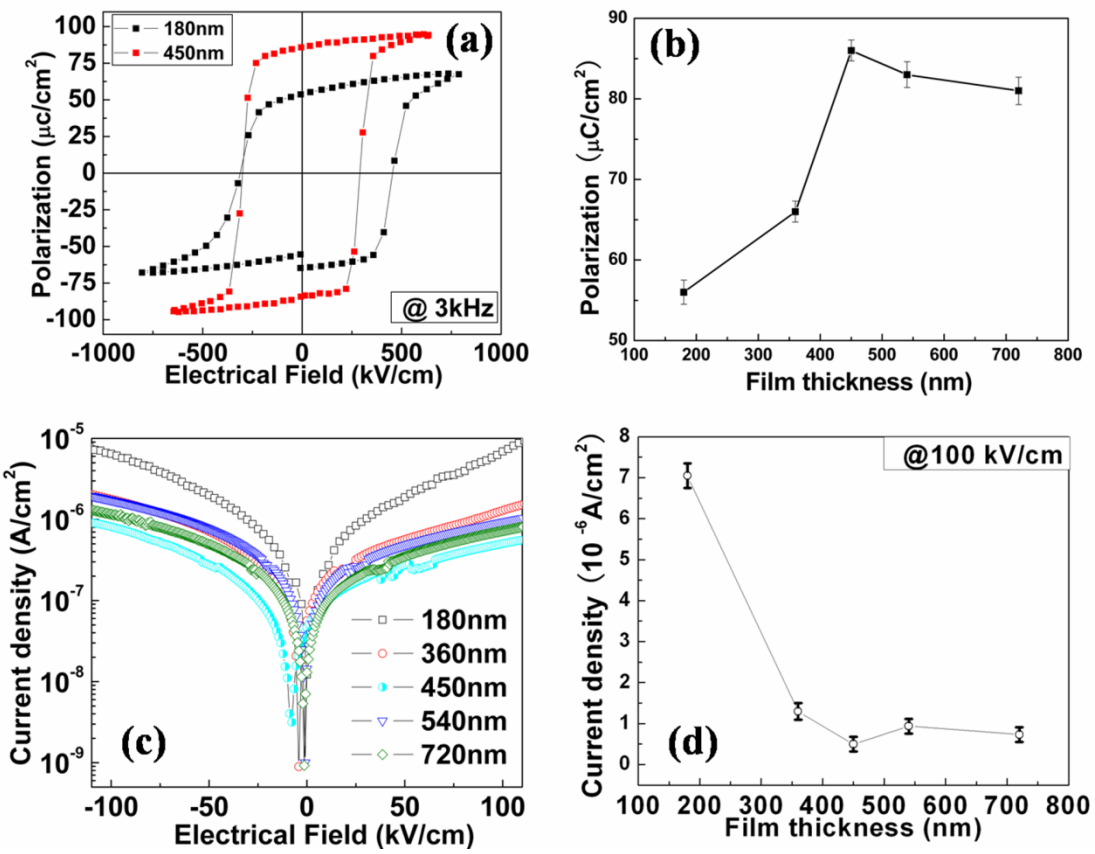

Figure 3.8 (a) Hysteresis loops for epitaxial BFO thin films of 180 nm and 450 nm in thickness; (b) remanent polarization as a function of film thickness; (c) *J-E* relationships of the Au/BFO/SRO capacitor for the epitaxial BFO film with film thickness increasing from 180 nm to 720 nm; (d) leakage current density at 100 *kV/cm* as a function of film thickness from 180 nm to 720 nm.

Figure 3.8 (a) shows the hysteresis loops for the 180 nm and 450 nm BFO thin films at the test frequency of 3 kHz. Both loops are square-like, showing the intrinsic remanent polarizations of epitaxial ferroelectric thin films. Due to the large leakage current, the polarization of 30 nm film cannot be properly measured. The polarization as a function of BFO film thickness increasing from 180 to 720 nm is plotted in Figure 3.8 (b). The remanent polarization increases from 55 to 87 μC/cm^2 when the film thickness

increases from 180 nm to 450 nm, representing about 58% enhancement. As reported in a previous study [62], for epitaxial BFO (001) films without twinning rotation structure, the polarization is almost unchanged as the film thickness increases from 77 nm to 960 nm. This great enhancement of polarization observed in the present work is thus related to the unique strain relaxation mechanism by twinning rotation. Figure 3.8 (c) shows the leakage current density of the epitaxial BFO (001) film as a function of applied electrical field for film thickness changing from 180 nm to 720 nm. The leakage current density measured at 100 kV/cm is plotted as a function of film thickness in Figure 3.8 (d). Despite that the 180 nm film has a larger leakage current than others; all the samples show very low leakage current in the order of 10^{-6} A/cm^2. This agrees with the square-like loops obtained in ferroelectric hysteresis test and confirms the intrinsic polarization measured.

The monoclinic lattice of BFO is orientated by 45° with respect to [001] direction of the substrate. A schematic configuration of monoclinic unit cell is represented by the thick lines in Figure 3.9 (a), while the pseudocubic (*pc*) unit cell is shown by the dashed lines. In order to derive the in-plane strain, the lattice parameters of monoclinic unit cell have to be transformed into the pseudocubic cell. This relation is given by

$$a_{film} = \frac{a_m + b_m}{2\sqrt{2}} . \quad (3.1)$$

$$c_{film} = c_m / \sin\beta . \quad (3.2)$$

where a_{film} and c_{film} are the lattice constants for the pseudocubic cell. As the thin SRO buffer layer and STO substrate are rather close in lattice parameters, as compared to that between BFO and STO, the mismatch strain is largely arising from the lattice mismatch between the BFO film and STO substrate. Taking the bulk BFO rhombohedral phase as a reference, the in-plane and out-of-plane strain are calculated by the following relationship:

$$\varepsilon_{in-plane} = \varepsilon_{xx} = \varepsilon_{yy} = \frac{a_{film} - a_{bulk}}{a_{bulk}} . \quad (3.3)$$

$$\varepsilon_{out-of-plane} = \varepsilon_{zz} = \frac{c_{film} - c_{bulk}}{c_{bulk}} . \quad (3.4)$$

The strains thus derived are plotted as a function of film thickness in Figure 3.9 (b). The in-plane strain does not relax from negative to zero with increasing thickness as expected, but varies slightly from -0.5% to +0.5%. This unique behaviour of strain evolution is due to the twinning rotation. At the film thickness of 180 nm, when the twinning is initiated, the compressive strain is relaxed to nearly zero. While, the fully developed twinning rotation structure even drives the compressive strain from the substrate to be tensile at 450 nm. For the out-of-plane strain, it keeps decreasing as the film becoming thicker, except a drop at 450 nm when the twinning rotation is fully formed. The trend of strain change does not agree with the change of polarization in Figure 3.8 (b), showing no direct correlation between the residual strain and

polarization.

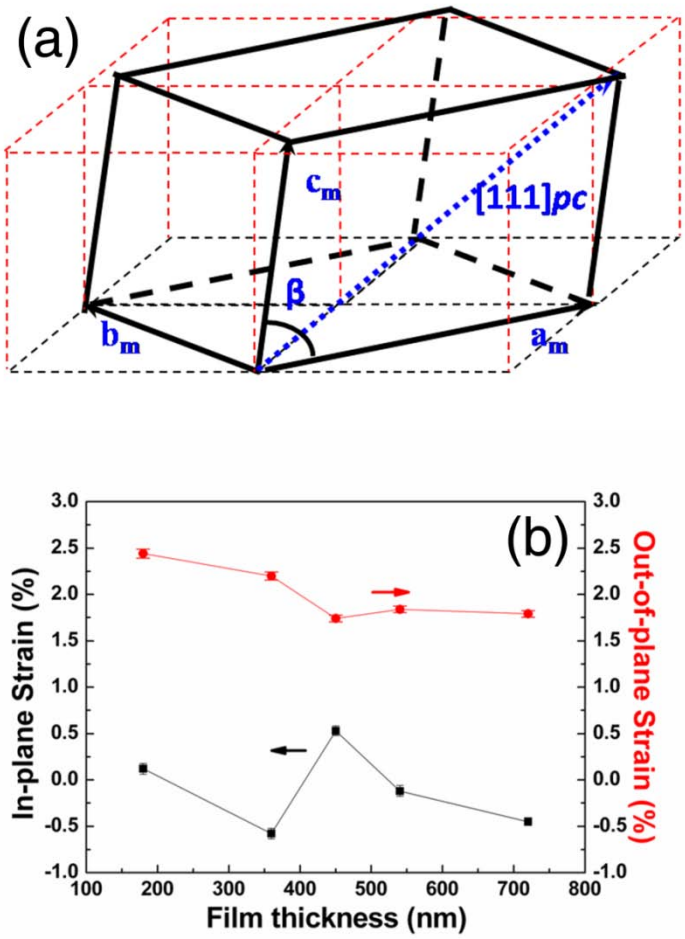

Figure 3.9 A schematic drawing for the relationship between monoclinic BFO unit cell (thick lines) and pseudocubic BFO unit cell (dashed lines); (b) in-plane strain and out-of plane strain as a function of film thickness.

This agrees with the result of the first principles calculations [48] and previous experimental results [62] that the polarization of BFO is not strongly dependent on the strain. In addition, the polarization rotation mechanism proposed in [40] also cannot

explain the polarization change of about 58% observed in our films. For the 450-nm-thick BFO film with a tensile in-plane strain, the polarization is expected to rotate towards $[110]_{pc}$ and give rise to lower polarization along the measured [001] direction. However, the polarization measured at 450 nm is even higher than those with compressive in-plane strain.

If the strain is not the critical parameter to account for the large polarization variance with film thickness, then now we have to turn to the length of polarization direction along the body diagonal of pseudocuic lattice. As is shown by the dashed arrow $[111]_{pc}$ in Figure 3.9 (a), the body diagonal direction is the face diagonal of (101) in monoclinic cell. The calculated length along $[111]_{pc}$ and polarization are plotted in Figure 3.10 as a function of film thickness. A strong and clear dependence of polarization on the $[111]_{pc}$ length is obviously seen. For the ferroelectric film of tetragonal phase, the in-plane strain is very important as it affects the length of polarization direction in [001]. Indeed, the first principles study shows ferroelectric films with tetragonal phase ($BaTiO_3$, $PbTiO_3$ and $BiFeO_3$ (P4mm)) are in-plane strain sensitive[48] . However, for the monoclinic phase, the in-plane strain is not the critical influencing factor, because the polarization direction is not along [001] any more. Although the monoclinic phase of our BFO films shows a degree of distortion from the bulk rhombohedral phase, the polarization direction should still be along the body

diagonal direction in pseudocubic unit cell. Therefore, the body diagonal length is the determining factor, as it affects the space for the ionic displacement within the unit cell. According to the modern Berry-phase theory of polarization [76, 77], the dipole moment from displacement of ions is the major contribution to the ferroelectric polarization although delocalized electrons also add to the total polarization. The dependence of polarization on the distortion along the polarization direction observed in the present work provides the experimental evidence for this theoretical understanding.

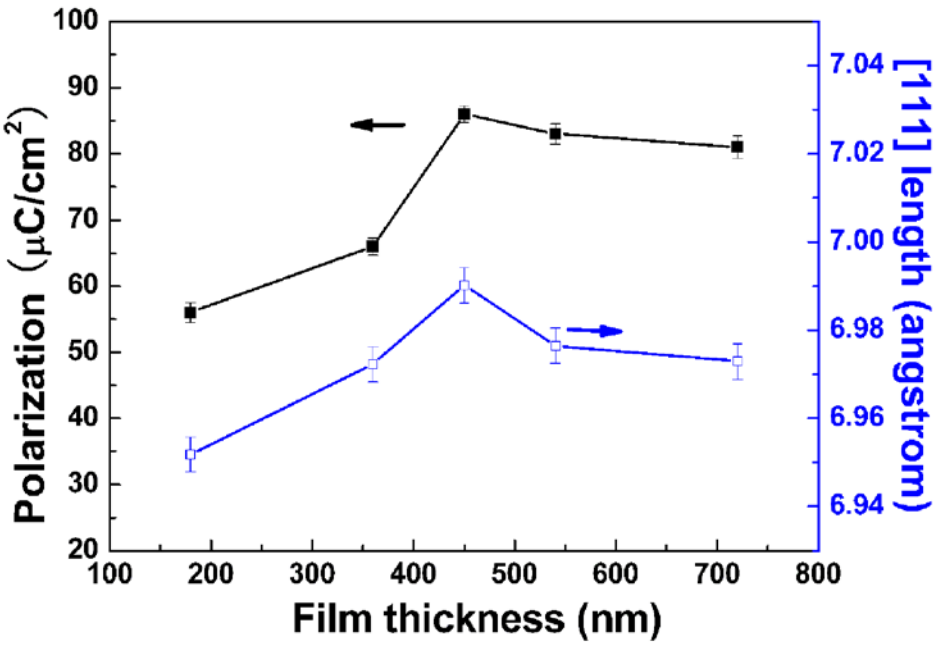

Figure 3.10 Remanent polarization and $[111]_{pc}$ length as a function of film thickness.

3.4 Summary

In summary, the crystal structure of BFO thin film with the thickness ranging from 30 nm to 720 nm was characterized by high-resolution synchrotron X-ray diffraction. For BFO film of 30 nm in thickness deposited on SRO-buffered STO (001) substrate, the crystal structure is the fully strained tetragonal phase with a small $c/a \sim 1.05$. For BFO films of 180 nm to 720 nm in thickness, a unique twinning rotation structure was identified, which shows a monoclinic symmetry. This structure result agrees with the conclusion that BFO with film thickness less than 50 nm shows a tetragonal structure while the thickness above 50 nm shows a monoclinic structure [10]. This twinning rotation identified here reveals a new mechanism to relax strain as film thickness increases. The vertical domain walls, as a result of this twinning rotation, provide a new path to engineer the domain wall configuration and therefore the ferroelastic and ferroelectric hehaviour.

For the strain effect on ferroelectric polarization, our results in this chapter show that remanent polarization increases as the film thickness increases to 450 nm and then decreases from 450 nm to 720 nm. This is inconsistent with the unchanged polarization as BFO film thickness varies reported in a previous study [62], which may result from the unique twinning rotation structure observed in our films. In addition, the

polarization doesn't show a strong dependence on strain, as reported in another previous study [40]. Instead, polarization has a strong dependence on the body diagonal length of distorted pseudocubic unit cell. Our results indicate that the distortion in polarization direction along body diagonal in pseudocubic unit cell is the critical factor that determines the remanent polarization of monoclinic phase BFO thin films. This observation supports the theoretical understanding that ionic displacement is the major contribution to the ferroelectric polarization.

Chapter 4. $BiFeO_3$ FILMS OF SUPER-TETRAGONAL PHASE WITH A GIANT *c/a* RATIO ON $SrTiO_3$ SUBSTRATES

4.1 Introduction

In 2009, the discovery of a new tetragonal-like BFO M_C phase with a giant *c/a* ~ 1.25 for epitaxial thin films on LAO (001) substrate reignites the interest in BFO [52, 64]. This tetragonal-like BFO phase is of particular curiosity as it shows an enhanced electromechanical response at MPB with a rhombohedral-like BFO M_A phase [52]. Also, it was predicted to have a giant polarization ~ 150 μC/cm^2 [54]. From the results of theoretical calculations, this tetragonal-like phase was identified as a stable phase only under high compressive strain of above ~ 4.5%. However, the super-tetragonal phase with a giant *c/a* ~ 1.25 was first reported to occur in a pure BFO film deposited at high growth rate on STO substrates [63]. The misfit compressive strain of 1.5% from STO substrate is not possible to provide enough high compressive strain to trigger a stable super-tetragonal phase, according to the first principles results.

The objective of this chapter is to investigate the film growth condition for developing

BFO super-tetragonal phase on STO (001) substrates. In addition, a detailed systematic structure study will be performed to identify the different phases for BFO films grown at different growth rates. What is more important is to explore the origin of forming BFO super-tetragonal phase on STO substrate, which cannot be understood from the strain phase diagram by theoretical calculations.

In the following sections of this chapter, growth rate induced phase transitions will first be shown for BFO thin films, which is studied by high resolution XRD. Then, to understand why the super-tetragonal phase BFO can be stabilized on STO substrates, AFM and TEM will be employed to perform a detailed structure characterization. Finally, a structure model will be proposed to clarify the origin of super-tetragonal phase BFO on STO (001) substrates.

4.2 Growth Rate Induced Monoclinic to Tetragonal Phase Transitions of $BiFeO_3$ Thin Films on $SrTiO_3$ (001) Substrates

Epitaxial BFO thin films were grown by radio frequency (RF) sputtering at the deposition temperature of 680 $^{\circ}$C, from a ceramic target with 10% bismuth excess. The deposition rate of BFO films was varied by changing the sputtering power from 30 to 180W, which was in the range from ~7.5 Å/min to ~45 Å/min. The thickness of BFO film is kept constant at ~180 nm. SRO epitaxial layer with 60 nm in thickness was

used as the bottom electrode. Crystal structure was investigated by using the high resolution X-ray diffraction reciprocal space mappings (RSM) at Singapore Synchrotron Light Source (SSLS) and Shanghai Synchrotron Radiation Facility (SSRF) (λ= 1.5405 Å and 1.0000 Å respectively). The RSMs are plotted in reciprocal lattice units (r.l.u.) of the STO substrate (1 r.l.u.=$2\pi/3.905$ Å^{-1}).

Figure 4.1 shows the $(-1-13)_{pc}$ *HL* plane and *HK* plane RSM of BFO films grown at the sputtering power of 30 W (a ,b), 60 W (c, d), 90 W (e, f) and 120 W (g, h). In the *HL* mappings, the vertical axis is along the $[00L]_{pc}$ direction in the reciprocal space of pseudocubic (*pc*) unit cell, while the horizontal axis is along $[HH0]_{pc}$ direction. The peaks with high intensity at about L = 3 come from the STO substrates. The BFO films give rise to the two splitting peaks, which are separated wider as the growth rate increases. The peaks of BFO films are split along the horizontal H direction, which differs from the previous report of vertical splitting two peaks in M_C phase and three peaks in M_A phase [51]. In order to understand this special configuration of diffraction peaks from BFO film, the *HK* mappings were measured at the corresponding L = BFO peaks in HL mappings. The *HK* mappings shows an evolution of BFO peaks from a single peak with small distortion at 30 W film to well separated four peaks at 120 W film. This is consistent with *HL* mappings, considering that the *HL* mappings are measured along the diagonal direction $[HH0]_{pc}$ in *HK* plane.

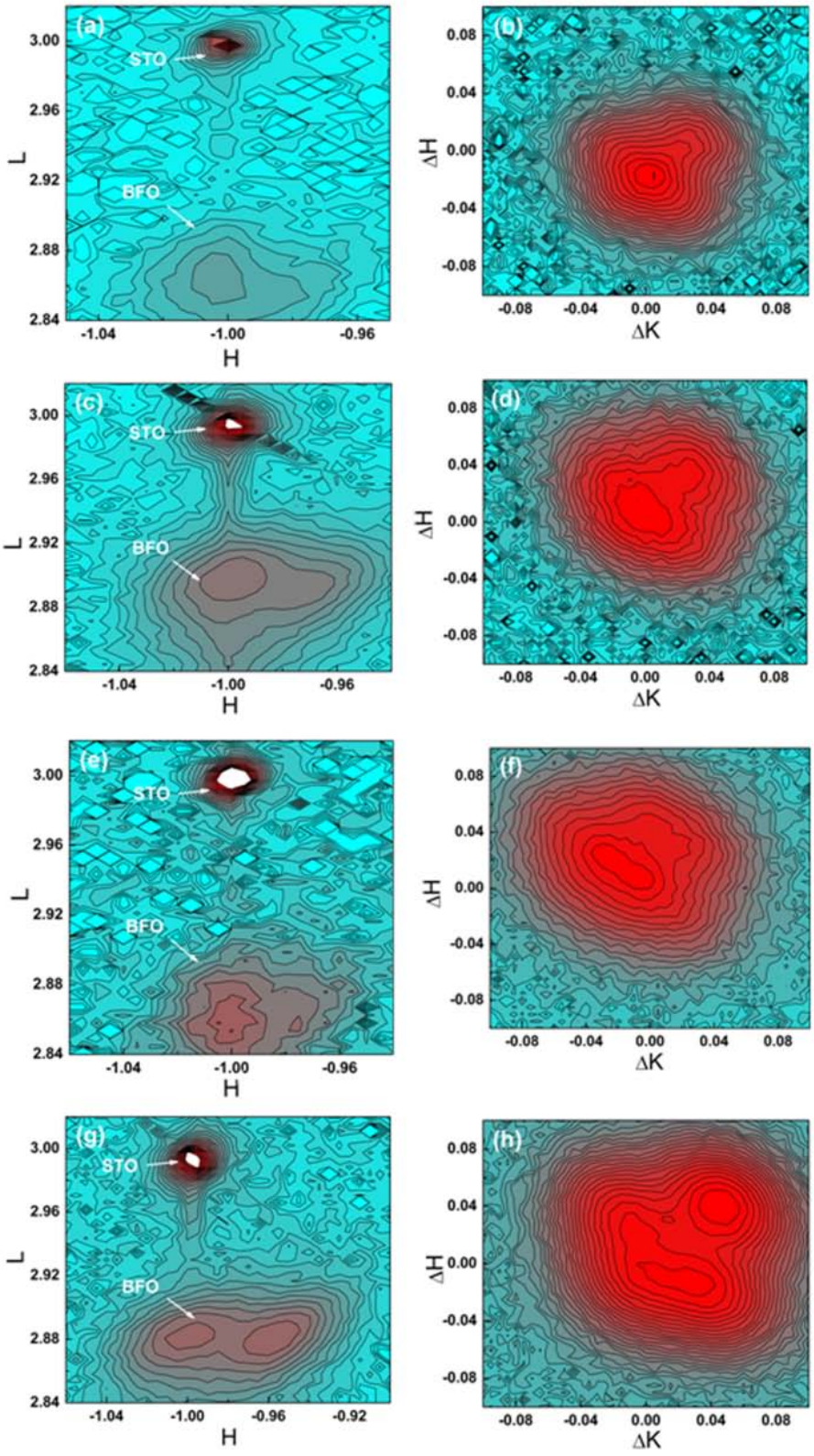

Figure 4.1 (-1-13)$_{pc}$ *HL* plan RSM of BFO films grown at the sputtering power of (a) 30 W, (c) 60 W, (e) 90 W, (g) 120 W. *HK* plan reciprocal space mappings at *L* = BFO in the (-1-13)$_{pc}$ *HL* mappings for films of (b) 30 W, (d) 60 W, (f) 90 W, (h) 120 W.

Due to the presence of twins or domains with different orientations, the monoclinic phase in bulk single crystal is not easily differentiated from tetragonal nano-twins using the X-ray diffraction data [78]. However, as a result of the fixed orientation of out-of-plane direction in the epitaxial thin film, it is simplified owing to the fact that the splitting of peaks is only from the axis perpendicular to the fixed direction [51]. Figure 4.2 (a) shows the schematic configurations of reciprocal space for monoclinic phase epitaxial (001) thin films without out-of-plane twinning rotation. Due to this fixed orientation of *c* axis along the out-of-plane direction, there is no splitting of *c* domains. The presence of twins for *a* domain in the monoclinic phase results in the splitting of spots in the vertical $(H0L)_m$ plane, shown by two open circles with full and broken lines. At the same time, the twins of *b* domain give rise to the splitting of spots within *HK* plane, shown by filled circles. In our previous work [79], a monoclinic phase with out-of-plane twinning rotation was identified, which leads to low leakage current and enhanced polarization. As a result of this out-of-plane twinning rotation (shown by the curved arrows in Figure 4. 2 (a)), the *c* axis is not fixed any more, as shown in Figure 4.2 (b). After rotation the splitting of spots from *c* domain and *b* domain within the HK plane results in four symmetric peaks in the *HK* mapping around (00L), which was clearly demonstrated in *HK* (002) RSM of Ref. [79]. For monoclinic M_A or M_B phase, the monoclinic lattices are rotated by 45° along the plane normal direction with respect to substrate cubic lattices. Therefore, the mappings around $(HHL)_{pc}$ equals to $(H0L)_m$,

specifically $(-1-13)_{pc}$ is equivalent to $(-203)_{m}$. In Figure 4.2 (b), the $(H0L)_{m}$ peaks are split to four peaks without symmetry due to the radical direction of the rotation axis. When measuring the *HL* mappings, the vertical plane passing through the origin was used to cut through the *3D* reciprocal space. Hence, only two spots within this vertical plane were measured (shown by two open circles with full and broken lines in Figure 4.2 (b)), while the filled spots from *b* domain twins would be missed. This was illustrated in Figure 4.2 (c), which agrees with the HL mappings obtained experimentally as shown in Figure 4.1. For the *HK* mappings, the measuring plane would cut all four spots within *HK* plane. This is drawn in Figure 4.2 (d), which explains the split four peaks observed in *HK* mappings in Figure 4.1. Variant splitting of peaks results from different monoclinic distortion angle β for different growth rate samples. Based on the above analysis, the phase in the BFO films grown from the sputtering power of 30 to 120 W was identified to be monoclinic phase with out-of-plane twinning rotation. The lattice parameters (Figure 4.4) derived from the mappings confirm this monoclinic phase, which belongs to M_A lattice because of in-plane compression.

The $(002)_{pc}$ and $(-103)_{pc}$ HL RSM of the BFO films grown at the sputtering power of 150 and 180 W are shown in Figure 4.3. For the 150 W sample (Figure 4.3 (a) and (b)), the BFO film exhibits two peaks with L value widely separated both in $(002)_{pc}$ and $(-103)_{pc}$ mappings. These two peaks are not split, indicating a tetragonal lattice for both

phases. The peak with small L value is corresponding to c = 4.096 (1) Å and c/a ~ 1.05 (T_1), while for the peak at large L value matching c = 4.673 (1) Å and c/a ~ 1.23 (T_2). The giant c/a ratio of T_2 phase is close to those of previous reports [52, 64], but our sample shows a tetragonal lattice rather than monoclinic one. For the 180 W film, the tetragonal phase T_1 disappeared, leaving only the single super-tetragonal phase T_2.

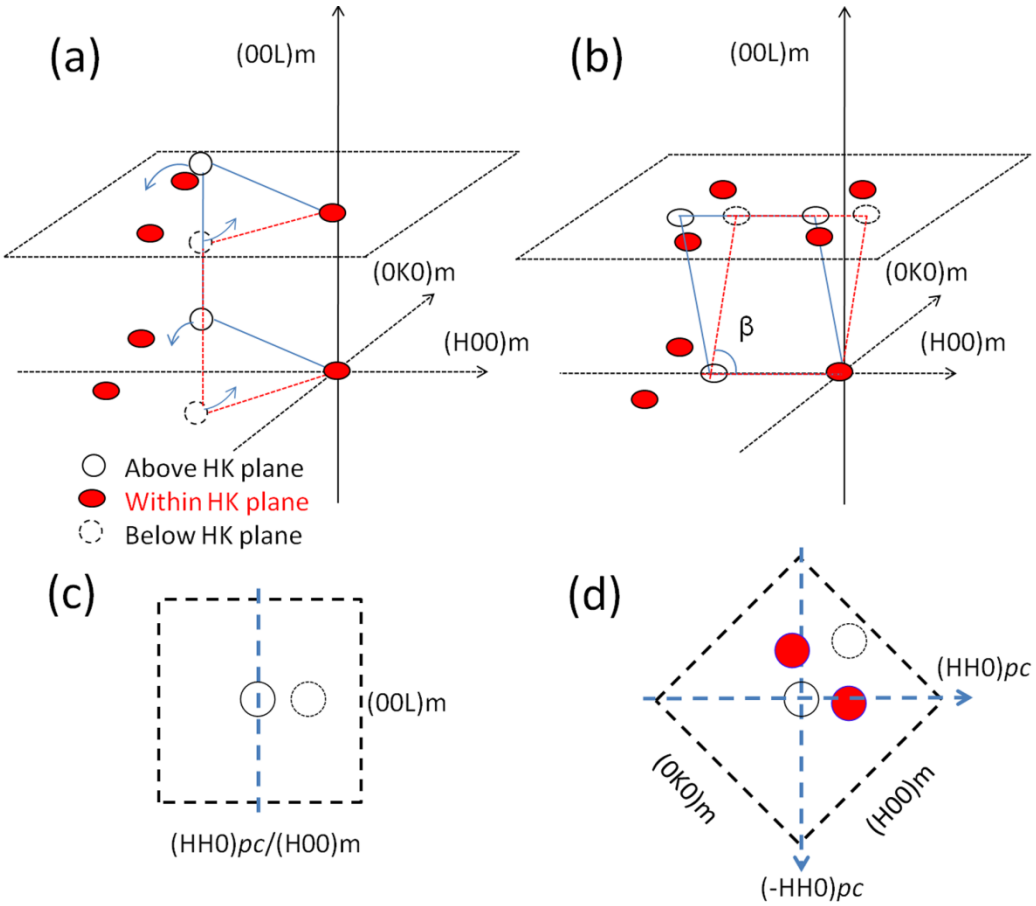

Figure 4.2 Schematic illustrations of reciprocal space for monoclinic phase, (a) monoclinic phase without out-of-plane twinning rotation, (b) monoclinic phase with out-of-plane twinning rotation in *3D* reciprocal space. (c) and (d) show the *HL* plane and *HK* plane mapping of the monoclinic M_A phase with out-of-plane twinning rotation in (b), respectively.

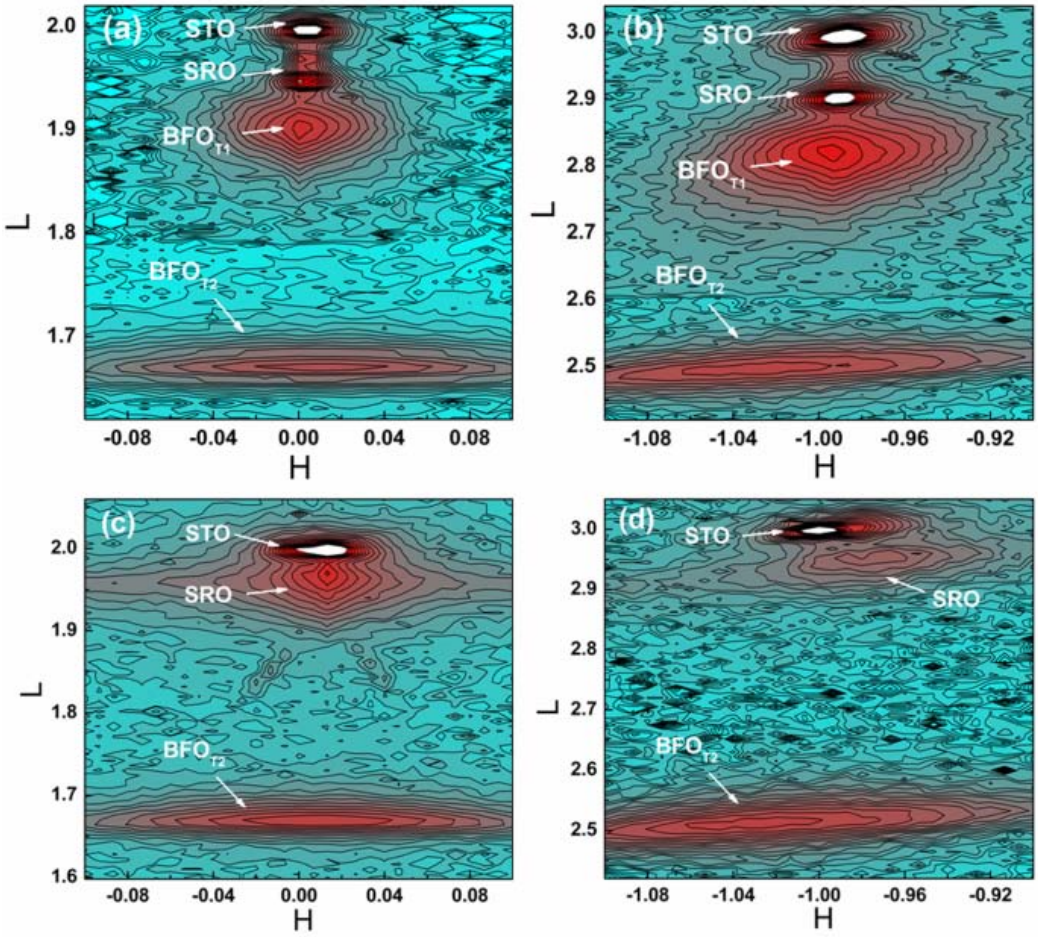

Figure 4.3 $(002)_{pc}$ *HL* plane reciprocal space mappings of BFO films grown at the sputtering power of (a) 150 W and (c) 180 W, $(-103)_{pc}$ *HL* plane reciprocal space mappings of BFO films grown at the sputtering power of (b) 150 W and (d) 180 W.

Figure 4.4 plots the lattice parameters and *c/a* ratio of the BFO films grown at the sputtering powers from 30 to 180 W, showing two phase transitions. The first one is from monoclinic phase to a mixture of two tetragonal phases, T_1 and T_2, at the sputtering power of 150 W, corresponding to the growth rate of ~37 Å/min. The second phase transition is from the mixture of the two tetragonal phases to a single super-tetragonal

phase T_2 with giant *c/a* ~1.23. In addition to the external stimuli such as temperature, stress or strain, electrical and magnetic field, our results demonstrate that the growth rate is also a tunable parameter that can be employed to trigger phase transitions in ferroelectric epitaxial thin films.

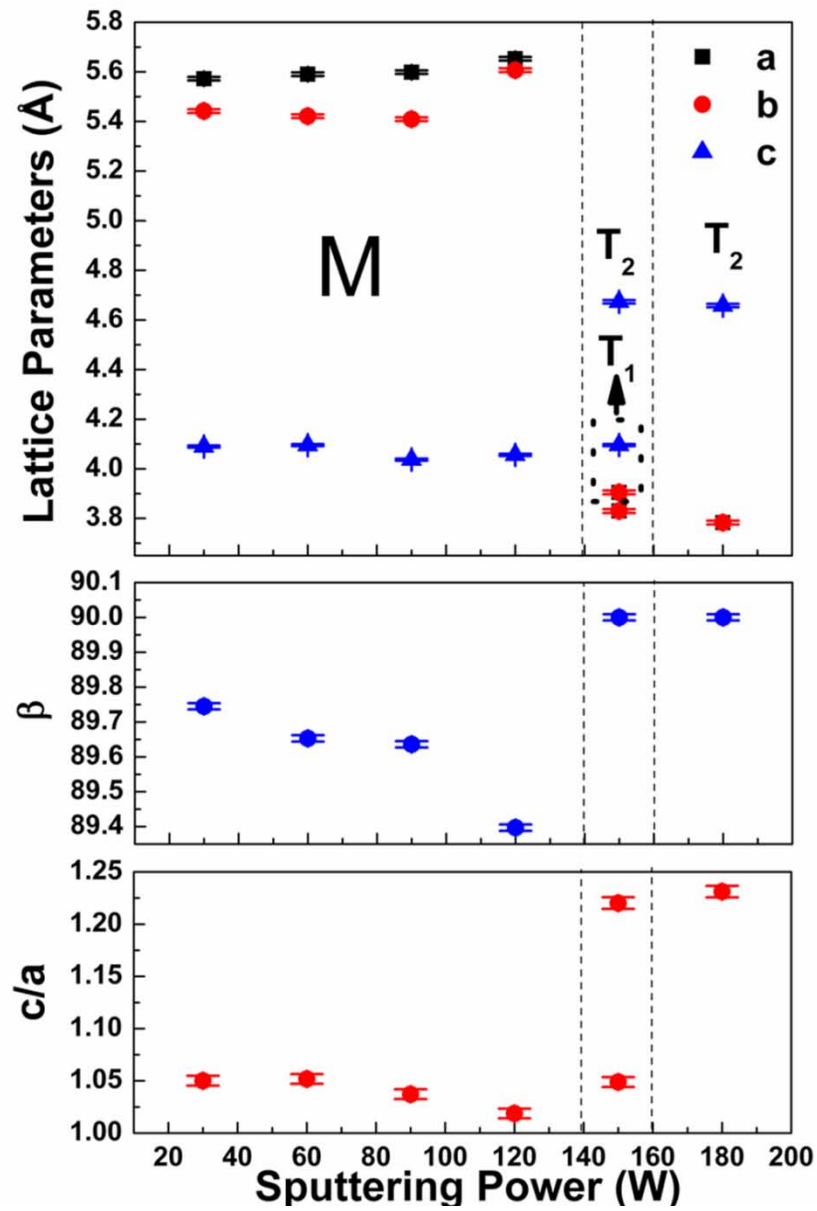

Figure 4.4 Lattice parameters, monoclinic distortion angle β and *c/a* of BFO films grown at the sputtering power from 30 W to 180 W.

4.3 Origin of Super-tetragonal $BiFeO_3$ Phase with a Giant *c/a* ratio on $SrTiO_3$ (001) Substrates

In this section, by using high resolution synchrotron X-ray diffraction, atomic force microscopy (AFM) and transmission electron microscopy (TEM), the parasitic β-Bi_2O_3 (BO) phase is found to coexist with super-tetragonal BFO phase in the BFO film grown at the sputtering power of 180 W. By comparing the BFO films grown with and without BO buffer layer at low growth rate on SRO/STO substrates, the BO phase is identified to strongly associate with the stabilization of super-tetragonal BFO phase. In addition, we have built a structure model to provide details on the lattice mismatch and strain accommodation between the BO phase and BFO giant tetragonal phase. Furthermore, our collaborators have performed ab initio calculations, which show that the super-tetragonal BFO phase exhibits a lower level of total energy than that of monoclinic BFO phase when BO phase is present [80]. These results can help understand the high leakage measured for the BFO samples with giant *c/a* ratio, where there is a poosible coexistence of small amount of highly conductive BO phase. This prevents the room temperature measurement of giant polarization as predicted theoretically.

To check the possible phases present in the BFO film grown at a sputtering power of 180

W on SRO/STO substrate, high resolution X-ray diffraction scan along *L* direction around (002) in the reciprocal space was measured from *L* value 1 to 2 (Figure 4.5 (a)). In addition to the diffraction peaks from STO, SRO and BFO, a peak at $L = 1.43$ was clearly shown, which is corresponding to (002) lattice spacing of β-BO phase. The *L* scan around (-103) also gives rise to the peak from this phase at $L = 2.14$ (Figure 4.5 (b)). (-103) Φ scans shown in Figure 4.5 (c)~(f) reveal the in-plane epitaxial relationship between BFO, BO, SRO and STO, demonstrating a four-fold symmetry. To establish a detailed crystal structure of this BO phase, reciprocal space mappings (RSM) were measured as shown in Figure 4.6. In the *HL* (002) RSM (Figure 4.6 (a)), a horizontally elongated peak of BO phase is shown to exist at $L \sim 1.43$, which is similar to the (002) RSM from BFO. This suggests an intimate contact between BFO and BO lattice in the film with a large degree of out-of-plane orientation. From a single peak in (-103) RSM (Figure 4.6 (b)), the BO phase was identified as a tetragonal β-BO with lattice parameters $a = 7.913(2)$, $c = 5.462(1)$ Å.

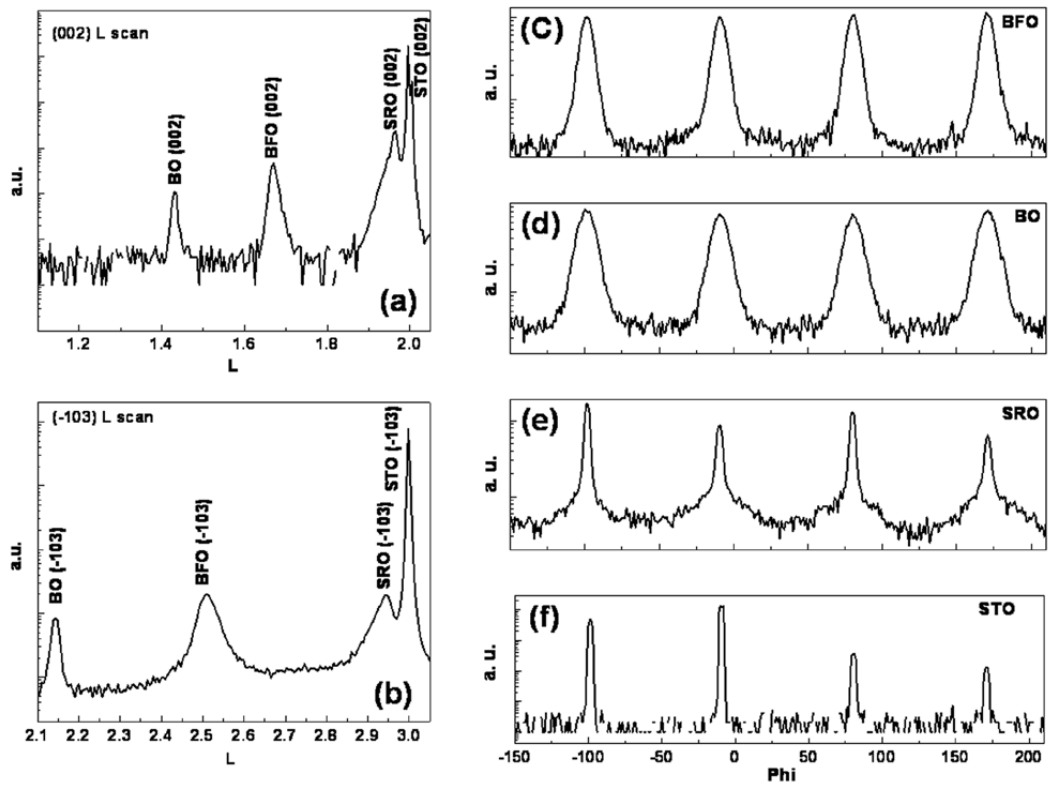

Figure 4.5 High resolution X-ray diffraction *L* scans around diffraction peaks of (002) (a) and (-103) (b). (-103) *Φ* scans of BFO (c), BO (d), SRO (e), and STO (f) lattice for the BFO film sputtered at 180 W on SRO/STO substrate.

The presence of BO phase at high growth rate but not at low rate can be understood as follows. As the growth rate increases, more Bi would be stabilized as BO phase in the films due to more Bi atoms being sputtered with less time allowed to be evaporated. The BFO films grown at very high oxygen pressure also show the existence of BO phase in two previous reports [31, 81]. In both reports (Figure 4(a) in Ref. [31] and Figure 1 in Ref. [81]), there was an unidentified peak in the X-ray diffraction (XRD) spectrum at $2\theta \sim 39^\circ$, corresponding to the (002) peak of super-tetragonal BFO phase. In our previous work [82], for the BFO films sputtered at power of 150 W, a weak XRD peak attributed

to BO phase was also observed, in addition to the strong peaks of the two tetragonal phases of BFO (not shown). Therefore, the super-tetragonal BFO phase was indeed in coexistence with the BO phase on STO substrates. In addition, the BO phase shares the same tetragonal symmetry with a reasonable lattice mismatch with super-tetragonal BFO phase. These observations lead us to speculate of the possible contribution of BO phase to the formation of super-tetragonal BFO phase.

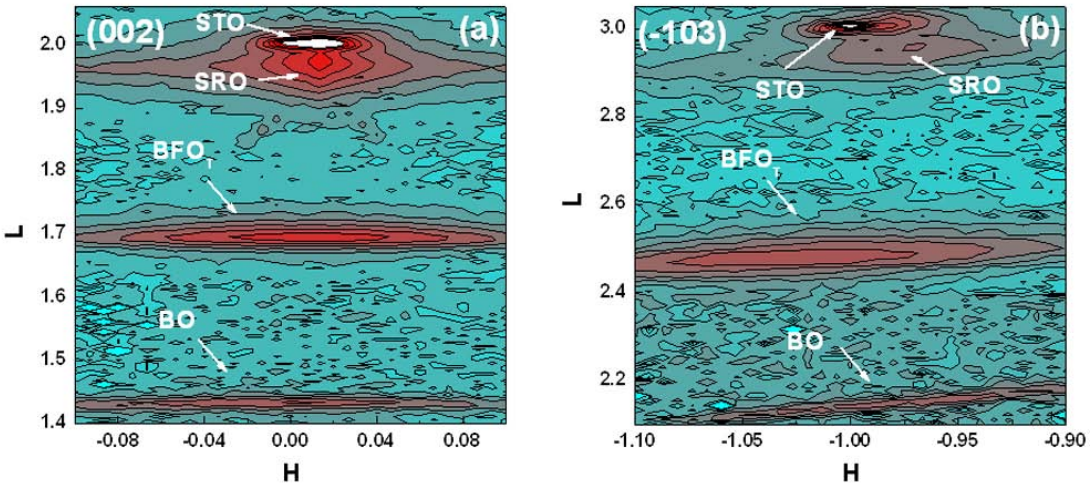

Figure 4.6 (a) (002) *HL*, (b) (-103) *HL* reciprocal space mappings of BFO film sputtered at 180 W on SRO/STO substrate.

In order to confirm the role of BO phase played in triggering the formation of super-tetragonal BFO phase, BFO film of 180 nm in thickness was grown on BO-buffered SRO/STO substrate at a sputtering power of 120 W. This growth rate has been demonstrated to lead to monoclinic M_A phase for the BFO film deposited on SRO/STO substrate without BO buffer layer in Ref. [79]. As shown in Figure 4.7 (a), the

BFO film grown with BO buffer layer shows a (002) peak corresponding to the super-tetragonal phase (thick line) while the film grown directly on SRO-buffered STO substrate shows a (002) peak with lattice spacing of monoclinic phase (thin line). The *L* scan around (-103) in Figure 4.7 (b) also confirms the super-tetragonal phase being induced in the BFO film deposited on BO buffer layer. HL reciprocal space mappings of (002) (Figure 4.7 (c)) and (-103) (Figure 4.7 (d)) were measured to determine the detailed structure of the BO-buffered BFO film grown on SRO/STO substrate. In both mappings, the BFO phase shows a single peak, indicating a tetragonal symmetry. Also, the BO phase shows the same tetragonal symmetry as in the BFO film grown at 180 W in Figure 4.6. The lattice parameters for BO buffer layer are a = 8.230 (2), c = 5.397 (1) Å, while those for the BFO phase are a = 3.782 (2), c = 4.681 (1) Å.

The real space arrangement of BFO phase and BO phase in 180W sample is studied using AFM and cross-section TEM, in order to clarify how BO phase can stabilize the super-tetragonal BFO phase on STO substrate. The in-plane AFM image (Figure 4.8 (a)) shows a large amount of square-like outgrowth from the surface of BFO film sputtered at 180 W. This outgrowth was also shown in a previous report of BO excess films [83]. From the TEM cross-section image (Figure 4.8 (b)), the outgrowth island is about 40 nm in height. For the elementary distribution in the film, EDX mappings reveal that Bi element cover both the film and outgrowth island while the Fe element shows a lower

intensity at the interface between the film and island. Therefore, the island outgrowth is introduced by BO phase presented in the film. At the BFO/SRO interface, the Bi element shows a higher intensity than Fe. This implies that BO phase acts as an inducing layer for BFO super-tetragonal phase in the film sputtered at 180W.

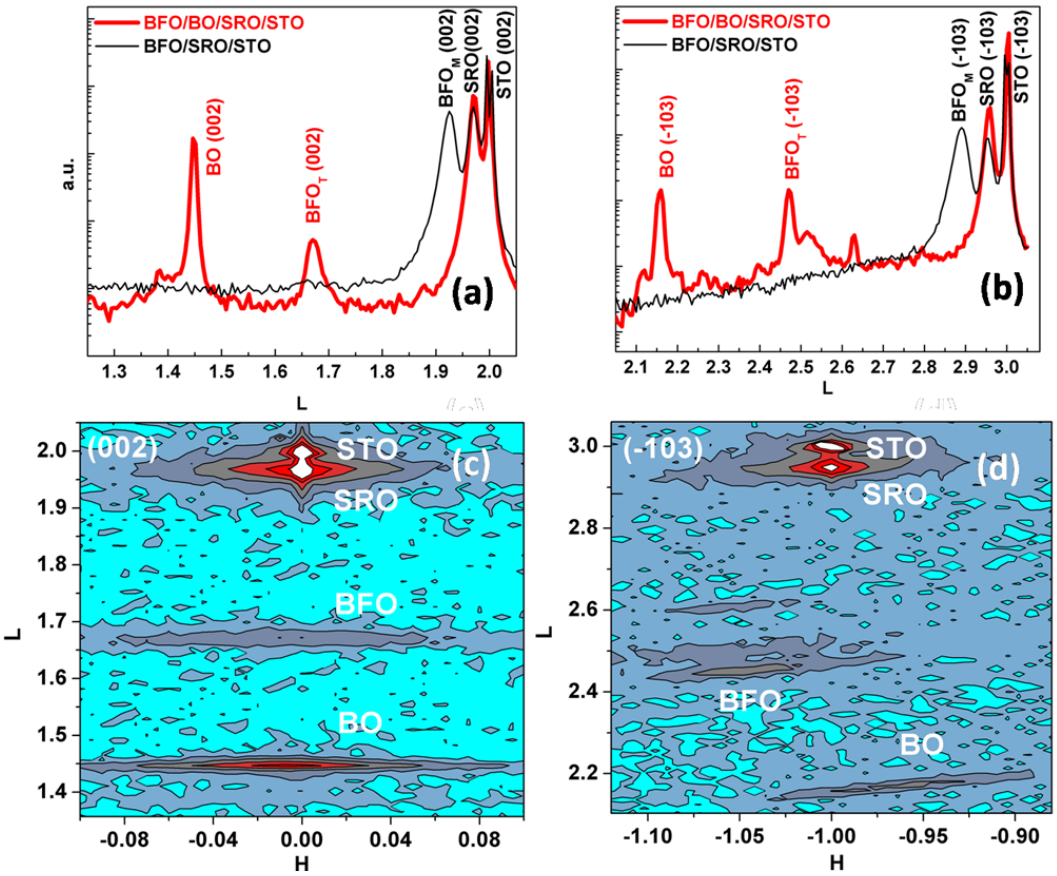

Figure 4.7 High resolution *L* scans of (002) (a) and (-103) (b) for BFO thin films grown at 120 W with (thick lines) and without BO (thin lines) buffer layer on SRO/STO substrate. (c) (002) *HL*, (d) (-103) *HL* reciprocal space mappings of 120 W BFO film grown with BO buffer layer on SRO/STO substrate.

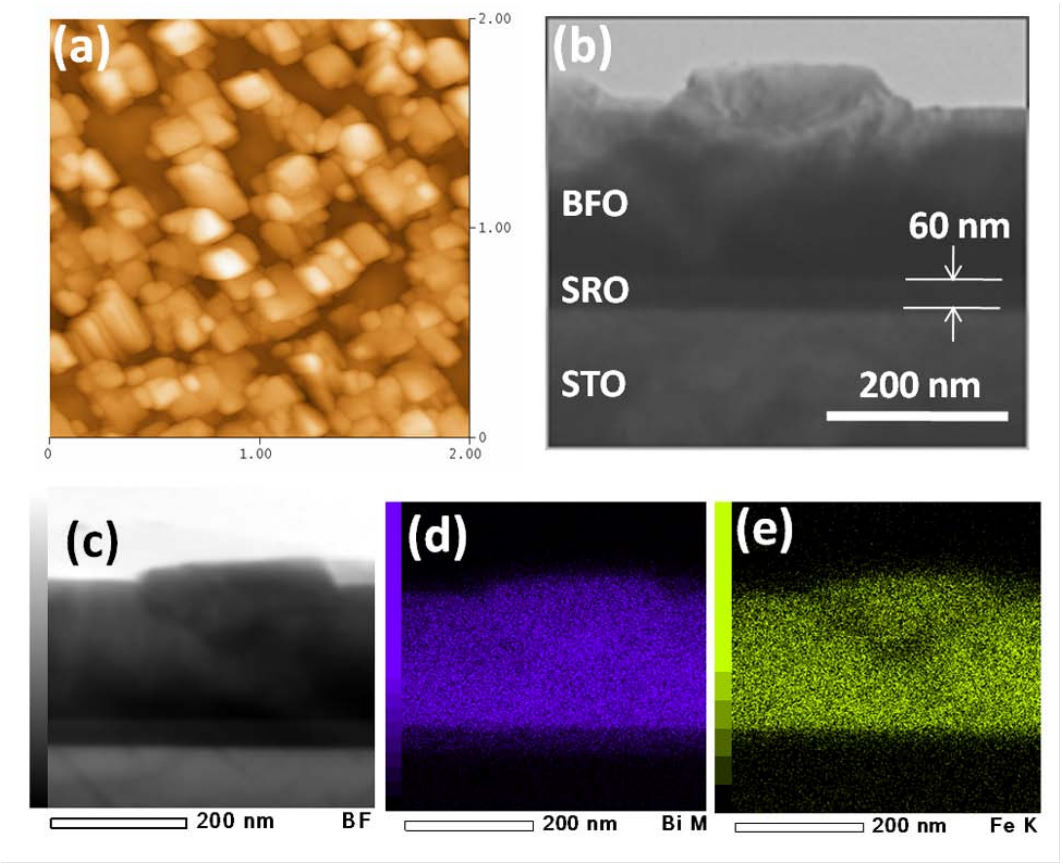

Figure 4.8 (a) In-plane AFM image with the scan area 2 by 2 μm. (b) Cross-section TEM image and EDX mapping with image (c), Bi M edge (d) and Fe K edge (e) of the BFO film sputtered at 180 W on SRO/STO substrate.

The experimental results of BFO lattice derived from high resolution TEM study of the film sputtered at 180 W on SRO/STO substrate agree well with that of the XRD result, i.e., c ~ 4.6 Å, as shown in Figure 4.9 (a). The single-crystal like lattice of BO phase in the BFO film grown at 180 W is also consistent with XRD data. Two types of relationship between BO phase and BFO super-tetragonal phase were generally found in the film, which is consistent with EDX mappings. One is the existence of BO phase at the BFO/SRO interface (Figure 4.9 (c)), acting as a buffer layer for the growth of BFO super-tetragonal phase. The other one is BO phase being sandwiched between BFO

phases, leading to the formation of island outgrowths at the film surface, as shown in Figure 4.9 (d). A further common phenomenon is that dislocations and disorders of atomic arrangement occur around the region of BO phase to accommodate the lattice mismatches, which can be seen around the dashed lines in the TEM images of Figure 4.9 (c) and (d).

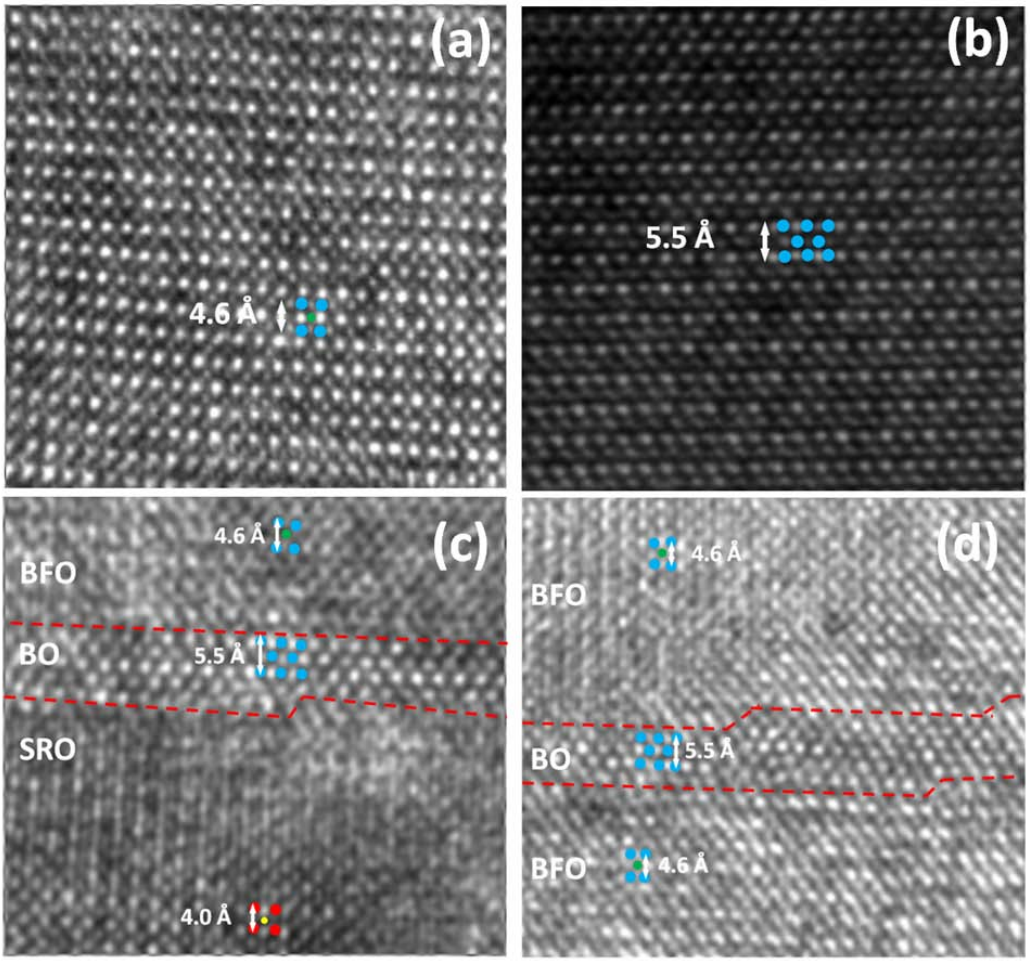

Figure 4.9 High resolution bright field TEM images of the BFO super-tetragonal lattice (a) and BO lattice (b) in the film sputtered at 180 W on SRO-buffered STO substrate. (c) BO lattice at the BFO/SRO interface, (d) BO lattice sandwiched between BFO super-tetragonal lattices.

Based on the XRD and TEM results, a structure model is proposed to clarify the arrangement of BFO lattice with BO phase in the BFO film. The tetragonal *β*-BO lattice, as outlined with *a, b* and *c* axes in Figure 4.10 (a), has a 45° in-plane relationship with the cubic *δ*-BO lattice. As the in-plane lattice parameter of the super-tetragonal BFO phase (*a* = 3.779 Å) is about half of *β*-BO phase (*a* = 7.913 Å), there would be four unit cells of BFO lattice on one unit cell of BO lattice. One of the BFO unit cells is drawn in Figure 4.10 (a). The cross-section view of the SRO/BO/BFO lattice in the *ac* plane is shown in Figure 4.10 (b). The in-plane lattice mismatch between SRO (*a* = 3.962 Å) and BO is only ~0.1%. Therefore BO phase can easily grow epitaxially on SRO/STO substrate. Although the lattice mismatch between BO and super-tetragonal BFO is about ~4.5%, which is quite large for epitaxial growth, experimentally it was found that BO phase prompts the formation of BFO super-tetragonal phase rather than monoclinic phase on STO substrates.

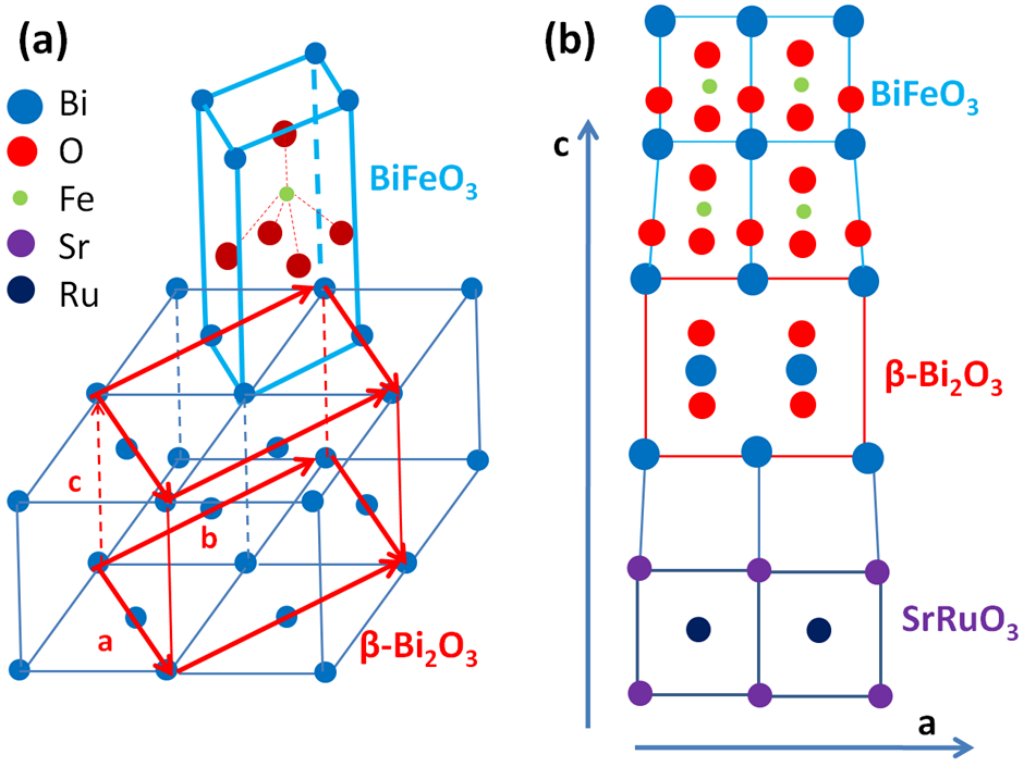

Figure 4.10 (a) Three dimensional schematic interface structure model for BFO and BO lattice, the oxygen atoms in the BO lattice were not included for easier visualization. (b) Cross-section view of the SRO/BO/BFO lattice in the *ac* plane.

4.4 Summary

In summary, epitaxial BFO thin films were deposited on STO (001) substrates at different growth rates by varying the RF sputtering power from 30 to 180 W. Two phase transitions were identified by high resolution X-ray diffraction RSM, from the monoclinic phase to a mixture tetragonal phases of T_1 and T_2, then to a single super-tetragonal T_2 phase. The super-tetragonal phase is formed at sputtering power above 150 W or growth rate larger than ~37 Å/min. The growth rate induced phase

transitions promise as an alternative pathway to control new phases in ferroelectric epitaxial thin films.

By detailed structure analyses using high resolution synchrotron X-ray diffraction, a parasitic β-BO phase is identified to coexist with the super-tetragonal BFO phase in BFO film deposited at sputtering power of 180 W on SRO/STO substrate. At a fixed sputtering power of 120 W, the BFO film grown directly on SRO/STO substrate shows a monoclinic phase, whereas the BFO film deposited on BO-buffered SRO/STO substrate demonstrates a super-tetragonal phase. This result confirms that the parasitic β-BO phase is largely responsible for the formation of super-tetragonal BFO phase in the film deposited on STO substrates. By combined XRD, AFM and TEM studies, the detailed lattice alignment relationship of β-BO phase and super-tetragonal BFO phase in the film is clarified, showing four super-tetragonal BFO lattices match one BO lattice in the in-plane dimension. The experimental results are supported by the *ab initio* calculations conducted by one of our collaborators [80], where the super-tetragonal BFO phase is shown to be more stable than monoclinic phase when BO is present.

BO phase is known to be highly conductive [83]. It could act as a bottom electrode and buffer layer of inducing super-tetragonal BFO phase at the same time. This opens an alternative route for forming the super-tetragonal BFO phase on single crystal substrates

(for example, STO) and even polycrystalline substrates, when the BO phase is properly controlled as a buffer layer. In a previous report [84], parasitic iron oxide is demonstrated to modify the strain relaxation process and improve the magnetic properties of multiphase Bi-Fe-O films while maintain the insulating behaviour. The experimental results in the present work, together with those of previous reports, indicate that parasitic phases are not always detrimental to the physical properties of thin films, which could be utilized to induce new phases.

Chapter 5. HIGHLY STRAINED EPITAXIAL $BiFeO_3$ THIN FILMS ON $NdCaAlO_4$ AND $LaAlO_3$ (001) SUBSTRATES

5.1 Introduction

In most of the previous reports, highly compressive strained BFO films are deposited on LAO (001) substrates with a large lattice mismatch of ~ 4.5 %, which show a monoclinic M_C structure [52, 64]. According to the first principles calculations [54], when deposited on substrates with higher compressive strain than LAO, the BFO film will form super-tetragonal phase with the space group of *P4mm*. However, strict super-tetragonal BFO phase has not been experimentally demonstrated. Strictly super-tetragonal BFO phase is interesting, as the polarization is predicted to be ~150 $\mu C/cm^2$ along <001> direction from theoretical calculations [54]. This giant polarization value is of promising value for device applications such as in random access memories and ferroelectric tunnel junctions.

To obtain the strict super-tetragonal phase BFO film, two approaches are taken in this chapter. The first one is to use substrates with higher compressive strain than LAO. One such candidate of single crystal substrate with smaller in-plane lattice parameter is orthorhombic $YAlO_3$ (YAO) (110), which gives a 6.9% compressive strain. However, the fully strained BFO film grown on YAO is reported to be in a monoclinic M_C phase [50]. This is probably due to the anisotropic in-plane strain due to the orthorhombic symmetry of YAO substrate. In fact, the fully strain driven super-tetragonal undoped BFO phase has not been demonstrated experimentally. Single crystal $NdCaAlO_4$ (NCAO) substrate exhibits a tetragonal lattice with $a = b = 3.685$ Å, $c = 12.12$ Å. The (001) oriented NCAO substrate has an in-plane compressive misfit strain of ~ 7% with BFO. In this chapter, NCAO substrate will be employed to grow BFO films for developing the super-tetragonal crystal structure. The second approach to obtain strict super-tetragonal phase is to grow ultrathin film on LAO (001) substrate. In the literature, no detailed crystal structure study has been made to BFO films less than 10 nm on LAO (001) substrate [32, 50, 52, 53, 64]. It is interesting to see whether ultrathin film will show different crystal structure other than the observed monoclinic M_C phase. In the following two sections of this chapter, experimental results on the basis of these two approaches will be presented.

The ferroelectric behaviour of tetragonal-like M_C phase BFO film on LAO substrate

has not been properly characterized experimentally as the rhombohedral-like M_A phase start to merge when the film thickness reaches 25 nm [65]. The single tetragonal-like M_C phase can only be obtained in very thin films below 25 nm in thickness, which is too leaky to measure reliable ferroelectric polarization. However, from the results in chapter 4, the super-tetragonal phase can form even for film with 180 nm in thickness when grown at high growth rate on (001) STO substrates, as this super-tetragonal phase is not strain driven and has no thickness limit. However, the large amount of conductive Bi_2O_3 phase impedes the ferroelectric measurement when grown on STO substrate. By employing the high compressive strain from LAO substrate, the amount of Bi_2O_3 may well be reduced for the formation of super-tetragonal phase BFO at high growth rate. In section 5.4 of this chapter, the crystal structure and ferroelectric properties of BFO thin films deposited at different growth rates on SRO-buffered LAO (001) substrate will be further explored.

5.2 Thickness Dependent Structure Evolution of $BiFeO_3$ Thin Films on $NdCaAlO_4$ (001) Substrates

Figure 5.1 shows XRD patterns of NCAO substrates (a) and BFO films with thickness of 30 nm (b), 180 nm (c) and 720 nm (d) on NCAO substrates, respectively. The NCAO single crystal substrate has pure (001) orientation with only (00L) diffraction

peaks being observed. The out-of-plane lattice parameter *c* is around 12.12 Å, which is calculated from the 2θ angles. The XRD pattern of 30-nm-thick BFO film on NCAO substrates shows two diffraction peaks, labeled as BFO (001) and (002) in Figure 5.1(b). These peaks agree with those of the super-tetragonal phase BFO, with out-of-plane lattice parameters around 4.6 Å. As the film thickness increases to 180 nm, besides the diffraction peaks (BFO-1) from the super-tetragonal phase BFO, two additional peaks occur in the XRD pattern, which are labeled by BFO-2 in Figure 5.1 (c). The out-of-plane lattice constant of the new XRD peaks is close to that of bulk BFO, which is called bulk-like BFO phase here. This indicates a mixture of two BFO phases formed at the film thickness of 180 nm. For the 720 nm BFO film, strong diffraction peaks from only bulk-like BFO phase were observed. Therefore, from the XRD results, BFO film deposited on NCAO substrates shows a single super-tetragonal phase at 30 nm in film thickness, which then develops to the mixture two phases at 180 nm and finally evolves to a single bulk-like phase at 720 nm.

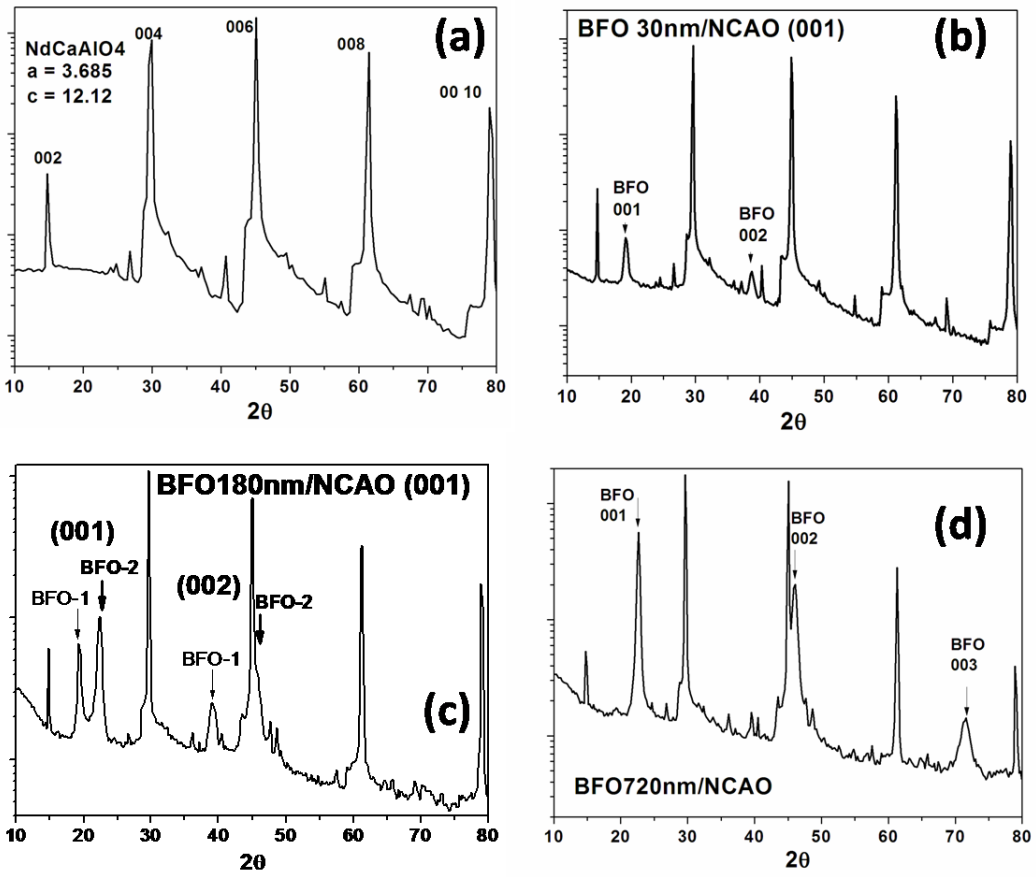

Figure 5.1 X-ray diffraction patterns of NCAO substrates (a), BFO films with thickness of 30 nm (b), 180 nm (c) and 720 nm (d) on NCAO substrates.

To characterize the detailed crystal structure of BFO films on NCAO (001) substrates, reciprocal space mappings from high resolution synchrotron X-ray diffraction were measured for all three samples. Figure 5.2 shows the (006) and (-109) RSM of 30-nm-thick BFO film on NCAO substrates. Both mappings show a single diffraction peak from BFO film. This is different from the reported *Mc* phase BFO on LAO substrates [85], which shows a splitting of two or three peaks due to the monoclinic distortion of BFO lattice. The RSM results demonstrate the strict tetragonal symmetry of BFO lattice on NCAO substrates with a compressive strain of 7%. The lattice

parameters of this super-tetragonal phase BFO are measured to be a = 3.779 Å and c = 4.662 Å, which gives a giant c/a of 1.23.

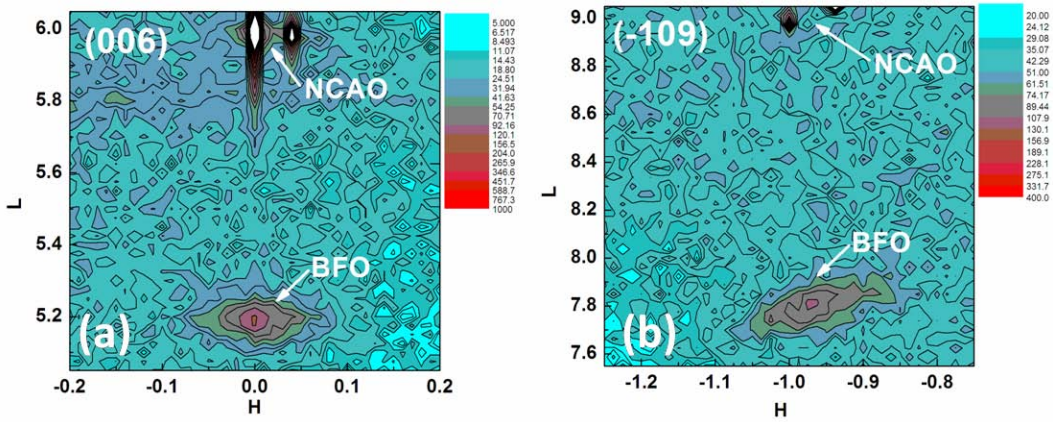

Figure 5.2 (006) (a) and (-109) (b) *HL* reciprocal space mapping of 30-nm-thick BFO film on a NCAO substrate

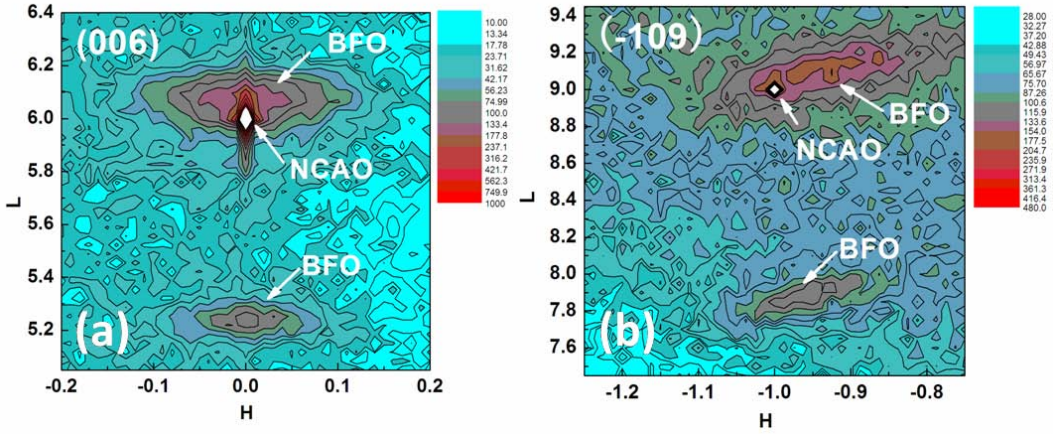

Figure 5.3 (006) (a) and (-109) (b) *HL* reciprocal space mapping of 180-nm-thick BFO film on a NCAO substrate

For the 180-nm-thick BFO thin films on NCAO substrates, in agreement with the line scan in Figure 5.1(c), the RSM around (006) in Figure 5.3 shows two diffraction peaks

located above and below the substrate peaks. The BFO peak at L ~ 6.1 has a out-of-plane lattice parameter of 3.995 Å, which is close to the lattice parameters of bulk BFO. While the other BFO peak at L ~ 5.2 corresponds to out-of-plane lattice parameter of 4.641 Å, which is consistent with the super-tetragonal BFO phase. The (-109) RSM gives the in-plane lattice parameters for these two phase. The lattice parameters are summarized in Table 4. In contrast to the phase mixture of BFO films on LAO substrates [32], we did not observe the two extra triclinic BFO phases on NCAO substrates. Instead, the two phases in the mixture on NCAO substrate are both tetragonal. This is similar to the phase mixture of BFO film induced by increasing sputtering power on STO substrates discussed in Chapter 4. Both STO and NCAO have strict square in-plane lattice, while LAO doesn't have perpendicular in-plane lattice due to the rhombohedral symmetry at room temperature. This explains the strict tetragonal lattice of BFO film on STO and NCAO substrates but monoclinic lattice of BFO films on LAO substrates. The monoclinic distortion of BFO is due to the in-plane shear strain effect from LAO substrates.

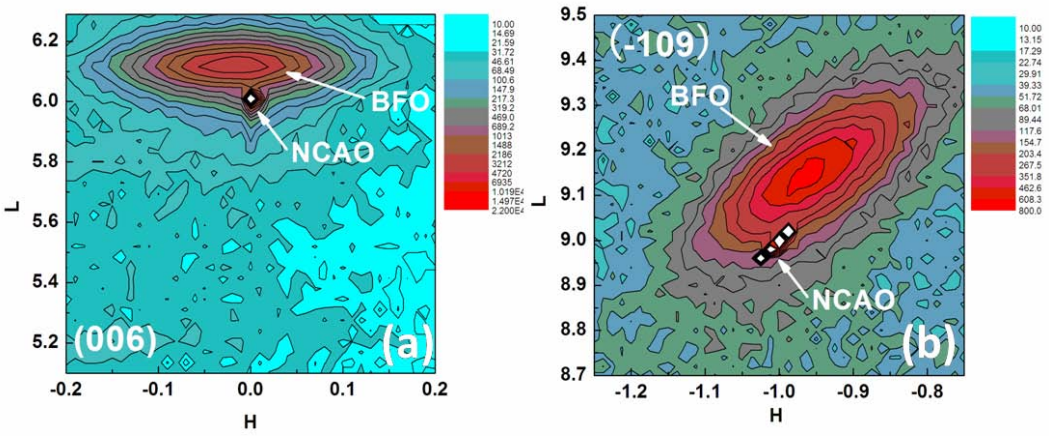

Figure 5.4 (006) (a) and (-109) (b) *HL* reciprocal space mapping of 720-nm-thick BFO film on a NCAO substrate

As for the 720-nm-thick BFO film on NCAO substrate, the RSM in Figure 5.4 shows a single diffraction peak of BFO in both (006) and (-109) mappings, indicating tetragonal symmetry. The out-of-plane lattice parameter derived from the RSM is 3.964 Å, which is extremely close to that of bulk BFO phase (3.96 Å). However, it has a strict tetragonal lattice instead of rhombohedral lattice of bulk BFO. This single BFO phase at 720 nm thickness is called bulk-like tetragonal phase.

Table 4 Thickness dependent lattice parameters of BFO films grown on NCAO (001) substrates

Film thickness (nm)	Structure	a (Å)	c (Å)	c/a
30	Super-Tetragonal	3.779	4.662	1.23
180	Super-Tetragonal	3.823	4.641	1.21
	bulk-like Tetragonal	3.984	3.995	1.003
720	bulk-like Tetragonal	3.874	3.964	1.02
Bulk	Rhombohedral	3.96	3.96	1.00

As a summary, Table 4 lists the evolution of thickness dependent phases and their lattice parameters for BFO films deposited on NCAO substrates. The strictly super-tetragonal BFO phase has been successfully demonstrated on NCAO (001) substrates, with a mismatch strain of -7%.

5.3 Crystal Structure of $BiFeO_3$ Thin Films on $LaAlO_3$ (001) Substrate

Figure 5.5 shows XRD patterns of the BFO film grown directly on LAO (001) substrate. The BFO peaks (001) and (002), corresponds to the out-of-plane lattice constant c = 4.640 Å. The satellite peaks located around the main BFO peaks, which are labeled by small arrows in Figure 5.5, arise from the thickness fringes. This indicates an extremely smooth surface and interface of the as-grown BFO film. Due to the high crystallinity and smooth surface, the Kiessig oscillation is observed in the X-ray reflectivity curve in Figure 5.6 (a). From the oscillation peak positions, the film thickness of BFO is estimated to be 7.5 nm. The AFM image in Figure 5.6 (b) shows a single-unit-cell step structure of BFO film surface, demonstrating the step flow growth mode.

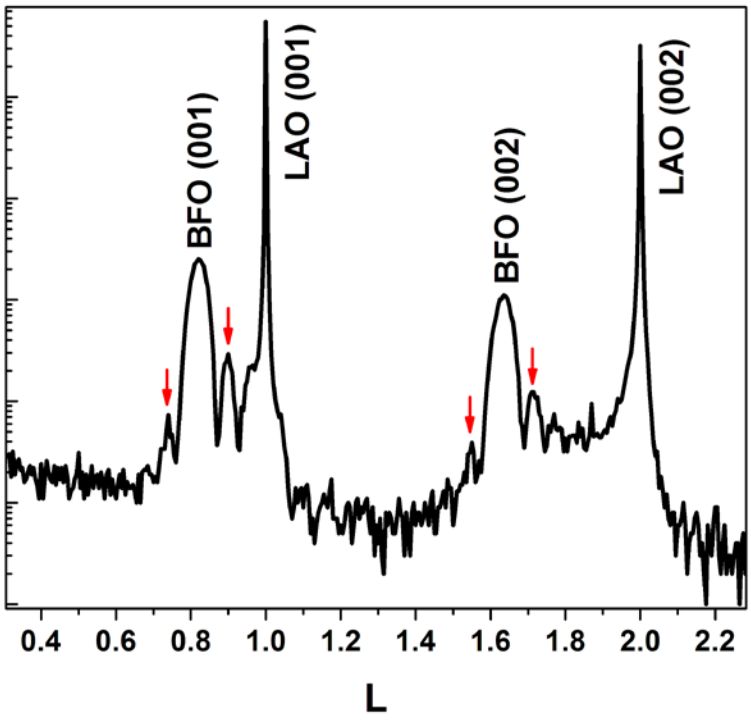

Figure 5.5 *L* scan of 7.5 nm BFO film on LAO (001) substrate

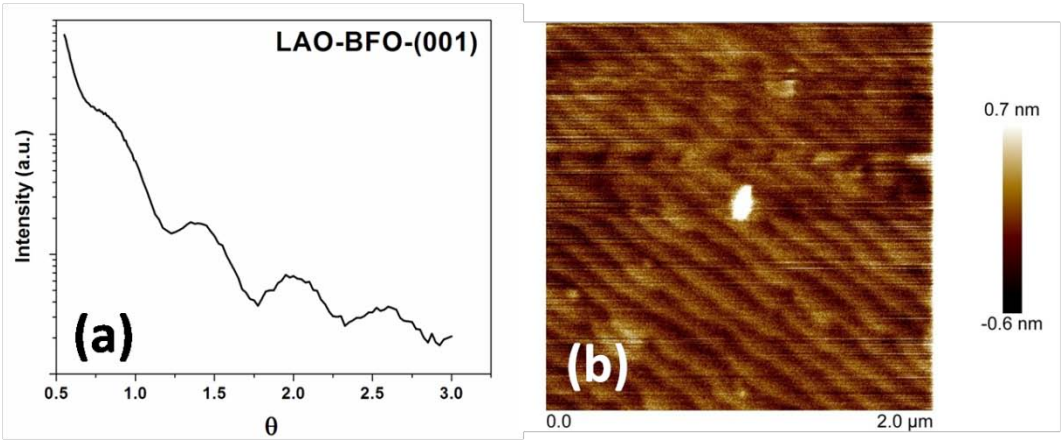

Figure 5.6 X-ray reflectivity (a) and AFM topography image (b) of 7.5-nm-thick BFO film deposited on LAO (001) substrate

To study the crystal symmetry of this ultrathin BFO film deposited on LAO (001) substrate, RSM around (002), (-103), (0-13) and (-1-13) were measured by high

resolution XRD at SSLS. (002) *HL* RSM, as shown in Figure 5.7, indicates a splitting of BFO peaks along H direction. This splitting of BFO peaks follows from the LAO substrate, as can be seen from the two pairs of thickness fringes along *L* direction. The LAO substrate is known to be heavily twinned due to the phase transition during the heating and cooling of film growth [86], which induces the twins formed in BFO film. In the (002) *KL* mapping, the BFO shows only a single peak without any splitting. Therefore, the twin of BFO film is along *H* direction, not along *K* direction.

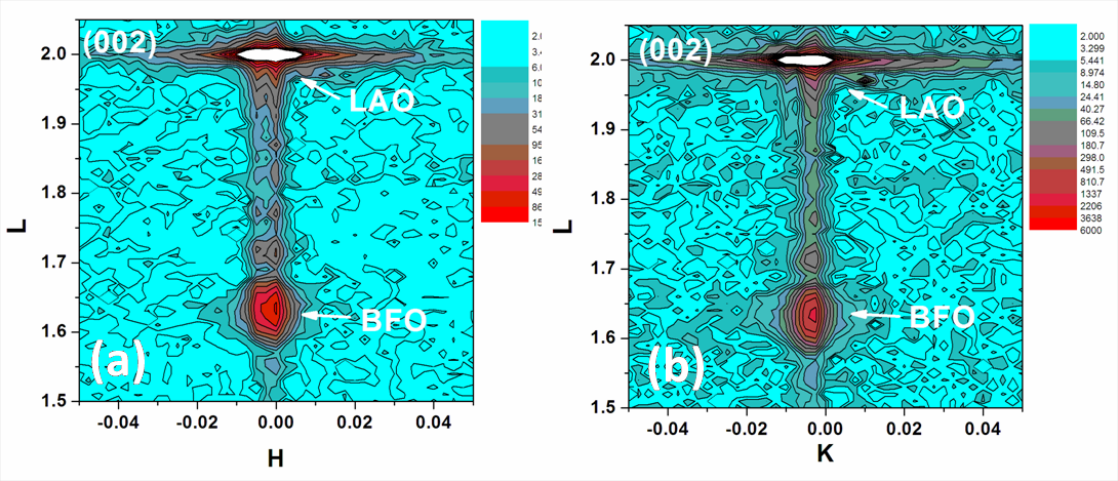

Figure 5.7 (002) *HL* (a) and *HK* (b) reciprocal space mapping of 7.5-nm-thick BFO film on LAO (001) substrate

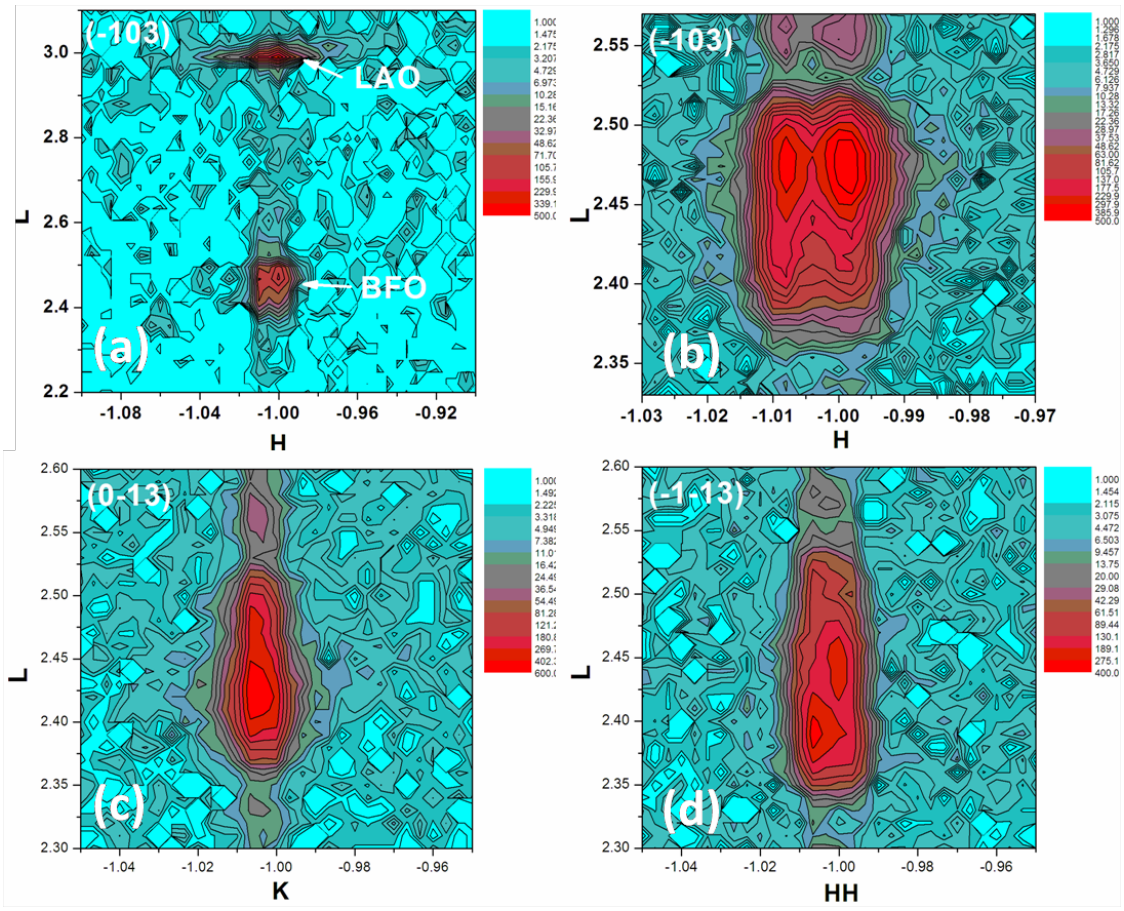

Figure 5.8 (-103) (a), enlarged (-103) around BFO peak (b), (0-13) (c) and (-1-13) (d) RSM of 7.5-nm-thick BFO film on LAO (001) substrate

Figure 5.8 (a) shows the (-103) *HL* mapping, with the enlarged part around BFO being shown in Figure 5.8 (b). The BFO peak has similar splitting when compared to the (002) *HL* mapping, which is induced from the substrate twining structure along *H* direction. The (0-13) mapping shows two peaks and (-1-13) shows three peaks from BFO indicates the monoclinic symmetry of BFO film, as shown in Figure 5.8 (c) and (d). According to the standard peak splitting in the monoclinic phase (Figure 2.7), this BFO film belongs to M_A phase with monoclinic distortion along *K* direction instead of *H* direction. This is different from what has been reported in the literature that fully

strained BFO film of 20 nm in thickness deposited on LAO (001) substrate shows a M_C phase [85, 87]. Interestingly, this reported M_C phase BFO has a phase transition to M_A phase BFO at around 150 ℃ [85]. The BFO film studied here has a film thickness of 7.5 nm, indicating that the high temperature M_A phase BFO is formed at room temperature when the film thickness is reduced. This may result from the strong strain state at ultrathin film thickness below 10 nm, which stabilizes the meta-stable high temperature phase at room temperature. The lattice parameters of M_A phase BFO for this BFO film are a = 3.790 Å, b = 3.771 Å, c = 4.640 Å, β =88.37°. This result suggests that even in ultrathin film on LAO substrate, BFO exhibit the monoclinic symmetry, not the strict super-tetragonal symmetry. This may due to the in-plane shear strain from the substrate because of rhomohedral symmetry of LAO.

5.4 Ferroelectric Behaviour of $BiFeO_3$ Thin Films on $LaAlO_3$ (001) Substrates with $SrRuO_3$ Buffer Layer

In this section, the ferroelectric behaviour of BFO thin films, deposited on LAO substrate with SRO as conductive buffer layer, will be discussed. Figure 5.9 shows the XRD pattern of the BFO thin films deposited on SRO-buffered LAO substrates, grown at different sputtering powers. For the BFO film deposited at 50 W, a single phase was observed in Figure 5.9 (a), with an out-of-plane lattice parameter matching bulk-like

phase. When the sputtering power increases to 100 W, in addition to this bulk-like phase, the super-tetragonal-like phase occurs, as labeled in Figure 5.9 (b). Also, the XRD pattern shows a small peak from Bi_2O_3 (BO). This is similar to what has been observed in the BFO films on SRO/STO (001) substrates in Chapter 4. Again, the higher sputtering power gives rise to the phase mixture with the presence of BO. The difference between the BFO films on STO and LAO substrates is that the super-tetragonal phase occurs at lower sputtering power on LAO than STO substrates. This indicates a strain effect from LAO substrate, which favors the formation of super-tetragonal phase BFO as they have closer in-plane lattice parameters. For the sputtering power of 120 W, the diffraction peaks from BO become stronger while the mixture phase of BFO remains, as shown in Figure 5.9 (c). The AFM images (Figure 5.10) show a flat surface for 50 W film, a small amount of square-like outgrowth at 100 W and a large amount of out-growth islands at 120 W. This also demonstrates more BO present in the BFO film as sputtering power increases, in agreement with XRD results.

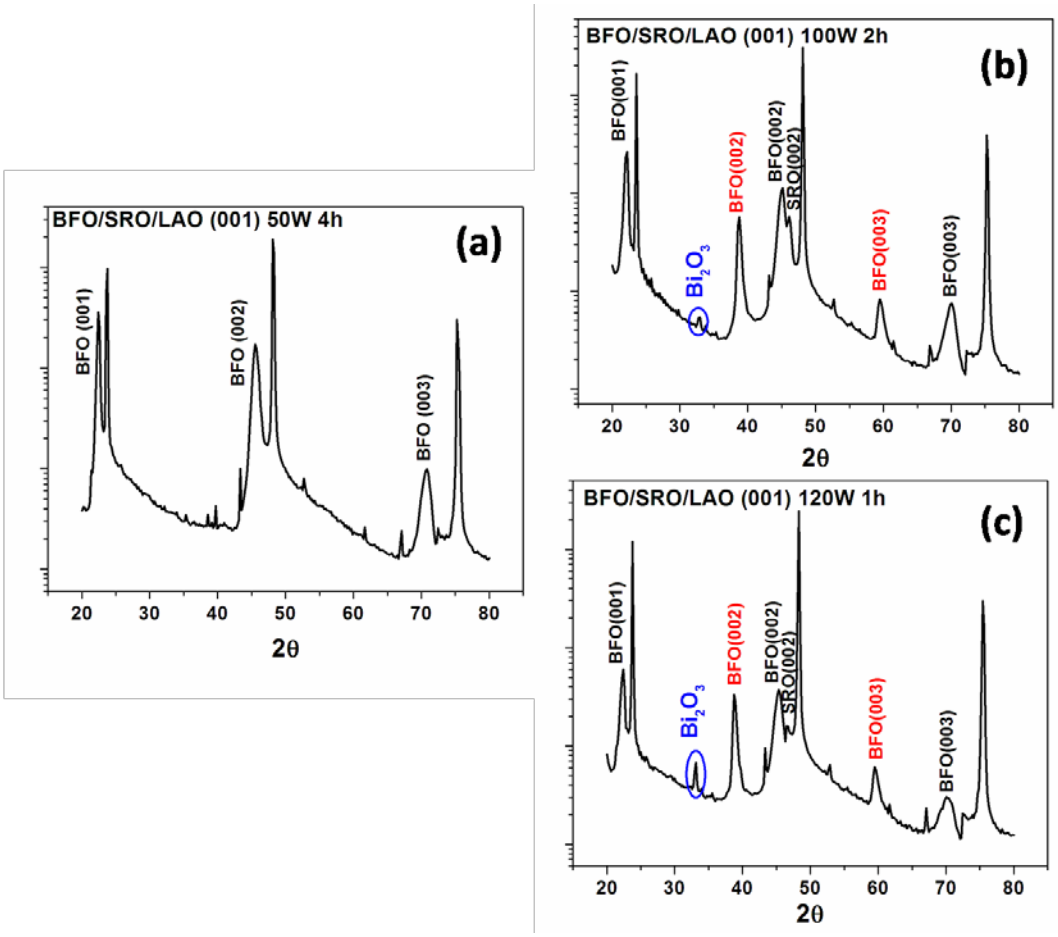

Figure 5.9 X-ray diffraction patterns of BFO films grown at the sputtering power of 50 W (a), 100 W (b) and 120 W (c) on SRO-buffered LAO (001) substrates.

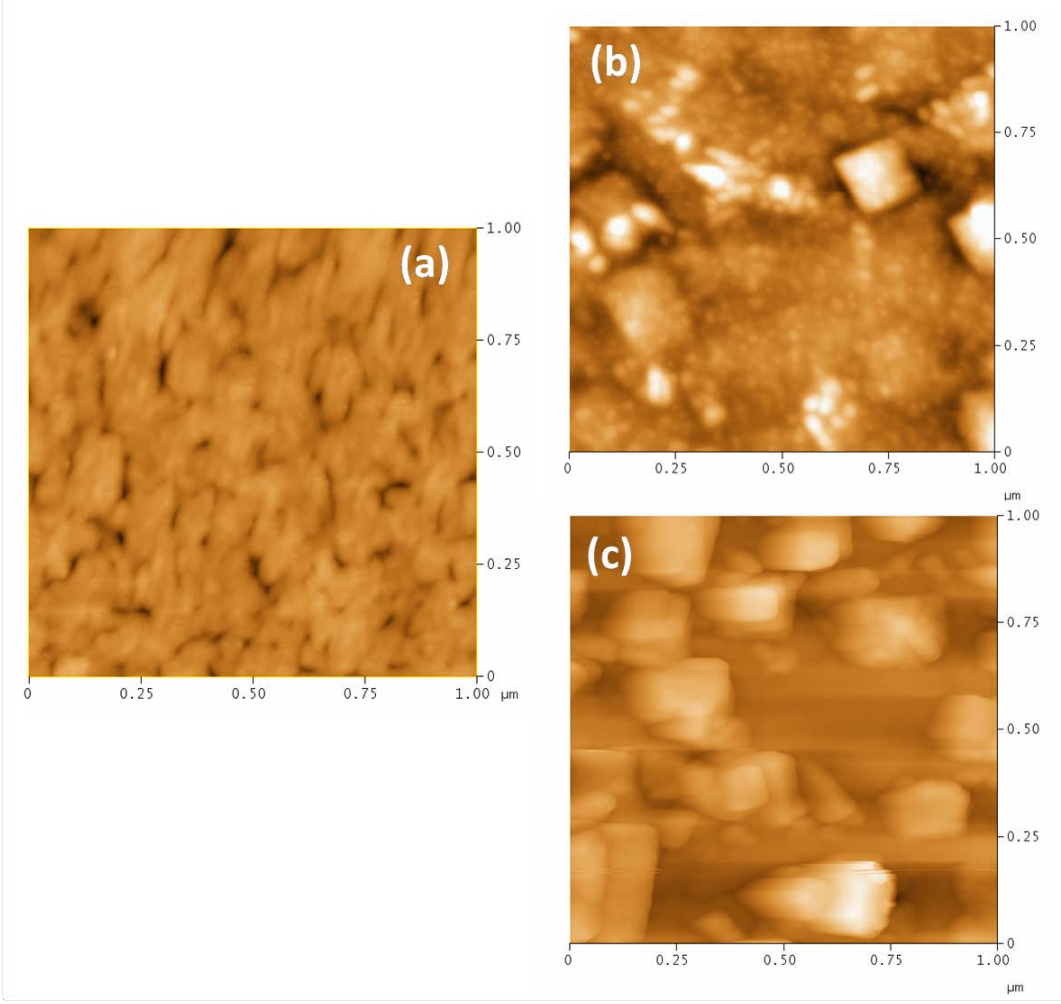

Figure 5.10 AFM topography images of BFO films grown at the sputtering power of 50 W (a), 100 W (b) and 120 W (c) on SRO-buffered LAO (001) substrates.

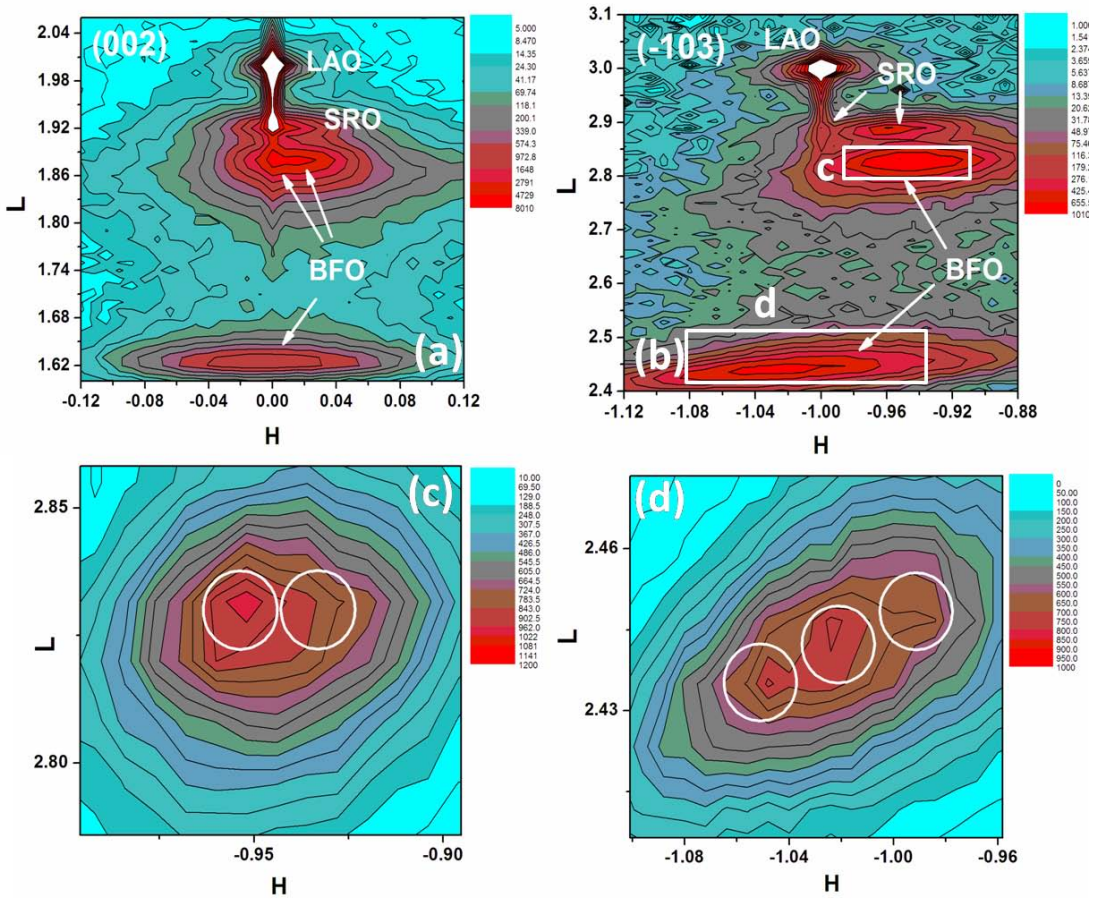

Figure 5.11 (002) (a) and (-103) (b) reciprocal space mapping of the BFO films grown at the sputtering power of 100 W on SRO-buffered LAO (001) substrates. (c) and (d) shows the enlarged (-103) diffraction peak for SRO and BFO, respectively.

Reciprocal space mappings around (002) and (-103) were measured for the BFO films grown at 100 W on SRO-buffered LAO substrates, as shown in Figure 5.11. For SRO, it is very interesting to see that the diffraction peak split into two peaks in (002) RSM (Figure 5.11 (a)). Combined with the (-103) diffraction peaks in Figure 5.11 (b), SRO exhibits two tetragonal phases. The first SRO tetragonal phase T_1 has lattice parameters of $a = b = 3.959$ Å, $c = 3.935$ Å, while the other SRO phase T_2 has lattice parameters of $a = b = 3.790$ Å, $c = 3.935$ Å. These two phases are different only in

in-plane lattice parameters. However, for the SRO film on LAO substrates before deposition of BFO layer, only a single diffraction peak was observed in (-103) RSM (Figure 5.12). The lattice parameters derived from the XRD are $a = b = 3.883$ Å, $c = 3.964$ Å. This means that the growth of BFO top layer separates SRO into two phases. In addition, SRO T_1 phase has close in-plane lattice constant with that of BFO bulk-like phase and SRO T_2 phase matches the super-tetragonal-like BFO phase. This indicates the possible strain effect from top BFO layer to the underneath SRO layer. Normally, it is expected that the bottom layer would constrain the lattice of the top layer during the growth process. However, we observe the different phenomena here. As a result of the formation of phase mixture in the top BFO layer, the bottom SRO layer also develops into two phases in order to accommodate the misfit strain from the BFO layer.

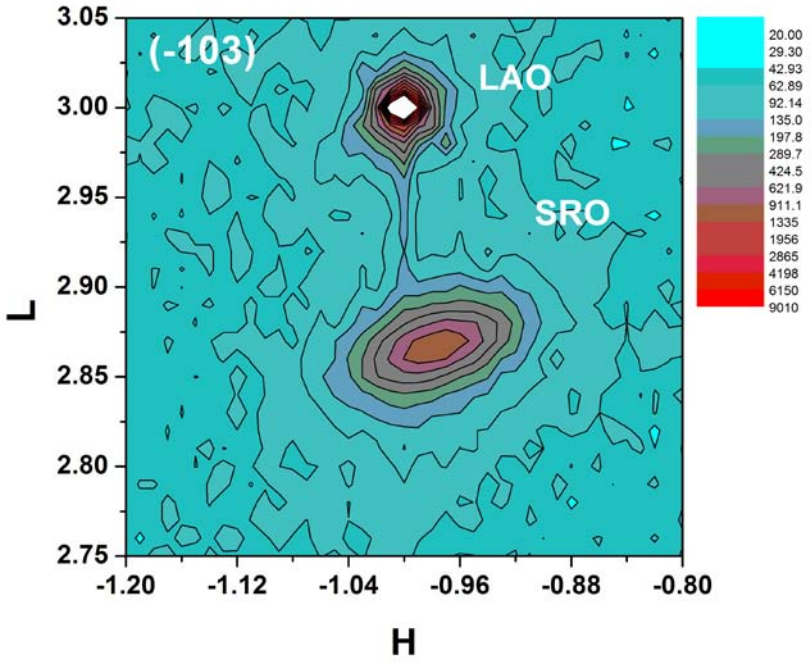

Figure 5.12 (-103) reciprocal space mapping of SRO film grown on LAO (001)

substrate

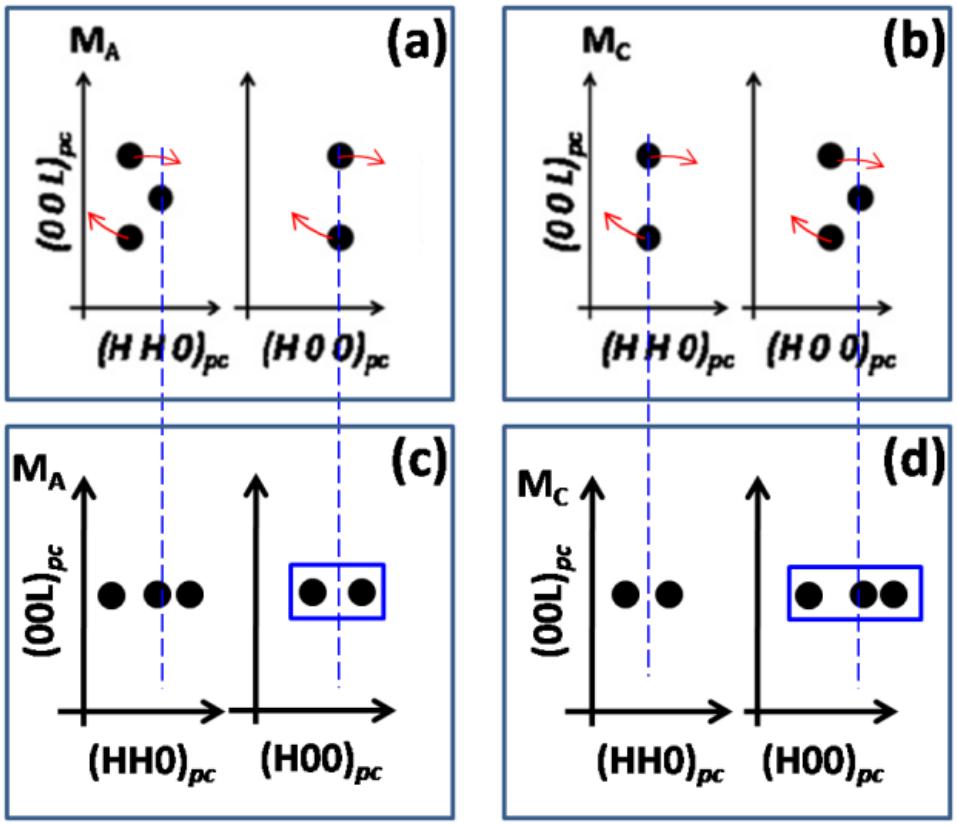

Figure 5.13 Schematic illustration of diffraction patterns in reciprocal space mapping for (a) M_A (b) M_C phases without twinning rotation, (c) M_A and (d) M_C phases with full twinning rotation. The curved arrows show the rotation directions.

From both (002) and (-103) RSM, two BFO diffraction peaks were observed, corresponding to the out-of-plane lattice constant of c = 4.031 Å and c = 4.662 Å, respectively. They are consistent with the bulk-like BFO phase and super-tetragonal-like BFO phase, respectively. To understand the strict symmetries of these BFO phases, the enlarged part of BFO peaks from (-103) RSM are shown in Figure 5.11 (c) and (d). It is clear that the BFO has two diffraction peaks in Figure 5.11

(c) and three peaks in Figure 5.11 (d). This means that these two BFO phases are monoclinic M_A and M_C, respectively. The specific diffraction peaks of these two phases can be understood as follows. In Figure 5.13 (a) and (b), the standard diffraction patterns are drawn according to the special monoclinic distortion for M_A and M_C phases. However, the (H0L) RSM (-103) from BFO in Figure 5.11 (c) and (d) does not agree with any of them. If the twinning rotation occurs, the diffraction patterns would rotate, as indicated by the arrows in Figure 5.13 (a) and (b). The fully rotated monoclinic structure would give rise to the diffraction pattern drawn in Figure 5.13 (c) and (d) for monoclinic M_A and M_C, respectively. The boxes in these two figures agree well with what have been observed for BFO from experiments. Therefore, the phase mixture of BFO consists of monoclinic M_A phase with lattice parameters a = 5.598 Å, b = 5.536 Å, c = 4.031 Å, β =89.54° and monoclinic M_C phase with lattice parameters a = 3.707 Å, b = 3.718 Å, c = 4.662 Å, β =89.47°. For BFO M_A phase, $a_m/\sqrt{2}$ = 3.959 Å, which is very close to the in-plane lattice parameter of SRO T_1 phase. On the other hand, the in-plane lattice parameters of BFO M_C and SRO T_2 phase are very close. This also provides the evidence for the strain effect from BFO to SRO. The experimental results here also indicate, under certain film growth condition, a mixture of BFO different phases may have a lower total energy as compared to anyone of the single BFO phase involved. One possible schematic structure model is drawn in Figure 5.14. The real arrangement of SRO phase and BFO phase mixtures needs further study

by cross-sectional TEM study.

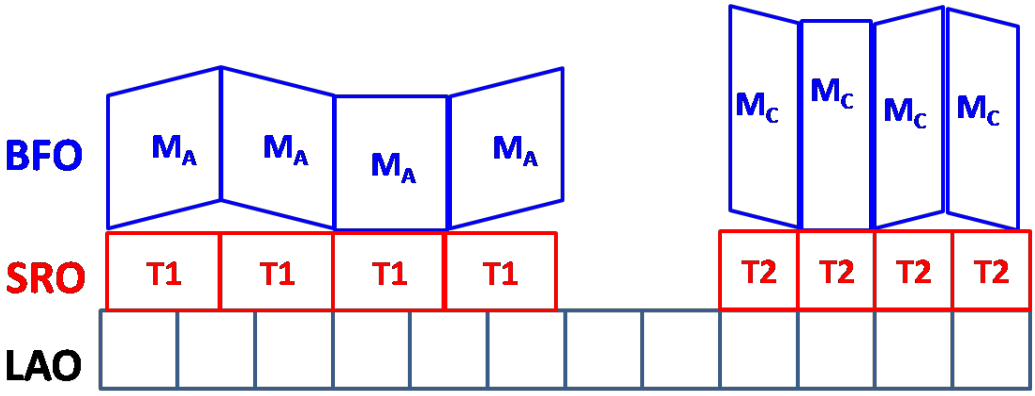

Figure 5.14 Schematic illustration of the possible configuration for BFO M_A and M_C phases on SRO T_1 and T_2 phases on LAO (001) substrates

In the remaining part of this section, the ferroelectric behaviour of these BFO films on SRO-buffered LAO substrates will be discussed. Gold electrodes were deposited on top of the BFO film for the ferroelectric measurement, as mentioned in Chapter 2.5. The 50 W BFO film gives a very good square-like P-E hysteresis loop, as shown in Figure 5.15 (a). The remanent polarization is around 70 μC/cm^2. This is comparable to the ferroelectric polarization measured for the monoclinic BFO film on SRO-buffered STO substrates [79]. For the phase mixture of BFO film at 100W, the hysteresis loop is not closed,as shown in Figure 5.15 (b). According to the Radiant manual, this type of hysteresis loop may well be due to the diode breakdown at one of the electrode-ferroelectric interface. As the BO phase may be located at SRO-BFO interface, it is highly likely that breakdown happens at the SRO-BFO interface as the

applied voltage increases. Figure 5.15 (c) shows the hysteresis loop for 120W BFO film. Due to the large amount of BO present in the film, the loop cannot be well saturated before breakdown.

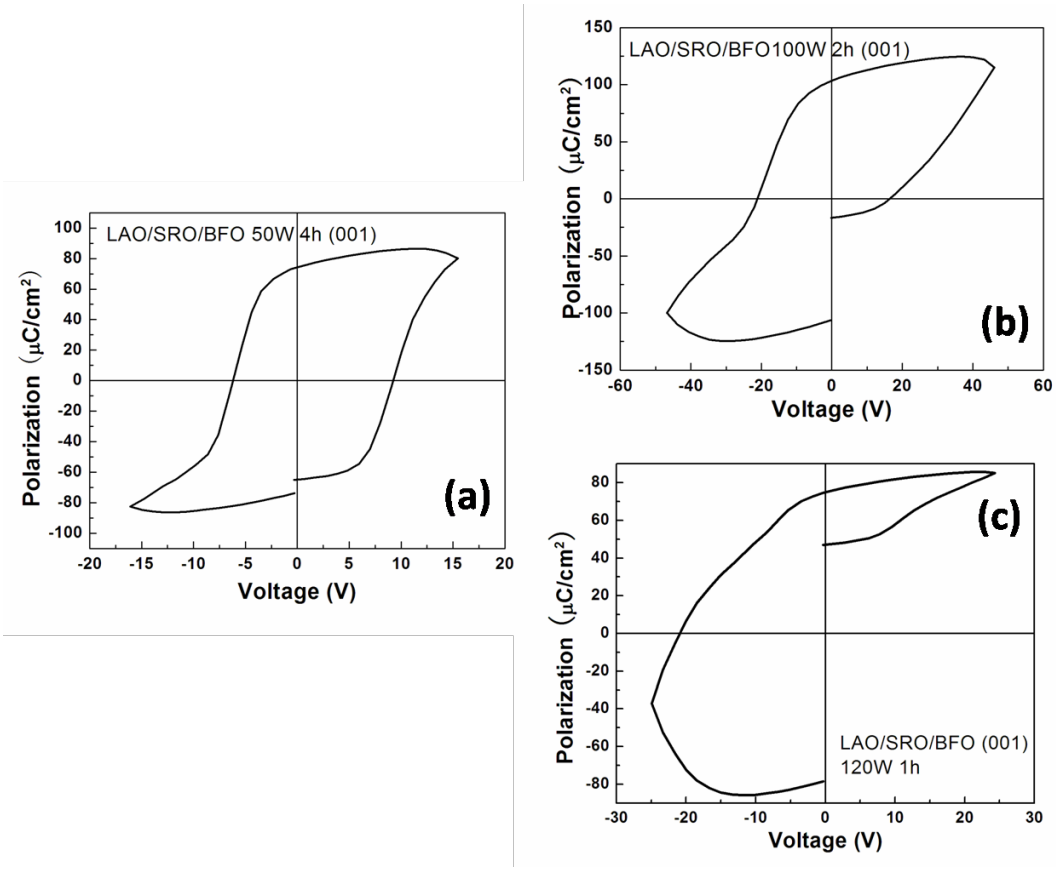

Figure 5.15 Ferroelectric hysteresis loops for BFO films grown at the sputtering power of 50 W (a), 100 W (b) and 120 W (c) on SRO-buffered LAO (001) substrates.

As the in-plane lattice of SRO (3.93 Å) does not match well with LAO substrates (3.79 Å), other conductive buffer layers with closer in-plane lattice constant should give rise to a better epitaxial growth of BFO phase with a giant *c/a*. $LaNiO_3$ (LNO) is chosen as a conductive buffer layer, with an in-plane lattice constant of 3.83 Å, which is very close to 3.79 Å of LAO substrates. As shown in Figure 5.16, the preliminary result

from (-103) RSM indicates a coherent growth of LNO on LAO substrates. The LNO layer has the same H value with LAO substrates, indicating that the LNO buffer layer is fully strained on the substrate. Further work on the fully strained BFO film on the top of LNO buffer layer will be conducted.

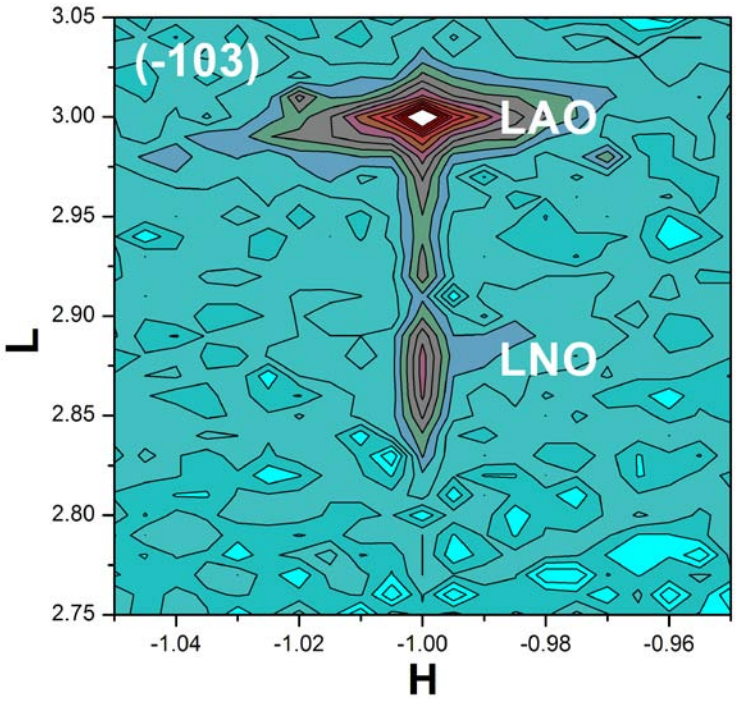

Figure 5.16 (-103) reciprocal space mapping of LNO film deposited on LAO (001) substrate

5.5 Summary

Unlike the monoclinic M_C BFO phase observed in thin films deposited on LAO (001)

substrates [32], the large compressive strain of ~7% from NCAO (001) substrates constrain BFO film into a strictly super-tetragonal phase at the film thickness of ~30 nm. At larger BFO film thickness, the fully strained super-tetragonal phase relaxes to a mixture of the super-tetragonal and bulk-like tetragonal BFO phase, and finally develops to a single bulk-like tetragonal phase. The super-tetragonal BFO phase has a *c/a* ~ 1.2 while the bulk-like tetragonal phase has a *c/a* ~ 1.02. This confirms that strict super-tetragonal BFO phase can be stabilized by an extremely high compressive strain around 7%.

For the ultrathin BFO film grown on LAO (001) substrate, our X-ray diffraction results show a monoclinic M_A structure, instead of the strict super-tetragonal phase. Due to the in-plane shear strain from LAO substrate and anisotropic strain from $YAlO_3$ (YAO) (110) substrate, fully strained BFO films on these two substrates show a monoclinic symmetry [50, 87]. The super-tetragonal BFO phase can be stabilized on NCAO substrate due to the tetragonal symmetry of the substrate. These observations suggest that not only the in-plane lattice dimension affects the film symmetry, the shear distortion and anisotropy of in-plane lattice also changes the film structure.

For the BFO thin films grown on SRO-buffered LAO (001) substrates, growth rate induces a phase transition from a single monoclinic M_A phase to a phase mixture of

monoclinic M_C phase with a giant *c/a* ratio and monoclinic M_A phase. The possible origin for this phase transition is related to the role of BO in the film growth process. The strain effect from the top BFO phase mixture layer on SRO layer may give rise to the phase separation of SRO into two tetragonal phases. The remanent polarization for monoclinic BFO film deposited at 50 W on LAO substrate is measured to be around 70 $\mu C/cm^2$, which is comparable to the ferroelectric polarization of monoclinic BFO film on SRO-buffered STO substrates. The ferroelectric behaviour of the super-tetragonal BFO phase deposited on SRO-buffered LAO (001) substrate cannot be properly characterized due to a large leakage.

Chapter 6. CONCLUSIONS AND FUTURE WORK

6.1 Conclusions

In this project, a systematic investigation has been made into the crystal structures and ferroelectric behaviour of BFO epitaxial thin films deposited on different substrates. Several new phenomena have been observed and studied, concerning the film growth, phase control, crystal structure and ferroelectric behavior of different BFO phases. .

Radio frequency (RF) sputtering is used to grow the epitaxial BFO thin films. The effect of various sputtering parameters on the film quality has been studied, including the target composition, gas pressure, oxygen pressure, sputtering power, sputtering time and temperature. By optimizing these conditions, high quality BFO films with desired epitaxial growth and low leakage are obtained. RF sputtering generally results in films with rougher surface and lower epitaxial quality as compared to pulse laser deposition (PLD) and molecular beam epitaxy (MBE). However, high quality films are successfully achieved by fine tuning the sputtering parameters, as demonstrated in this work.

In general, the crystal phases for BFO epitaxial thin films can be controlled by strain engineering, in which the BFO lattice follows the single crystal substrates by fully coherent growth. It is found that high compressive strain of around 7% induces the super-tetragonal phase, ~ 4.5% compressive strain results in monoclinic phase with a giant c/a ~ 1.2, and a small compressive strain of 1.5% leads to the monoclinic phase with a small c/a ~ 1.0. The disadvantage of the strain engineering is the thickness limit of fully strained film, as above the critical thickness (~50 nm) the structure tends to relax back to bulk structure. For the formation of super-tetragonal BFO phase, a new approach has been demonstrated in this work, whereby BO is used as a buffer layer to induce the phase transition from monoclinic to super-tetragonal phase. The advantage of this approach is that much thicker films (~200 nm) with single super-tetragonal phase can be successfully obtained.

For BFO films grown on SRO-buffered STO (001) substrates, tetragonal, monoclinic and the super-tetragonal BFO phases can be formed depending on the growth condition. At a low sputtering power below 120 W, tetragonal BFO phase is developed for the film thickness less than 30 nm, while monoclinic BFO phase is obtained for film thickness in the range of 180 to 720 nm. The super-tetragonal BFO phase is developed at sputtering powers of above 150 W.

Studies of monoclinic BFO phase using high-resolution synchrotron X-ray diffraction reveal a new rotated twinning structure, which leads to the formation of vertical domain walls. As a result of the elongation of polarization direction and rotation of twinning blocks, the remanent polarization is significantly enhanced along the measured (001) direction and the leakage current density is greatly reduced. For the strain effect on ferroelectric polarization of monoclinic BFO phase, our results show that remanent polarization increases as the film thickness increases to 450 nm and then decreases from 450 nm to 720 nm. The polarization has a strong dependence on the body diagonal length of distorted pseudocubic unit cell, indicating that the distortion in polarization direction is the critical factor that determines the remanent polarization. This agrees with the theoretical understanding that ionic displacement along the polarization direction is the main contribution to the measured polarization.

The formation of super-tetragonal BFO phase on STO substrates at high sputtering power contradicts the prediction from strain phase diagram, which shows that it is highly unlikely to form the super-tetragonal phase on STO substrate. By detailed structure analyses, the parasitic β-BO phase is identified to be responsible for the formation of super-tetragonal BFO phase in the thin film deposited on STO substrates. The detailed arrangement of β-BO phase and super-tetragonal BFO phase in the film is

clarified, which shows four super-tetragonal BFO lattices match one BO lattice in the in-plane dimension. This opens an alternative formation route for the super-tetragonal BFO phase on single crystal substrates.

The large compressive strain of ~7% from NCAO substrates constrains BFO film into a strictly super-tetragonal phase at the film thickness about 30 nm. With increasing BFO film thickness, the fully strained super-tetragonal phase relaxes to a mixture of super-tetragonal and tetragonal BFO phase with a *c/a* ~ 1.2, and finally develops to a single tetragonal phase with a *c/a* ~ 1.02. This confirms that the strict super-tetragonal BFO phase can be stabilized by extremely high compressive strain around 7%.

For the ultrathin BFO film grown on LAO (001) substrate, X-ray diffraction show a monoclinic M_A structure, instead of the widely reported M_C phase. For the BFO films grown on SRO-buffered LAO (001) substrates, growth rate induces a phase transition from a single monoclinic M_A phase to a phase mixture of monoclinic M_C phase with a giant *c/a* and monoclinic M_A phase. The origin for this phase transition is related to the role of BO in the film growth process, although detailed structure study by TEM has not been performed. Interestingly, the top BFO layer of mixture phase on SRO layer may give rise to the phase separation of SRO into two tetragonal phases. This shows a rare example of strain effect from the top layer to bottom layer, which deserves more

detailed study in the future to better understand the formation mechanism of BFO phase mixture.

6.2 Suggestions for Future Work

Although epitaxial BFO thin films have been extensively studied for almost ten years, there are still several fundamental issues to be properly addressed before the real device applications. Here we propose several topics to be investigated in the future.

i) The super-tetragonal BFO phase has a greatly distorted lattice and potentially possesses giant polarization and electromechanical response, which makes it interesting for both fundamental study and practical device applications. Intrinsic ferroelectric and piezoelectric characterization for this super-tetragonal phase demands the growth of high insulating BFO thin films. Future investigation should be made to obtain high quality super-tetragonal BFO films with proper conductive bottom layer, by either strain engineering or employing the BO buffer layer or both.

ii) Orthorhombic BFO phase has never been demonstrated experimentally. The first principles calculation shows that orthorhombic phase is stable under extremely

large tensile strain around 8% in (001) orientation [56], which cannot be realized experimentally, because of the lack in appropriate substrates available. Another theoretical calculation illustrates that orthorhombic BFO phase can also be formed under large compressive strain in (110) orientation films [60]. Interestingly, this phase is predicted to be paraelectric and has unique optical behavior. This may be of interest for the photovoltaic study of BFO orthorhombic phase films. Future work on the growth and electric characterization of the orthorhombic phase BFO films would complete the strain phase diagram of BFO system and provide a better understanding on the phase control in ferroelectric thin films.

iii) Although different BFO phases, such as monoclinic and tetragonal, in epitaxial thin films have been demonstrated to have superior properties than the rhombohedral phase of bulk single crystal, detailed structure information on the atomic positions and chemical bonding for these phases is still missing. Single crystal X-ray diffraction is a standard method to completely solve the crystal structure. It can provide the accurate electron density map in the unit cell, which leads to all structure information at atomic level. As the epitaxial thin films are close to single crystal, it is possible to employ this method to solve the crystal structures of new BFO phases in epitaxial thin films that are otherwise not available in the bulk form. Our preliminary study on rhombohedral thin film generates results close to the

rhombohedral single crystal, which indicates this method is applicable on epitaxial thin film samples. Future study of other BFO phases would help to understand how the atoms react under specific strain conditions and the ferroelectric origin of BFO at atomic levels.

REFERENCES

[1] M. E. Lines and A. M. Glass, Principles and applications of ferroelectrics and related materials, Clarendon Press, Oxford, 1977.

[2] J. F. Scott, Science 315 (2007) 954.

[3] R. E. Newnham and G. R. Ruschau, Journal of American Ceramic Society 74 (1991) 463.

[4] H. Bea, M. Gajek, M. Bibes, and A. Barthelemy, Journal of physics: condensed matter 20 (2008) 434221.

[5] P. W. Forsbergh, Jr., Physical Review 76 (1949) 1187.

[6] J. F. Scott, Ferroelectric memories, Springer, Berlin, 2000.

[7] J. B. Neaton, C. Ederer, U. V. Waghmare, N. A. Spaldin, and K. M. Rabe, Physical Review B 71 (2005) 014113.

[8] G. H. Haertling, Journal of American Ceramic Society 82 (1999) 797.

[9] B. Jaffe, W. R. Cook, and H. Jaffe, Piezoeletric ceramics, Academic Press, 1971.

[10] Y. Saito, H. Takao, T. Tani, T. Nonoyama, K. Takatori, T. Homma, T. Nagaya, and M. Nakamura, Nature 432 (2004) 84.

[11] W. Eerenstein, N. D. Mathur, and J. F. Scott, Nature 442 (2006) 759.

[12] G. Catalan and J. F. Scott, Advanced Materials 21 (2009) 2463.

[13] N. A. Spaldin and M. Fiebig, Science 309 (2005) 391.

[14] N. A. Hill, Journal of physical chemistry B 104 (2000) 6694.

[15] C.-W. Nan, M. I. Bichurin, S. Dong, D. Viehland, and G. Srinivasan, Journal of Applied Physics 103 (2008) 031101.

[16] J. V. Suchtelen, Philips Res. Rep. 27 (1972) 28.

[17] S.-W. Cheong and M. Mostovoy, Nat Mater 6 (2007) 13.

[18] R. Ramesh, Nature 461 (2009) 1218.

[19] R. Seshadri and N. A. Hill, Chemistry of Materials 13 (2001) 2892.

[20] B. B. Van Aken, T. T. M. Palstra, A. Filippetti, and N. A. Spaldin, Nat Mater 3 (2004) 164.

[21] D. V. Efremov, J. van den Brink, and D. I. Khomskii, Nat Mater 3 (2004) 853.

[22] Y. Tokura, Science 312 (2006) 1481.

[23] P. Jain, N. S. Dalal, B. H. Toby, H. W. Kroto, and A. K. Cheetham, Journal of the American Chemical Society 130 (2008) 10450.

[24] F. Kubel and H. Schmid, Acta Crystallographica Section B 46 (1990) 698.

[25] Y. Kuroiwa, S. Aoyagi, A. Sawada, J. Harada, E. Nishibori, M. Takata, and M. Sakata, Physical Review Letters 87 (2001) 217601.

[26] J. R. Teague, R. Gerson, and W. J. James, Solid State Communications 8 (1970) 1073.

[27] J. Wang, J. B. Neaton, H. Zheng, V. Nagarajan, S. B. Ogale, B. Liu, D. Viehland, V. Vaithyanathan, D. G. Schlom, U. V. Waghmare, N. A. Spaldin, K. M. Rabe, M. Wuttig, and R. Ramesh, Science 299 (2003) 1719.

[28] D. Lebeugle, D. Colson, A. Forget, M. Viret, P. Bonville, J. F. Marucco, and S. Fusil, Physical Review B 76 (2007) 024116.

[29] V. V. Shvartsman, W. Kleemann, R. Haumont, and J. Kreisel, Applied Physics Letters 90 (2007) 172115.

[30] I. Sosnowska and R. Przenioslo, Physical Review B 84 (2011) 144404.

[31] H. Bea, M. Bibes, S. Fusil, K. Bouzehouane, E. Jacquet, K. Rode, P. Bencok, and A. Barthelemy, Physical Review B 74 (2006) 020101.

[32] Z. Chen, S. Prosandeev, Z. L. Luo, W. Ren, Y. Qi, C. W. Huang, L. You, C. Gao, I. A. Kornev, T. Wu, J. Wang, P. Yang, T. Sritharan, L. Bellaiche, and L. Chen,

Physical Review B 84 (2011) 094116.

[33] B. Yu, M. Li, Z. Hu, L. Pei, D. Guo, X. Zhao, and S. Dong, Applied Physics Letters 93 (2008) 182909.

[34] S. Fujino, M. Murakami, V. Anbusathaiah, S. H. Lim, V. Nagarajan, C. J. Fennie, M. Wuttig, L. Salamanca-Riba, and I. Takeuchi, Applied Physics Letters 92 (2008) 202904.

[35] T. Zhao, A. Scholl, F. Zavaliche, K. Lee, M. Barry, A. Doran, M. P. Cruz, Y. H. Chu, C. Ederer, N. A. Spaldin, R. R. Das, D. M. Kim, S. H. Baek, C. B. Eom, and R. Ramesh, Nat Mater 5 (2006) 823.

[36] K. Y. Choi, S. H. Do, P. Lemmens, D. Wulferding, C. S. Woo, J. H. Lee, K. Chu, and C. H. Yang, Physical Review B 84 (2011) 132408.

[37] S. Y. Yang, SeidelJ, S. J. Byrnes, ShaferP, C. H. Yang, M. D. Rossell, YuP, Y. H. Chu, J. F. Scott, J. W. Ager, L. W. Martin, and RameshR, Nat Nano 5 (2010) 143.

[38] W. Ji, K. Yao, and Y. C. Liang, Physical Review B 84 (2011) 094115.

[39] W. Ji, K. Yao, and Y. C. Liang, Advanced Materials 22 (2010) 1763.

[40] H. W. Jang, S. H. Baek, D. Ortiz, C. M. Folkman, R. R. Das, Y. H. Chu, P. Shafer, J. X. Zhang, S. Choudhury, V. Vaithyanathan, Y. B. Chen, D. A. Felker, M. D. Biegalski, M. S. Rzchowski, X. Q. Pan, D. G. Schlom, L. Q. Chen, R. Ramesh, and C. B. Eom, Physical Review Letters 101 (2008) 107602.

[41] J. H. Haeni, P. Irvin, W. Chang, R. Uecker, P. Reiche, Y. L. Li, S. Choudhury, W. Tian, M. E. Hawley, B. Craigo, A. K. Tagantsev, X. Q. Pan, S. K. Streiffer, L. Q. Chen, S. W. Kirchoefer, J. Levy, and D. G. Schlom, Nature 430 (2004) 758.

[42] E. Bousquet, M. Dawber, N. Stucki, C. Lichtensteiger, P. Hermet, S. Gariglio, J.-M. Triscone, and P. Ghosez, Nature 452 (2008) 732.

[43] A. Berger, D. Hesse, A. Hahnel, M. Arredondo, and M. Alexe, Physical Review B 85 (2012) 064104.

[44] P. Wurfel, I. P. Batra, and J. T. Jacobs, Physical Review Letters 30 (1973) 1218.

[45] N. A. Pertsev, A. G. Zembilgotov, and A. K. Tagantsev, Physical Review Letters

80 (1998) 1988.

[46] N. A. Pertsev, A. K. Tagantsev, and N. Setter, Physical Review B 61 (2000) R825.

[47] N. A. Pertsev, V. G. Kukhar, H. Kohlstedt, and R. Waser, Physical Review B 67 (2003) 054107.

[48] C. Ederer and N. A. Spaldin, Physical Review Letters 95 (2005) 257601.

[49] D. Vanderbilt and M. H. Cohen, Physical Review B 63 (2001) 094108.

[50] H. M. Christen, J. H. Nam, H. S. Kim, A. J. Hatt, and N. A. Spaldin, Physical Review B 83 (2011) 144107.

[51] G. Xu, H. Hiraka, G. Shirane, J. Li, J. Wang, and D. Viehland, Applied Physics Letters 86 (2005) 182905.

[52] R. J. Zeches, M. D. Rossell, J. X. Zhang, A. J. Hatt, Q. He, C. H. Yang, A. Kumar, C. H. Wang, A. Melville, C. Adamo, G. Sheng, Y. H. Chu, J. F. Ihlefeld, R. Erni, C. Ederer, V. Gopalan, L. Q. Chen, D. G. Schlom, N. A. Spaldin, L. W. Martin, and R. Ramesh, Science 326 (2009) 977.

[53] M. N. Iliev, M. V. Abrashev, D. Mazumdar, V. Shelke, and A. Gupta, Physical Review B 82 (2010) 014107.

[54] A. J. Hatt, N. A. Spaldin, and C. Ederer, Physical Review B 81 (2010) 054109.

[55] I. C. Infante, S. Lisenkov, B. Dupe, M. Bibes, S. Fusil, E. Jacquet, G. Geneste, S. Petit, A. Courtial, J. Juraszek, L. Bellaiche, A. Barthelemy, and B. Dkhil, Physical Review Letters 105 (2010) 057601.

[56] B. Dupe, S. Prosandeev, G. Geneste, B. Dkhil, and L. Bellaiche, Physical Review Letters 106 (2011) 237601.

[57] J. Allibe, K. Bougot-Robin, E. Jacquet, I. C. Infante, S. Fusil, C. Carretero, J. L. Reverchon, B. Marcilhac, D. Crete, J. C. Mage, A. Barthelemy, and M. Bibes, Applied Physics Letters 96 (2010) 182902.

[58] M. P. Cruz, Y. H. Chu, J. X. Zhang, P. L. Yang, F. Zavaliche, Q. He, P. Shafer, L. Q. Chen, and R. Ramesh, Physical Review Letters 99 (2007) 217601.

[59] G. Xu, J. Li, and D. Viehland, Applied Physics Letters 89 (2006) 222901.

[60] S. Prosandeev, I. A. Kornev, and L. Bellaiche, Physical Review Letters 107 (2011) 117602.

[61] D. C. Arnold, K. S. Knight, F. D. Morrison, and P. Lightfoot, Physical Review Letters 102 (2009) 027602.

[62] D. H. Kim, H. N. Lee, M. D. Biegalski, and H. M. Christen, Applied Physics Letters 92 (2008) 012911.

[63] D. Ricinschi, K. Y. Yun, and M. Okuyama, Journal of Physics: Condensed Matter 18 (2006) L97.

[64] H. Bea, B. Dupe, S. Fusil, R. Mattana, E. Jacquet, B. Warot-Fonrose, F. Wilhelm, A. Rogalev, S. Petit, V. Cros, A. Anane, F. Petroff, K. Bouzehouane, G. Geneste, B. Dkhil, S. Lisenkov, I. Ponomareva, L. Bellaiche, M. Bibes, and A. Barthelemy, Physical Review Letters 102 (2009) 217603.

[65] J. X. Zhang, Q. He, M. Trassin, W. Luo, D. Yi, M. D. Rossell, P. Yu, L. You, C. H. Wang, C. Y. Kuo, J. T. Heron, Z. Hu, R. J. Zeches, H. J. Lin, A. Tanaka, C. T. Chen, L. H. Tjeng, Y. H. Chu, and R. Ramesh, Physical Review Letters 107 (2011) 147602.

[66] X. Qi, M. Wei, Y. Lin, Q. Jia, D. Zhi, J. Dho, M. G. Blamire, and J. L. MacManus-Driscoll, Applied Physics Letters 86 (2005) 071913.

[67] K. Wasa, M. Kitabatake, and H. Adachi, Thin Film Materials Technology: Sputtering of Compound Materials, Springer, 2004.

[68] P. Yu, J. S. Lee, S. Okamoto, M. D. Rossell, M. Huijben, C. H. Yang, Q. He, J. X. Zhang, S. Y. Yang, M. J. Lee, Q. M. Ramasse, R. Erni, Y. H. Chu, D. A. Arena, C. C. Kao, L. W. Martin, and R. Ramesh, Physical Review Letters 105 (2010) 027201.

[69] V. Holy, U. Pietsch, and T. Baumbach, High Resolution X-ray Scattering from Thin Films and Multilayers, Springer, New York, 1999.

[70] P. B. Hirsh, Electron Microscopy of Thin Crystals, Butterworths, London, 1965.

[71] S. J. Pennycook and P. D. Nellist, Scanning transmission electron microscopy:

imaging and analysis, Springer, New York, 2011.

[72] C. B. Sawyer and C. H. Tower, Physical Review 35 (1930) 269.

[73] M. Dawber, K. M. Rabe, and J. F. Scott, Reviews of Modern Physics 77 (2005) 1083.

[74] L. Pintilie, C. Dragoi, Y. H. Chu, L. W. Martin, R. Ramesh, and M. Alexe, Applied Physics Letters 94 (2009) 232902.

[75] C. J. M. Daumont, S. Farokhipoor, A. Ferri, J. C. Wojdel, J. Iniguez, B. J. Kooi, and B. Noheda, Physical Review B 81 (2010) 144115.

[76] R. D. King-Smith and D. Vanderbilt, Physical Review B 47 (1993) 1651.

[77] R. Resta, Reviews of Modern Physics 66 (1994) 899.

[78] W. S. Chang, L. C. Lim, P. Yang, H. Miao, C. S. Tu, Q. Chen, and A. K. Soh, Applied Physics Letters 94 (2009) 202907.

[79] H. Liu, K. Yao, P. Yang, Y. Du, Q. He, Y. Gu, X. Li, S. Wang, X. Zhou, and J. Wang, Physical Review B 82 (2010) 064108.

[80] H. Liu, P. Yang, K. Yao, K. P. Ong, P. Wu, and J. Wang, Advanced Functional Materials 22 (2012) 937.

[81] L. You, N. T. Chua, K. Yao, L. Chen, and J. Wang, Physical Review B 80 (2009) 024105.

[82] H. Liu, P. Yang, K. Yao, and J. Wang, Applied Physics Letters 98 (2011) 102902.

[83] H. Bea, M. Bibes, A. Barthelemy, K. Bouzehouane, E. Jacquet, A. Khodan, J. P. Contour, S. Fusil, F. Wyczisk, A. Forget, D. Lebeugle, D. Colson, and M. Viret, Applied Physics Letters 87 (2005) 072508.

[84] C. J. Cheng, D. Kan, S. H. Lim, W. R. McKenzie, P. R. Munroe, L. G. Salamanca-Riba, R. L. Withers, I. Takeuchi, and V. Nagarajan, Physical Review B 80 (2009) 014109.

[85] H.-J. Liu, C.-W. Liang, W.-I. Liang, H.-J. Chen, J.-C. Yang, C.-Y. Peng, G.-F. Wang, F.-N. Chu, Y.-C. Chen, H.-Y. Lee, L. Chang, S.-J. Lin, and Y.-H. Chu,

Physical Review B 85 (2012) 014104.

[86] Z. L. Wang and A. J. Shapiro, Surface Science 328 (1995) 141.

[87] Z. Chen, Z. Luo, C. Huang, Y. Qi, P. Yang, L. You, C. Hu, T. Wu, J. Wang, C. Gao, T. Sritharan, and L. Chen, Advanced Functional Materials 21 (2011) 133.